ADAPTIVE EDGE-ENHANCED CORRELATION BASED ROBUST AND REAL-TIME VISUAL TRACKING FRAMEWORK AND ITS DEPLOYMENT IN MACHINE VISION SYSTEMS

by

Javed Ahmed

Submitted to the Department of Electrical Engineering,
Military College of Signals, in partial fulfillment of the requirements for
the degree of Doctor of Philosophy

National University of Sciences and Technology
Rawalpindi, Pakistan

February 2008

Approved for the Department of Electrical Engineering

Supervisor

Chairman of the Guidance & Examination Committee

Head of the Department

Abstract

An adaptive edge-enhanced correlation based robust and real-time visual tracking framework, and two machine vision systems based on the framework are proposed. The visual tracking algorithm can track *any* object of interest in a video acquired from a stationary or moving camera. It can handle the real-world problems, such as noise, clutter, occlusion, uneven illumination, varying appearance, orientation, scale, and velocity of the maneuvering object, and object fading and obscuration in low contrast video at various zoom levels. The proposed machine vision systems are an active camera tracking system and a vision based system for a UGV (unmanned ground vehicle) to handle a road intersection.

The core of the proposed visual tracking framework is an **E**dge **E**nhanced **B**ack-propagation neural-network **C**ontrolled **F**ast **N**ormalized **C**orrelation (EE-BCFNC), which makes the object localization stage efficient and robust to *noise*, *object fading*, *obscuration*, and *uneven illumination*. The *incorrect template initialization* and *template-drift* problems of the traditional correlation tracker are handled by a *b**e**st-match rectangle adjustment algorithm*. The *varying appearance* of the object and the *short-term neighboring clutter* are addressed by a robust *template-updating scheme*. The *background clutter* and *varying velocity* of the object are handled by looking for the object only in a *dynamically resizable search window*, in which the likelihood of the presence of the object is high. The search window is created using the prediction and the prediction error of a Kalman filter. The effect of the *long-term neighboring clutter* is reduced by weighting the template pixels using a 2D Gaussian weighting window with *adaptive* standard deviation parameters. The *occlusion* is addressed by a data association technique. The *varying scale of the object*

is handled by correlating the search window with three scales of the template, and accepting the best-match region that produces the highest peak in the three correlation surfaces. The proposed visual tracking algorithm is compared with the traditional correlation tracker and, in some cases, with the mean-shift and the condensation trackers on real-world imagery. The proposed algorithm outperforms them in robustness and executes at the speed of 25 to 75 frames/second depending on the current sizes of the adaptive template and the dynamic search window.

The proposed active camera tracking system can be used to get the target always in focus (i.e. in the center of the video frame) regardless of the motion of the target in the scene. It feeds the target coordinates estimated by the visual tracking framework into a predictive open-loop car-following control (POL-CFC) algorithm which in turn generates the precise control signals for the pan-tilt motion of the camera. The performance analysis of the system shows that its *percent overshoot*, *rise time*, and *maximum steady state error* are 0%, 1.7 second, and ±1 pixel, respectively.

The hardware of the proposed vision based system, that enables a UGV to handle a road intersection, consists of three on-board computers and three cameras (mounted on top of the UGV) looking towards the other three roads merging at the intersection. The software in each computer consists of a vehicle detector, the proposed tracker, and a finite state machine model (FSM) of the traffic. The information from the three FSMs is combined to make an autonomous decision whether it is safe for the UGV to cross the intersection or not. The results of the actual UGV experiments are provided to validate the robustness of the proposed system.

Index terms – visual tracking, adaptive edge-enhanced correlation, active camera, unmanned ground vehicle.

To the Prophet Muhammad (*Sallallahu Alaih Wa Aalihee Wasallam*)

Acknowledgements

It would be an injustice if I do not thank, first of all, Allah, the creator and controller of the whole universe. He blessed me with the will to get into the world of research and guided me through ups and downs in the course of achieving my goal. I thank Him without any limit...

I am grateful to my parents (who always pray for me to have a good place in this world and hereafter), my wife and children (for being with me even when I was not *completely* with them), and my brothers and sisters (who are my perpetual well-wishers).

I would like to thank my supervisor Dr. M. Noman Jafri (Professor, MCS) for his technical as well as managerial support during my PhD studies. I am also grateful to my co-supervisor Dr. Mubarak Shah (Agere Chair Profesor, University of Central Florida, USA), who graciously invited me to conduct the collaborative research with his research group at the world famous Computer Vision Lab under his guidance. The 8-month visit provided me with the opportunity to learn many new ideas and current trends in the field of computer vision.

I am grateful to Dr. Zhigang Zhu (City University of New York, USA), Dr. Alper Yilmaz (Ohio State University, USA), and Dr. Sohaib Ahmad Khan (Lahore University of Management Sciences, Pakistan) for accepting the manuscript of this dissertation for PhD and providing me with their positive comments and valuable suggestions for the further improvement.

I would also like to thank Brig.® Dr. Muhammad Akbar (Professor, MCS), Dr. Saleem Akbar (Professor, MCS), and Dr. Jamil Ahmad (Professor and Dean, Iqra

University, Islamabad Campus) for being members of my Guidance and Examination Committee (GEC).

I think I am going to remember Dr. Muhammad Ali Chaudhry, Robina Ashraf, Lt. Col. Fahim Arif, Lt. Col. Alamdar Raza, and Lt. Cmdr. Junaid Ahmed for a long time for accompanying me in the same vulnerable boat.

Table of Contents

List of Figures

List of Tables

1

Introduction

1.1 Chapter Overview

This chapter provides the introduction to visual tracking and its deployment in an active camera tracking system and a vision system for a UGV to handle a road intersection. It also discusses the limitations of the previous techniques, and presents the summary of the proposed solutions.

1.2 Visual Tracking

This section provides a brief introduction to visual tracking, previous work, and the contribution of the present research.

1.2.1 Introduction

Visual tracking, in general, can be defined as localizing the object of interest in consecutive frames of a video. Efficient tracking of the object in complex environments is a challenging task for the computer vision community. The complex environments or real-world problems include noise, object fading obscuration, clutter (including other similar objects in the scene), occlusion, uneven illumination, high computational complexity, and varying shape, orientation, scale, and velocity of the maneuvering object at different zoom levels of the camera. The computational complexity of the tracker is critical for most applications. Only a small percentage of

the system resources can be allocated for tracking and the rest is assigned to preprocessing stages or high-level tasks such as recognition, trajectory interpretation, and reasoning [6].

Some widely known applications of real-time visual tracking are surveillance and monitoring [1], perceptual user interfaces [2], smart rooms [3, 4], video compression [5], active camera tracking system [58], and vision-based system for a UGV (unmanned ground vehicle) to handle a road intersection [57]. The last two systems are also part of this research work.

1.2.2 Previous Work

Several techniques have been proposed by the researchers for target tracking in the consecutive video frames. Most of these are either limited to tracking specific class of objects [7, 8, 9, 10], or assume that the camera is stationary (and exploit back-ground subtraction) [41, 42]. The trackers based on the particle filter or condensation [51, 52, 53, 54] and active contours [45, 46] do not assume constant background and they are reported to track the whole object instead of only the centroid or a portion of the object [46]. However, keeping in mind the present power of a high-end computer, they are computationally too expensive to be exploited for a practical real-time tracking application. The mean shift tracker [43, 48] has gained a significant influence in the computer vision community in recent years, because it is fast, general-purpose and does not assume static background. Mean-shift is a nonparametric density gradient estimator to find the image window that is most similar to the color histogram of the object in the current frame. It iteratively carries out a kernel-based search starting at the previous location of the object [50]. There are variants, e.g. [49], to improve its localization by using additional modalities, but the original method requires the object kernels in the consecutive frames to have a certain overlap. The

success of the mean-shift highly depends on the discriminating power of the histograms that are considered as the probability density function of the object [50]. Another issue in the mean shift tracker is inherent in its use of histogram, which does not carry the spatial information of the pixels [44]. The integral histogram based tracker [47] matches the color histogram of the target with every possible region in the *whole* frame; therefore, it can track even a very fast moving object. It works slower than the mean shift tracker, because the mean shift tracker searches for the target in only a small neighborhood of the previous target-position. On a P4 3.2 GHz machine, the integral histogram tracker works with the speed of about 18 fps (frames per second), and the mean shift tracker works with the speed of about 66 fps [47]. Since the histogram does not contain the spatial information, and there is a risk of picking up a wrong candidate having similar histogram as that of the target (especially when the search is carried out in the *whole* image), this tracker is not adequately robust. More recently, in the covariance tracking [50], the object is modeled as the covariance matrix of its features, and the region (in the search image) which has minimum covariance distance with the model is considered to be the next target position. The covariance matching process in [50] is carried out on a half-resolution grid in the search image, so the accuracy of the target coordinates found by the algorithm is reduced. The reported results are quite robust, but the computational efficiency of the algorithm is not adequate for a real-time tracking application, because its maximum throughput (as reported in [50]) is only 7 fps on a P4 (3.2 GHz) PC.

There are also some widely used classic trackers, such as edge tracker, centroid tracker, and the correlation tracker. A good introduction to these trackers can be found in [11], where it is reported that the correlation tracker has proved to be the

most robust of the three, especially in a noisy and cluttered scene. However, the *standard* correlation tracker has some *inherent* problems. Firstly, it is prone to the template-drift problem; secondly, its performance tremendously deteriorates in the presence of varying illumination conditions; thirdly, if the template is kept constant throughout the tracking session, the detection performance declines especially when the object changes its shape, size, and orientation; lastly, if the user has initialized the template incorrectly due to the motion of the object in the streaming video, the tracking accuracy is not adequate. Therefore, the standard correlation tracker is not robust enough, if some preprocessing is not performed, the template is not adaptive, and above all the modification in the basic correlation formulation is not done [11, 12, 58]. Furthermore, the correlation tracker alone does not handle the other real-world problems mentioned in Section 1.2.1. As far as the implementation of the correlation operation is concerned, it can be computationally expensive in the *spatial* domain, especially when the sizes of the search window and the template are large. In order to speed up the computation, the *standard* correlation can be implemented in the frequency domain using the convolution theorem of the discrete Fourier transform [11, 12, 13]. However, the modified correlation metrics, which are more robust than the standard correlation, have no direct counterparts in the frequency domain. Moreover, it is not necessary that the correlation in the frequency domain is always faster than its spatial domain implementation, as discussed in Chapter 2.

1.2.3 Contribution of the Present Research

The present research proposes to enhance the efficiency and robustness of the classic correlation tracker by addressing all of its inherent problems mentioned in the previous subsection and the other real-world problems mentioned in Section 1.2.1.

The core of the visual tracking module in the proposed system is the edge enhanced BPNN-controlled fast normalized correlation (EE-BCFNC) algorithm. The *edge-enhancement* stage in the EE-BCFNC algorithm resolves the problems of *noise*, *object fading*, *obscuration*, and *varying illumination* in the scene. The edge-enhancement consists of Gaussian smoothing, gradient magnitude, normalization, and thresholding operations applied on the images to be correlated. The *normalized* correlation (NC) [58] makes the proposed tracker robust to the *varying illumination* in the scene and produces a normalized response in the range [0.0, 1.0]. The normalized response is exploited in the post processing stages, such as template updating and occlusion handling. The role of the BPNN (Back-Propagation Neural Network) in the EE-BCFNC algorithm is to predict whether the NC will be performed more efficiently using the direct method in the spatial domain or the FFT-SAT (fast Fourier transform and summed-area-table) method. The NC is then computed efficiently using the implementation technique suggested by the BPNN controller. The FFT-SAT method exploits the power of the FFT to efficiently compute the standard correlation in the frequency domain and the SAT [18] to normalize the resulting correlation surface very fast. The SAT is also known as the running-sum [16] or integral image [47, 58, 64, 65] in the computer vision literature. It is a very efficient technique to calculate the sum of the elements in any rectangular section in a matrix (or image) using only four algebraic addition operations.

Furthermore, an effective *template updating* scheme is proposed in order to make the tracker adaptive to the varying appearance of the object being tracked. It changes the template gradually with time using the history of the template and the current best-match. This template updating scheme also limits the *template drift* problem to some extent, and handles the *short-lived neighboring background clutter*.

The *varying scale* of the object is addressed by correlating three scales of the template with the search window, and selecting the scale that produces the maximum correlation value. The *long-lived neighboring background clutter* is handled by applying a weight on every pixel in the template using a 2D Gaussian weighting window with adaptive standard deviation parameters. The *template drift* problem is formally dealt with by adjusting the size of the best-match rectangle and relocating its position in the frame. The technique is accordingly named as the best-match rectangle adjustment algorithm, which also handles the *incorrect template initialization* by the user. Besides, a novel algorithm is introduced to dynamically determine the position and size of the search window using the prediction and the prediction-error of a Kalman filter. The search window is a small region (in the frame), where the probability of the presence of the target is high. The benefit of searching for the target in the small search window is that it reduces the processing burden on the system and it eliminates the false alarms due to the background clutter in the scene. Though the Kalman filter assumes a unimodal Gaussian noise distribution, the motivation behind its use in the present research is that it is simple and fast and offers adequate prediction accuracy for most of the real-world maneuvering targets (because of their inherent inertia). However, in order to further increase the prediction accuracy, the "constant acceleration with random walk model" instead of the most commonly used "constant velocity with random walk model" for the target dynamics is used in this research. It is demonstrated that the proposed visual tracking framework outperforms the traditional correlation tracker and, in some cases, the CONDENSATION [51, 52, 53, 54] and the mean-shift [43, 48] trackers.

1.3 Active Camera Tracking System

This section provides a brief introduction to the active camera tracking system, previous work, and the contribution of the present research.

1.3.1 Introduction

The active camera tracking system contains an *active* camera which moves automatically to the target using the target coordinates provided by a visual tracking algorithm. The motion of the camera is controlled by a pan-tilt unit (PTU) driven by a control algorithm. The control algorithm is responsible for generating the control signals for the PTU in such a way, that the target should remain precisely at the center of the video frame. If the PTU motion is not smooth and precise, the object in the video will oscillate to and fro around the center of the frame, and in the worst case the object may get out of the entire field of view (FOV) of the camera.

There are many prospective applications of an active camera tracking system. For instance, it can be deployed for precisely tracking and viewing a celestial body (e.g. satellite, star, etc.) with an automatically moving telescope, remotely monitoring an unattended child at home, performing surveillance of the enemy region by mounting the tracking system on an unmanned aerial vehicle (UAV), monitoring the movement of the objects in the strategic buildings and industries, automatically firing at the target with precision when the target is locked at the predefined track-point in the video frame, and so on.

Since the visual tracking algorithm has been introduced in the previous section, the focus of the next two subsections will be on the pan-tilt control algorithm.

1.3.2 Previous Work

Most of the time, the algorithm used to control a plant or system is the classic proportional-integral-derivative (PID) controller [56]. However, its design requires a mathematical model of the plant or system. Besides, it necessitates a sensitive and rigorous tuning of its proportional, differential and integral gain parameters. The tuning of the three parameters is very time consuming, if they are to be optimized for use with all the zoom levels of the camera in a tracking application. An alternative approach is to use a fuzzy controller [10, 59, 60, 61] that does not require the system model, but choosing a set of right membership functions and fuzzy rules calibrated for every zoom-level of the camera is practically very cumbersome. Another alternative is to implement a neural network controller [25, 62], but it is heavily dependent on the *quality* and the *variety* of the *examples* in the training dataset, which can accurately represent the complete behavior of the controller in *all* possible scenarios, including the varying zoom-levels of the camera. Furthermore, the traditional control algorithms, e.g. the one used in [14], are generally implemented based on the difference between the center (i.e. reference) position and the current target *position* in the image. They do not account for the target *velocity*. As a result, there will be oscillations (if the object is moving slow), a lag (if it is moving with a mediocre speed), and loss of the object from the frame (if it is moving faster than the maximum pan-tilt velocity *generated* by the *control algorithm*). The most relevant work to the proposed approach is the car-following control (CFC) law [15], which is very easy to implement and offers adequate robustness and accuracy. However, the main problem with the CFC is that it assumes that the current pan-tilt velocities of the PTU are available. Unfortunately, the PTU used in the current research is an open-loop system,

i.e. it does not feedback its current pan-tilt velocities. Therefore, the CFC law can not be used in its existing form.

1.3.3 Contribution of the Present Research

Keeping in view the limitations of the various control algorithms mentioned in the previous subsection, a predictive open-loop car-following control (POL-CFC) algorithm is proposed. Although its basic idea is borrowed from the car-following control (CFC) strategy [15], it does not assume the availability of the current pan-tilt velocities of the PTU. It simply: (1) considers that the current PTU velocity is the previous velocity generated by itself, (2) receives the predicted target coordinates from the visual tracking module, (3) estimates the predicted target velocity relative to the currently estimated PTU velocity, (4) estimates the velocity to be added into the current velocity of the PTU to generate the new velocity command, and (5) sends the new velocity to the PTU to move the camera to follow the target accurately in real-time.

A software application has been developed using multi-threading technique in LabVIEW (a graphical programming language by National Instruments [86]). The visual tracking algorithm is executed in one thread, while the pan-tilt control algorithm and the serial communication (between the PC and the PTU, and between the PC and the camera) are executed in another thread. This approach exploits the parallel processing power available in an off-the-shelf PC (e.g. P4 Centrino 1.7 GHz, 512 MB RAM). The visual tracking module has been actually implemented as a DLL (Dynamic Linked Library) using C/C++, which is invoked in one of the threads in the main LabVIEW application program. The camera, used in this research, is Sony FCB-EX780BP, which offers 1x to 25x optical zoom and serial interface for PC control. Since the output of the camera is an analog video signal, Dazzle DVC-90 Digital

Video Creator is used to digitize the video signal into a sequence of frames. The maximum frame rate, that the module can output, is 30 fps. The module can send 640×480 size frames, but it is configured to send 320×240 size frames in order to reduce the computational complexity without significantly sacrificing the robustness of the tracker. The PTU, used in this research, is Directed Perception PTU-D46 17.5W. It is a stepper motor PTU with configurable step size. The smallest step size, that it offers, is 0.01285 degree/step. Its maximum speed at this step size is 77.1 degree/second, which is enough for tracking most of the fast moving objects.

When the object is stationary or moving with no abrupt change in its *direction*, the proposed pan-tilt control algorithm centralizes the object in the video frame with 0% *overshoot*, 1.7 second *rise time*, and ±1 pixel maximum *steady state error* (at least for up to 6x zoom levels of the camera). These performance parameters of a control system are discussed in [56] and briefly defined in Section 4.3.4 for completeness.

1.4 A Vision Based System for a UGV to Handle a Road Intersection

This section provides an introduction to a machine vision system that enables a UGV (unmanned ground vehicle) to automatically handle a road intersection [57]. The previous work and the contribution of the present research are also discussed.

1.4.1 Introduction

Unmanned vehicles, e.g. UAVs (unmanned aerial vehicles) and UGVs (unmanned ground vehicles), are steadily growing in demand since they save humans from having to perform hazardous or tedious tasks and the equipment is often cheaper than the personnel. It further reduces cost to have unmanned vehicles remotely controlled by fewer remote operators by implementing autonomous robotics to partially assume the burden of control. UGVs in particular have been successfully used for

reconnaissance, inspection and fault detection, and active tasks like removal of dangerous explosives. These deployments have usually required the UGV to operate in relative isolation. However, future uses of UGVs will require them to be more aware of their surroundings. Deployment in an urban environment, for example, will require a UGV to behave within challenging constraints in order to avoid endangering or interfering with humans.

In order to foster the growth of research in practical autonomous UGVs, the United States defense research agency DARPA recently organized the Urban Challenge 2007 event, in which the participating organizations developed roadworthy vehicles that can navigate a mock urban obstacle course under complete autonomy. The original DARPA Grand Challenge event in 2005 required the UGVs to autonomously cross the Mojave Desert. The Urban Challenge 2007 event was more challenging since the UGV had to deal with a number of more difficult obstacles and constraints, such as parking in a confined space, following traffic laws, and avoiding interference with other vehicles on the same course.

1.4.2 Previous Work

Computer vision approaches have been successfully used in several previous UGV applications. For example, vision has been used to make the vehicle stay in its lane while driving on a road [88, 89], to detect unexpected obstacles in the road [90, 91, 92, 93, 94], to recognize road signs [93], and to avoid collisions with pedestrians [95]. Some research that enables multiple agents (UGVs and UAVs) to coordinate with each other to accomplish a task has also been reported [96].

1.4.3 Contribution of the Present Research

In this research, a new problem is highlighted and solved. That is, a UGV must be able to pass a street intersection regulated by a stop sign where vehicles from up to four directions are expected to voluntarily take turns crossing the intersection according to the order of their arrivals. In the DARPA Grand Challenge, the UGV prepared by Team UCF (University of Central Florida) was equipped with sweeping laser range finders to detect and avoid obstacles. However, these sensors can only detect objects along a single line in space, so they are ill-suited to the recovery of higher level information about the scene. Additionally, if the UGV travels on uneven roads, the laser range finders often point off-target. Cameras are preferable in this situation because they have a conical field-of-view (FOV). Thus, a computer vision system is proposed to solve the problem. The system hardware consists of three on-board computers and three cameras (mounted on top of the UGV) looking towards the other three roads merging at the intersection. The software in each computer consists of: (1) a vehicle detector (which detects any vehicle of any color and type on the other road), (2) the proposed tracker (which tracks the detected vehicle), and (3) a finite state machine model (FSM) of the traffic (which informs the status of the traffic at the corresponding road). The information from the three FSMs is combined to make an autonomous decision whether it is safe for the UGV to cross the intersection or not. The results of the actual UGV experiments are provided to validate the robustness of the proposed system.

1.5 Thesis Organization

The rest of the thesis is organized as follows. Chapter 2 reviews various correlation techniques for object localization in an *image*, and proposes the edge-enhanced BPNN-controlled fast normalized correlation (EE-BCFNC) method. The comparison

among all the correlation techniques with EE-BCFNC is also performed in this chapter. The proposed robust and real-time visual tracking framework to track an object in a *video* and its results are presented in Chapter 3. The proposed active camera tracking system (specifically the pan-tilt control algorithm to move the video camera) and its experimental results are presented in Chapter 4. The proposed machine vision system for a UGV to handle a road intersection and its experimental results are discussed in detail in Chapter 5. Finally, Chapter 6 concludes the thesis and presents the future directions.

1.6 Chapter Summary

Visual tracking is an important and challenging area of computer vision. There are many visual tracking algorithms, but they are either not robust to various real-world problems or they require too much computation time to be used in the practical real-time machine vision systems. In this thesis, a robust as well as real-time visual tracking algorithm is proposed which has been practically deployed in two important machine vision systems: an active camera tracking system and a system for a UGV to handle a road intersection. The correlation based object localization techniques, the visual tracking framework, and the two machine vision systems that use the visual tracking framework are individually discussed in detail in the following chapters.

2

Correlation Based Object Localization

2.1 Chapter Overview

This chapter answers the following questions. What is an object? How is it represented in a visual tracking paradigm? What is the correlation and what are its types? What are the pros and cons of the traditional correlation metrics? Then, an edge-enhanced BPNN-controlled fast normalized correlation (EE-BCFNC) algorithm is proposed. After that, a generic algorithm for localizing an object in a *single* frame is described. Finally, the EE-BCFNC technique is compared with all the other correlation techniques.

2.2 Object and Its Representation

In a visual tracking scenario, an object can be defined as anything that is of interest for further analysis [66]. The object that may be important to track in a specific domain can be a boat on the sea, a fish inside an aquarium, a vehicle on a road, a plane in the air, a person walking on a road, a bubble in the water, etc. Objects can be represented by their shapes and/or appearances [66].

The *shape* based representation of the object can be a point [67], a primitive geometric shape (e.g. rectangle, ellipse, etc.) [43], an object silhouette and contour [46], an articulated shape model [66], or a skeletal model [68, 69].

The *appearance* based representation of the object can be a probability density [43, 70, 71], a template [58, 72], or a multi-view model [73, 74, 75]. The probability densities of the object appearance features (e.g. color) can be computed from the image regions specified by the shape models (e.g. interior region of an ellipse or a contour). A template encodes object appearance generated from one view. Thus, it is suitable for tracking only the object, whose pose does not vary considerably during the course of tracking [66]. One limitation of multi-view appearance model is that the appearances of the object from all view angles are required ahead of time [66].

As far as the proposed correlation tracker is concerned, a rectangular template is used for the object representation. A template is basically a gray-level image of the whole (or part of the) object to be localized in the search image. An obvious advantage of a template is that it carries both the spatial and the appearance information [66]. The template is initialized by the user of the visual tracking system by extracting a rectangular patch from the initial frame. In order to overcome the limitation of the template mentioned above, it is updated according to the varying appearance of the object with time for robust and persistent tracking as discussed in Section 3.3.7.

2.3 Correlation Metrics

A correlation metric is used to determine the similarity of a small template of an object of interest with a candidate region in a search window. The search window is basically a small section (inside the video frame), where the likelihood of finding the object is high. If the expected location of the object is not already known, the whole frame can become the search window. Throughout the thesis, it is assumed that:

- The template and the search window are gray-level images,

- The template is represented by a matrix t of size $K \times L$ and the search window by a matrix s of size $M \times N$,
- K and L are odd integers to have a proper center of the template, and
- The template is smaller than or equal to the search window in size (i.e. $K \leq M$ and $L \leq N$).

There are four metrics usually used in the correlation-based tracking systems: standard correlation (SC), phase correlation (PC), normalized correlation (NC), and normalized correlation coefficient (NCC). In the following subsections, all these metrics are overviewed one by one with their pros and cons, and then the proposed edge-enhanced BPNN-controlled fast normalized correlation (EE-BCFNC) is introduced.

2.3.1 Standard Correlation (SC)

The 2D standard correlation (SC) metric in the spatial domain is given as [11, 13]:

$$c(m,n) = \sum_{i=0}^{K-1} \sum_{j=0}^{L-1} s(m+i, n+j) t(i,j) \tag{2.1}$$

where $c(m, n)$ is the element of the correlation surface (i.e. matrix) at row m and column n, where $m = 0, 1, 2, \ldots, M - K$, and $n = 0, 1, 2, \ldots, N - L$.

The SC metric can also be computed efficiently in the frequency domain as:

$$c = real\left[idft(S.T^*) \right] \tag{2.2}$$

where S and T are the 2-D discrete Fourier transforms (DFTs) of s and t, respectively. The superscript (*) over T indicates its conjugate, the dot operator (.) indicates the element-by-element multiplication, *idft*(.) is the 2-D inverse discrete Fourier transform function, and the *real*(.) function extracts the real part of a complex matrix.

The real part is extracted, because the imaginary part of the resulting complex matrix is almost zero, since s and t are real 2-D signals. Note that s and t must be appropriately zero padded before getting their transforms to obtain *true* (linear) correlation instead of *circular* correlation [87], because of the repeated-signal assumption by the *discrete* Fourier transform [13]. The minimum size of the zero-padded images must be $P \times Q$, where $P = M + K - 1$ and $Q = N + L - 1$. Once the correlation surface, c, is obtained, the highest peak, c_{max}, in the surface is found. The position of the peak in the surface is denoted by (m_{tl}, n_{tl}), which indicates the location of the top-left corner of the *best-match rectangle* (BMR) in the search window.

The main problem with the standard correlation is that it is highly sensitive to the illumination conditions, because it always produces c_{max} at the brightest spot in the search image. Furthermore, the correlation value is dependent on the size and content of the images, and is not normalized in the range [-1.0, 1.0]. Thus, an absolute measure of confidence is not obtained to be exploited in the later stages of the tracking algorithm (e.g. template updating, occlusion handling, etc).

2.3.2 Phase Correlation (PC)

Phase correlation (PC), also called symmetric phase-only matched filter (SPOMF), has also been used for registration and tracking [12, 19, 20, 21]. It is defined as:

$$c = real\left[idft\left(\frac{S}{|S|} . \frac{T^*}{|T|} \right) \right] \tag{2.3}$$

where |.| operator computes the magnitude of every complex number in its input matrix, and all the division and multiplication operations are computed *element-by-element*. In the phase correlation technique, the transform coefficients are normalized to unit magnitude prior to computing correlation in the frequency domain. Thus, the

correlation is based only on the phase information and is insensitive to changes in image intensity. It has an interesting property that it yields a sharp peak at the best-match position and attenuates all the other elements in the correlation surface to almost zero, but at the cost of being more sensitive to noise than SC [87]. Although this approach has proved to be successful, it has a drawback that all transform components are weighted equally, whereas one might expect that insignificant components should be given less weight [16]. It is shown in [22, 23, 58] and this thesis, that PC may produce false alarms and a very small peak (usually much less than 0.5) even at the correct position in the correlation surface. Furthermore, the value of the peak is highly dependent on the scene content. Therefore, it is very difficult to set a single threshold, which is needed to compare the peak value for template updating and other later stages of the tracking algorithm. The false-alarm rate can be reduced to some extent by phase-correlating the *edge images* of the search window and the template, rather than their gray-level images [12]. An alternative approach to minimize the false alarms is to modulate the gray-level images by an Extended Flat-top Gaussian (EFG) weighting function before phase-correlating them [63]. Some other methods to improve the performance of the phase correlation can be found in [80, 81, 82]. Nevertheless, these techniques do not eliminate the problem of unpredictable peak value and they do not make the PC as robust to the distortion in the appearance, shape, brightness, contrast, etc. of the object as the normalized correlation metrics discussed in the next subsections.

2.3.3 Normalized Correlation (NC)

In order to handle the limitations of SC and PC, some researchers, e.g. [12, 58], use the normalized correlation (NC):

$$c(m,n) = \frac{\sum_{i=0}^{K-1}\sum_{j=0}^{L-1} s(m+i,n+j)t(i,j)}{\sqrt{\sum_{i=0}^{K-1}\sum_{j=0}^{L-1} s^2(m+i,n+j)}\sqrt{\sum_{i=0}^{K-1}\sum_{j=0}^{L-1} t^2(i,j)}} \tag{2.4}$$

It may be noted that the numerator of NC is basically SC. The two normalizing factors are the square-roots of the energies of the candidate region [with its top-left position at (m, n) in the search image] and the template, respectively. This correlation metric has two salient features: (1) it is less sensitive to varying illumination conditions than SC, and (2) its values are normalized within the range [0.0, 1.0]. Therefore, further decision making is possible for template-updating, etc. However, its counterpart in the frequency domain does not exist, so it is computationally more intensive than SC or PC.

2.3.4 Normalized Correlation Coefficient (NCC)

This is the most commonly used correlation metric for object localization [11, 13, 16, 17, 79]. It is more robust to varying illumination conditions than NC, and its values are normalized within the range [-1.0, 1.0]. It is defined as:

$$c(m,n) = \frac{\sum_{i=0}^{K-1}\sum_{j=0}^{L-1} [s(m+i,n+j) - \mu_s][t(i,j) - \mu_t]}{\sqrt{\sum_{i=0}^{K-1}\sum_{j=0}^{L-1} [s(m+i,n+j) - \mu_s]^2}\sqrt{\sum_{i=0}^{K-1}\sum_{j=0}^{L-1} [t(i,j) - \mu_t]^2}} \tag{2.5}$$

where μ_s and μ_t are the mean intensity values of the candidate region [with its top-left coordinates at (m, n) in the search image] and the template, respectively. However, this metric has two disadvantages. Firstly, it requires that the intensity values of s or t must not be constant; otherwise, the correlation value will be infinity or indeterminate. However, this problem is not so serious in real-world imagery because of the inherent sensor noise. Secondly, its implementation in the spatial-domain is

computationally more intensive than even NC. However, there is an efficient method [16] to compute it using FFT and the concept of summed-area table (SAT) [18] or integral image [64, 65].

2.3.5 Edge Enhanced BPNN-Controlled Fast Normalized Correlation (EE-BCFNC)

It has been found out in this research that when the images to be correlated are first edge-enhanced, the NC metric outperforms even the NCC. The proposed EE-BCFNC is not a new correlation metric, but it is the combination of edge-enhancement (EE) and a fast implementation of NC (i.e. BCFNC). They are explained as follows.

2.3.5.1 Edge Enhancement (EE)

The edge enhancement operation is performed on the search window and the template before they are correlated. This technique makes the object localization algorithm robust to noise, varying lighting conditions, obscuration and object fading even in the low-contrast imagery. The proposed edge-enhancement process consists of four operations: Gaussian smoothing, gradient magnitude, normalization, and thresholding.

2.3.5.1.1 Gaussian Smoothing

It is a well-known fact that the video frames captured from any camera have noise in them – at least to some extent, especially when the ambient light around the sensor is low. If the frames are extracted from a *compressed* video clip instead of camera, they usually contain undesired artifacts (e.g. dim lines) in addition to noise. The smoothing process attenuates the sensor noise and reduces the effects of artifacts, resulting in less number of false edges in the subsequent operation (i.e. gradient magnitude).

The average filter could be used to attenuate the noise and artifacts in the images, but it introduces unwanted blur resulting in the loss of the fine detail of the object [13]. On the contrary, the Gaussian smoothing filter does the same job without

sacrificing the fine detail of the object [13]. Thus, a $w \times w$ Gaussian smoothing filter with standard deviation, σ_w, is applied on the search window and the template. It has been experimentally found out that $w = 7$ works fine in almost all scenarios. However, setting a value for σ_w is critical. If the value of σ_w is too low, the image pixels corresponding to the boundary coefficients of the Gaussian smoothing mask get too small weight, and the smoothing is not satisfactory. On the other hand, if the value of σ_w is too large, the image pixels corresponding to the boundary coefficients of the filter get too much weight, and the resulting image is too much smoothed (or blurred) to be acceptable. An effective formula [29] given below is exploited in this research for automatically calculating an optimum value of σ_w:

$$\sigma_w = 0.3\left(\frac{w}{2} - 1\right) + 0.8 \tag{2.6}$$

As a result, the effective coefficients for the Gaussian smoothing filter according to the size of the filter are obtained. Another desirable property of the resulting filter is that the sum of all the filter coefficients, which basically act as the weights of the image pixels under consideration, equals 1.

2.3.5.1.2 Gradient Magnitude

The edge-enhanced gray-level images instead of the actual gray-level images are used in this research in the correlation process, because edge-enhanced images are less sensitive to lighting conditions and they produce a cleaner correlation surface with less number of false peaks. In this regard, the standard horizontal and vertical Sobel masks [13, 30] are applied on the Gaussian smoothed image, and the two resulting images, E_h and E_v, are obtained Then, the gradient magnitude image, E, can be obtained as follows:

$$E(i,j) = \sqrt{E_h^2(i,j) + E_v^2(i,j)} \tag{2.7}$$

where i = 0, 1, 2, …, U - 1, j = 0, 1, 2, …, V - 1, where (U, V) = (K, L) for the template, and (U, V) = (M, N) for the search-window. Since Eq. (2.7) is computation intensive, its efficient approximation (given below) is actually used in this research, which produces almost identical result [13, 30].

$$E(i,j) = \left|E_h(i,j)\right| + \left|E_v(i,j)\right| \tag{2.8}$$

2.3.5.1.3 Normalization

It has been found out in this research that the *dynamic range* of the edge image, E, is often too narrow towards darker side as compared to the available pixel-value range [0, 255], especially in low-contrast imagery. Conventionally, the edge image is converted into a binary image using a predefined threshold; however, this approach does not work well in a template matching application, because the rich content of the gray-level edge-features of the object is lost in the process of binarization. In order to make the object localization algorithm robust to object fading and obscuration, which occur when the object is very far and the zoom level of the camera is set to a high value, the edges are enhanced using a normalization procedure given by:

$$E_n(i,j) = \left[\frac{255}{E_{\max} - E_{\min}}\right]\left[E(i,j) - E_{\min}\right] \tag{2.9}$$

where E_n is the normalized edge image, 255 is the maximum value a pixel can have, and $E_{\min}$ and $E_{\max}$ are the minimum and maximum values in the un-normalized edge image, E, respectively. The normalization stage effectively tries to stretch the histogram of the image in the whole range [0, 255], so the contrast between the object and the background is enhanced.

2.3.5.1.4 Thresholding

It has been found out through various experiments that the edges of the *object* in the *normalized* edge-images almost always have the values greater than 100 in any scenario. Nevertheless, in order to remain in the safe side and eliminate the false edges due to smoothed noise and artifacts, a thresholding operation is performed as:

$$E_{nt}(i,j) = \begin{cases} E_n(i,j) & \text{if } E_n(i,j) \geq 50 \\ 0 & \text{otherwise} \end{cases}, \tag{2.10}$$

where E_{nt} is the normalized and thresholded edge image. It may be noted that E_{nt} is not a binary image, but an edge-enhanced gray-level image adequately containing the important features of the object as illustrated in Figure 2.1. Figure 2.1(a) shows a 240×320 real-world image containing a small and dim helicopter having very low contrast with its background. Figure 2.1(b) is its edge image obtained by applying only the horizontal and vertical Sobel masks (i.e. without Gaussian smoothing, normalization, and thresholding). It may be noted that the edges of the object in this image are very weak and almost invisible, and that it contains the unwanted edges due to the noise and artifacts. Figure 2.1(c) illustrates how the proposed edge-enhancement operations have enhanced the edges of the object, eliminated the edges due to artifacts and noise, and enhanced the contrast between the object and the

(a) (b) (c)

Figure 2.1 Effect of the proposed edge-enhancement operations. (a) A 240×320 gray level image containing a very low-contrast (faded) object, (b) Edges of the image without using the proposed edge-enhancement operations, (c) Result of the proposed edge-enhancement operations

background.

2.3.5.2 BPNN-Controlled Fast Normalized Correlation (BCFNC)

Though NCC is the best correlation metric for the *actual gray-level* images, NC outperforms it for the *edge-enhanced* images according to the experiments performed during this research. Furthermore, computing the mean value for every candidate region of the search image is time-consuming in the NCC. Therefore, NC as defined in Eq. (2.4) is used in this research as the correlation metric for the edge-enhanced images, but with an efficient implementation. The technique is appropriately named as BPNN-Controlled Fast Normalized Correlation (BCFNC). It may be noted that the correlation surface yielded by BCFNC is the same as that by NC. The role of the BPNN is to predict whether the NC will be performed efficiently by the direct method described by Eq. (2.4) or by the FFT-SAT (fast Fourier transform – summed area table) method described in the next sub-section.

2.3.5.2.1 Efficient Implementation of NC Using FFT-SAT Method

This implementation of normalized correlation exploits the combined efficiency of FFT (Fast Fourier Transform) and SAT (Summed-Area-Table) [18]. Summed-area-table is also known as the *running sum* or the *integral image* in the computer vision literature [47, 58, 64, 65]. The same method has been exploited in [16], but for implementing the normalized correlation *coefficient* described by Eq. (2.5). The idea is that the numerator of Eq. (2.4) is computed in the frequency domain using Eq. (2.2), and the second normalizing factor (i.e. the square-root of the energy of the template) in the denominator of Eq. (2.4) is pre-calculated only once for each video frame. Since the first normalizing factor in the denominator of Eq. (2.4) varies with (m, n), it has to be calculated for every candidate region in the search image. For

efficient computation of all the local energies of the search window, the concept of summed area table (SAT) [18] is exploited.

The SAT of the $M \times N$ search window, s, is a matrix, I, of the size $(M + 1) \times (N + 1)$. The elements in its 0^{th} row and 0^{th} column are set to 0. All the other elements are efficiently calculated in a recursive manner as:

$$I(i, j) = s(i-1, j-1) + I(i, j-1) + I(i-1, j) - I(i-1, j-1), \qquad (2.11)$$

where $i = 1, 2, \ldots, M$, and $j = 1, 2, \ldots, N$. Once the SAT is computed, the sum of all the elements in any rectangular section in the search-window can be easily calculated by algebraically adding only the four corner elements of the corresponding rectangular section in its SAT. Specifically, in order to calculate the sum of elements contained in a $K \times L$ rectangular section (in the search window) with top-left element $s(i, j)$, top-right element $s(i, j+L-1)$, bottom-right element $s(i+K-1, j+L-1)$, and bottom-left element $s(i+K-1, j)$, then sum of all the pixels in the rectangular section is computed using the SAT of the search window very efficiently as:

$$sum = I(i + K, j + L) + I(i, j) - I(i + K, j) - I(i, j + K) \qquad (2.12)$$

Thus, the *local energies* of the search window can be determined by first obtaining the SAT of the *square* of the search window, and then computing the local sums of the *squared* search image using *its* SAT. The size of the resulting matrix containing the local energies is exactly same as that of the normalized correlation surface, c, in Eq. (2.4). If the square-roots of the elements in this matrix are multiplied with the pre-calculated "second factor in the denominator of Eq. (2.4)", a normalizing matrix is obtained. Finally, if the numerator of Eq. (2.4), which was computed using FFT, is divided by this normalizing matrix *element-by-element*, the *normalized* correlation surface, c, is determined.

2.3.5.2.2 Efficiency Comparison of FFT-SAT Method with Direct Method

Let t_f be the time (in ms) taken by the FFT-SAT method to compute NC between an $M \times N$ search window and a $K \times L$ template, and t_d be the time (in ms) taken by the direct method for the same operation as described by Eq. (2.4). Then, the *speed gain* of the FFT-SAT method relative to the direct method can be calculated as:

$$G = \frac{t_d}{t_f} \tag{2.13}$$

Furthermore, let S_t, S_s, and R_{ts} be defined as:

$$S_t = \sqrt{KL},\ S_s = \sqrt{MN},\ \text{and}\ R_{ts} = \frac{S_t}{S_s} \tag{2.14}$$

and assume that the numbers of rows and columns of the zero-padded images are integers greater than or equal to P and Q (defined in Section 2.3.1), respectively. It has been observed that G is a nonlinear function of S_t and R_{ts}, as illustrated in the surface plot shown in Figure 2.2. The surface plot has been obtained by experimentally acquiring the speed gain for S_s = 40, 80, 120, …, 600, and R_{ts} = 0.025, 0.05, 0.075, …, 1.0 for every value of S_s. If P and Q, individually, comes out to be power of 2, or if they individually contain only small prime factors (e.g. 2, 3, or 5), then the FFT computation becomes very efficient, and the *speed gain* is drastically increased as illustrated by various peaks in the surface plot. For example, when S_t is 153 and S_s is 360, R_{ts} becomes 0.425, and the size of the zero-padded images becomes 600×600. It may be noted that the integer 600 contains small prime factors: 2, 2, 2, 3, 5, and 5. In this example, t_d is 2629.6 ms, while t_f is only 66.2 ms. Thus, the speed gain (G) of the FFT-SAT method over the direct method is 39.72 (as illustrated by the highest peak in the middle of the surface plot and mentioned in Table 2.1). The flat valley (with the darkest blue color) in the surface plot in Figure 2.2 indicates $G \leq 1.0$,

while all the higher regions in the surface plot indicate $G > 1$. It shows that the FFT-SAT method can be sometimes slower than the direct method for computing NC. (This finding is contrary to the common notion that the FFT based correlation is always faster than the spatial domain correlation as the sizes of the images are increased). The reason behind this phenomenon is explained as follows.

In this research, the *valid* correlation of size $(M-K+1)\times(N-L+1)$ is performed as mentioned in Eq. (2.1), instead of the *full* correlation of size $(M+K-1)\times(N+L-1)$, because the object is expected to be *inside* the search image (and not outside it). If the correlation is performed in the frequency domain, the search image and the template has to be zero-padded to the size at least $(M+K-1)\times(N+L-1)$ before computing their FFTs, regardless of full or valid correlation. If the zero-padding of the images is not performed, the undesired wrap-around effect will be obtained in the correlation result. Therefore, when template size is too large, the FFT computation of the two large zero-padded matrices becomes time consuming. On the contrary, the correlation performed in the spatial domain works directly on the original (i.e. $M\times N$ and $K\times L$) images and it has to find the matching score only at $(M-K+1)\times(N-L+1)$ positions. Thus, the spatial domain NC becomes faster than the FFT-SAT based NC, when the ratio of the template size to the search window size is large (near 1.0).

In order to get the best from the two approaches, the proposed method does not use a single approach for all cases, but switches between the two implementations according to the decision of a Back-propagation Neural Network (BPNN) controller.

2.3.5.2.3 BPNN Controller

A table of decisions (when to use direct or FFT-SAT implementation) could be made from the data that was used to generate the surface plot shown in Figure 2.2, but the table could not provide the decisions for the arbitrary sizes of the template and the search window. Similarly, some analytical function could be obtained to provide the decision, but it was difficult to find a good analytical function, because the FFT function in OpenCV library [29] (which was being used in all the experiments) does not exploit a single approach to compute FFT for all sizes of the images. Thus, in this research, the two implementations of the NC were considered as black boxes, the actual time taken by each implementation was listed in a table for some sizes of the images (as discussed in the previous subsection), and a BPNN controller was trained on the observations. As a result, the BPNN could predict which implementation of NC will perform faster for the current sizes of the images at hand, before actually computing the correlation. A question may arise at this point. Why the BPNN was

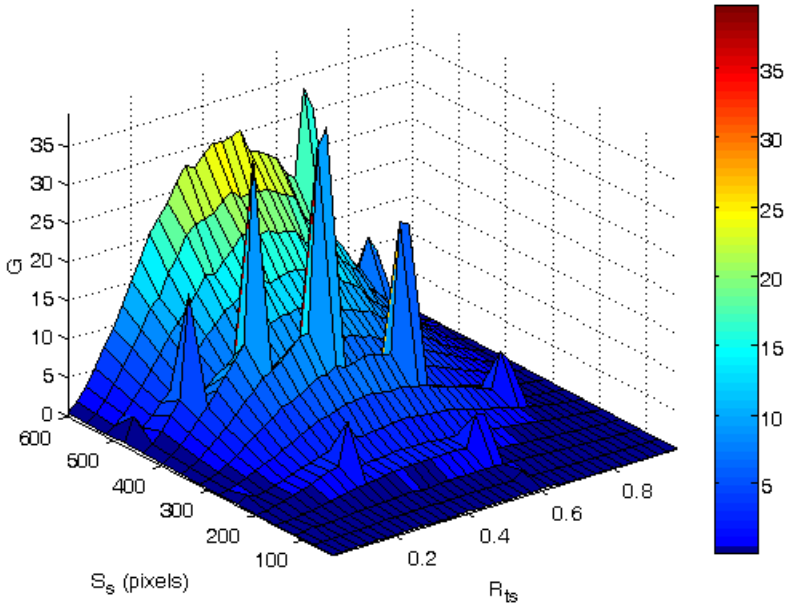

Figure 2.2 Surface plot of G as a function of R_{ts} and S_s , where G is the speed-gain of FFT-SAT method of NC implementation relative to the direct method, R_{ts} is the ratio of template-size to search-window-size, and S_s is the search-window-size.

used instead of other neural networks? The answer is that the BPNN can *easily* learn a *non-linear* multi-dimensional classification/approximation problem, while others may not [25, 26, 7, 8].

The neural network was trained on the experimental data, which was used to generate the non-linear surface plot in Figure 2.2. It may be noted, that the surface plot was generated using only three parameters (i.e. S_s, R_{ts}, and G), and that the *pixels* of the images were *not* used for creating the surface plot or for training the neural network. The architecture of the designed BPNN is shown in Figure 2.3. It contains an input layer, a hidden layer, and an output layer. The input layer has *only* two nodes (i.e. $m_0 = 2$), because the input pattern **p** consists of *only* two scalar elements, as described in Eq. (2.15). The output layer has one neuron (i.e. $m_2 = 1$), because the BPNN is supposed to output a single binary decision (either a positive or a negative value). The number of neurons in the hidden layer depends on the difficulty level of the mapping or classification problem at hand. The problem at hand was satisfactorily solved using only 20 hidden neurons (i.e. $m_1 = 20$). The activation function of the neurons in the hidden layer and the output layer was chosen to be the tangent-sigmoid

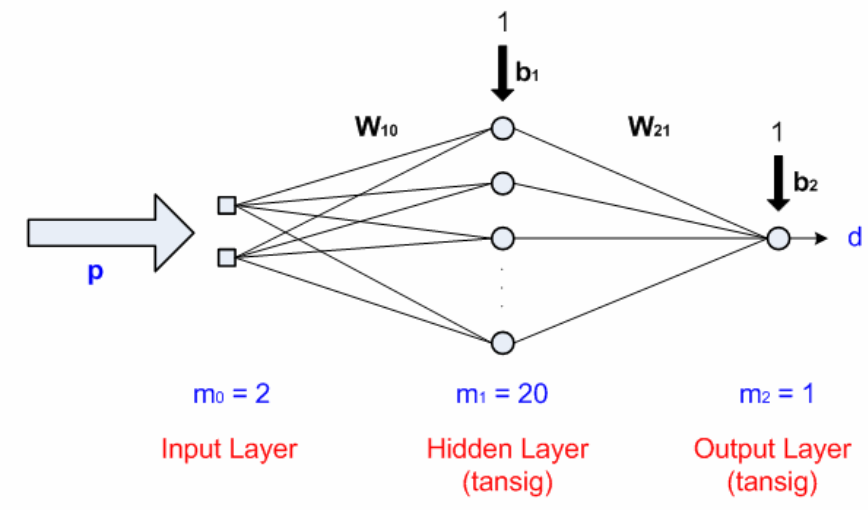

Figure 2.3 The proposed architecture of the BPNN classifier, where tansig is the activation function used for the neurons in the hidden and the output layers [see Eqs. (2.16) and (2.17)].

function. This activation function was used, because it is non-linear and it supports negative as well as positive values [24, 25, 26]. The non-linearilty requirement is necessary to solve a non-linear classification problem. The support of positive and negative values in the activation function speeds up the learning process of the neural network [26]. The training of the BPNN was carried out using the efficient *scaled-conjugate gradient learning algorithm* [27]. This algorithm is far more efficient for training a BPNN than any of the conventional learning algorithms, e.g. gradient descent method [24]. The proposed neural network architecture accepts a pattern (**p**) as its input, defined as:

$$\mathbf{p} = \left[\frac{S_S}{600}, \quad R_{ts} \right]^T \tag{2.15}$$

where the S_s is normalized by 600, which is the maximum value of S_s in the experimental data. The normalization is necessary, since the input layer of the neural network assumes that the values in the input pattern are in the range [0.0, 1.0]. Thus, the maximum size of the search window, that the designed BPNN can support is 600×600 pixels. This constraint is not of much significance, because the video frame is of size 320×240 pixels only, and the search window is normally much smaller than even the frame. Since the training was performed in a supervised manner, the ideal output for each example was provided in the training dataset. The ideal output was a scalar value: either +0.8 or -0.8. The scalar values ±1 could be used instead of ±0.8, respectively, but that approach would have caused slow learning [26], because the tansig(.) activation function is saturated at ±1, as shown in Figure 2.4.

Once the training is completed, the neural network is ready to be a fast decision maker. The decision output, *d*, of the trained BPNN is easily determined as:

$$d = \text{tansig}\left[\mathbf{W}_{21}.\text{tansig}\left(\mathbf{W}_{10}.\mathbf{p} + \mathbf{b}_1\right) + \mathbf{b}_2\right] \tag{2.16}$$

where $\mathbf{W}_{10}$, $\mathbf{b}_1$, $\mathbf{W}_{21}$, and $\mathbf{b}_2$ are the $m_1 \times m_0$, $m_1 \times 1$, $m_2 \times m_1$, and $m_2 \times 1$ matrices, respectively. Each row of $\mathbf{W}_{10}$ contains the learnt synaptic weights of its corresponding neuron in the hidden layer. The elements of the row vector $\mathbf{W}_{21}$ are the synaptic weights of the output neuron. The column vector $\mathbf{b}_1$ contains the bias weights of the neurons in the hidden layer, and $\mathbf{b}_2$ is the bias weight of the output neuron. All these synaptic weights are adapted and optimized according to the training dataset during the learning phase of the neural network. The tansig(.) function, as defined in Eq. (2.17) and illustrated in Figure 2.4, is basically a fast approximation of the well-known tanh(.) function [28].

$$\text{tansig}(n) = \frac{2}{1 + e^{-2n}} - 1 \tag{2.17}$$

The output of the BPNN (i.e. d) will be either a positive or a negative value. If $d > 0$, the FFT-SAT method of computing NC will be faster than its *direct* method; and vice versa, if $d < 0$. The response of the BPNN has been tested with all the patterns from its training dataset, and the resulting surface plot is shown in Figure 2.5.

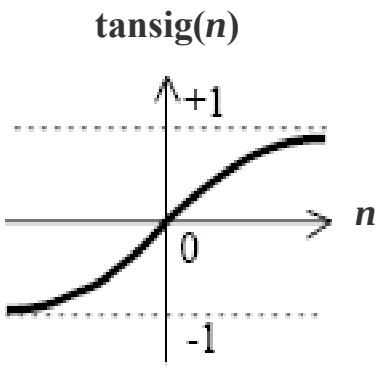

Figure 2.4 Tangent sigmoid activation function

If the surface plots in Figures 2.2 and 2.5 are compared with each other, it can be observed that all the darkest blue regions at the valley (where $G_p \leq 1$) in Figure 2.2 corresponds to all the blackish regions (where $d < 0$) in Figure 2.5. Similarly, all the higher regions (where $G_p > 1$) in Figure 2.2 correspond to all the whitish regions (where $d > 0$) in Figure 2.5. Thus, the BPNN controller has produced the correct decisions in all cases. In fact, the BPNN is well *generalized*, because it can produce the right decisions, even for those input patterns, which were not included in its training dataset. This is, because the mean square error of 0.01 (which is quite high) was used as the error goal during the training phase of the BPNN, so the BPNN did not *over-fit* to the *training* dataset. The BPNN decisions and their validations for some examples of the sizes of the images are listed in Table 2.1. It may be noted that t_d is the time taken by the optimally coded function for *direct* method of NC available in OpenCV b4 [29] and t_f is the time taken by the FFT-SAT implementation of NC. The

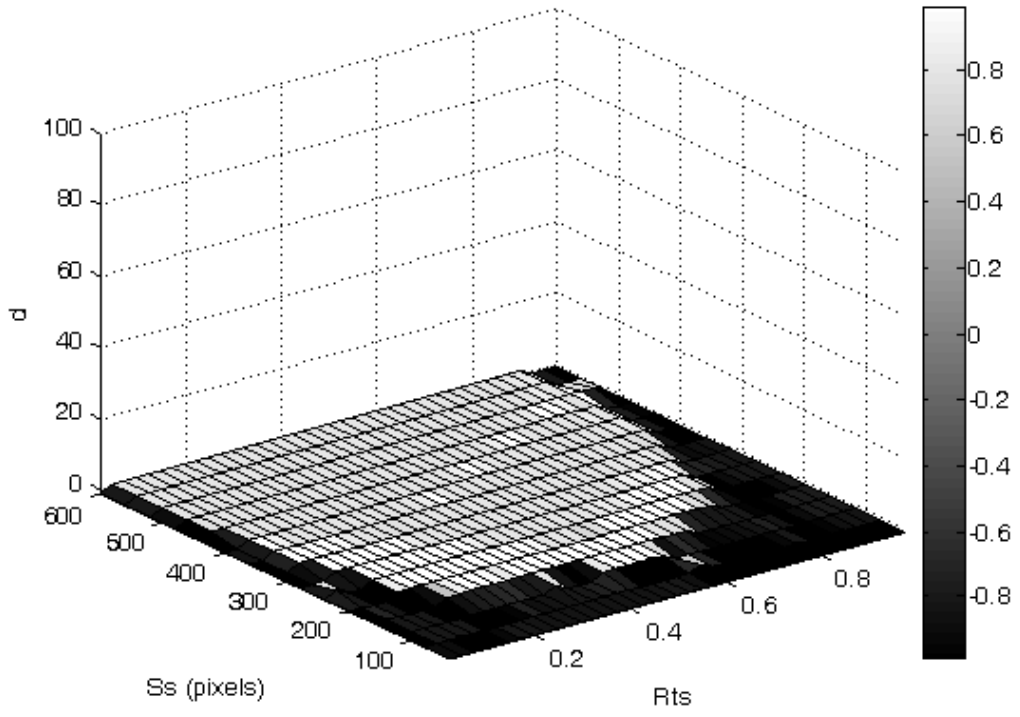

Figure 2.5 Surface plot showing the decisions made by the BPNN classifier when it was provided with various combinations of the search-window-size and the size-ratio as 2-element input patterns.

value of G_p is machine independent, because it is a ratio of the two elapsed times and both of the implementations are executed on the same machine. The downward arrow (↓) and the upward arrow (↑) indicate d < 0 and d > 0, respectively. The testing was carried out on a PC having P4 Centrino 1.7 GHz processor and 512 MB RAM. The value of G_p, for every case listed in Table 2.1, validates the corresponding decision (d) of the BPNN. At first sight, it may seem that the direct spatial-domain implementation is applied rarely. However, it is the one, which is applied frequently, especially when the template size is small in case of distant object tracking, or when the template size is very large in case of nearby smoothly moving object.

2.4 Generic Correlation Based Object Localization Algorithm

No matter which correlation technique is used, the basic algorithm for localizing an object (or target) in a frame is the same in every case. It is described in the following simple steps.

Step 1 Prepare the search window (i.e. s) and the template of the target (i.e. t).

Step 2 Compute the correlation surface, c, using SC, PC, NC, NCC, or the proposed

Table 2.1 BPNN decision, d, and its validation, G, for some sizes of the images

$M \times N$	$K \times L$	R_{ts}	d	t_d (ms)	T_f (ms)	G
50×50	30×30	0.6000	↓	0.8	3.2	0.25
75×75	25×25	0.33	↓	4	8.81	0.45
320×240	10×10	0.036	↓	28.68	82.28	0.35
320×240	51×51	0.18	↑	260	80	3.25
320×240	75×75	0.27	↑	450	90	5
320×240	100×100	0.3610	↑	601.8	100.4	5.99
320×240	125×125	0.44	↑	681	100	6.81
320×240	300×200	0.884	↓	135.2	282.4	0.48
360×360	153×153	0.4250	↑	2629.6	66.2	39.72
512×512	60×30	0.0820	↑	776.34	317	2.45
512×512	205×205	0.4	↑	7631	390	19.56
640×480	400×300	0.6245	↑	10111	701	14.42

EE-BCFNC.

Step 3 Locate the peak value c_{max} in the correlation surface, and denote its position by (m_{tl}, n_{tl}), where m_{tl} and n_{tl} are the row and the column coordinates of the top-left position of the best-match rectangle (BMR) in the search-window, respectively.

Step 4 Locate the center of the BMR using:

$$(m_c,\ n_c) = \left(m_{tl} + \frac{K-1}{2},\ n_{tl} + \frac{L-1}{2} \right) \tag{2.18}$$

Step 5 Let the position of the top-left pixel of the search window in the frame be (x_s, y_s), where x_s and y_s are the column (i.e. horizontal) and row (i.e vertical) coordinates relative to the frame origin (0, 0), respectively. Then, locate the center of the BMR with respect to the *frame origin*, as:

$$(x,\ y) = \left(x_s + n_c,\ y_s + m_c \right), \tag{2.19}$$

where (x, y) is the center of the target in the current frame, assuming that the target is at the center of the BMR. If the object is to be searched for in the whole frame instead of a small search window, then $(x_s, y_s) = (0, 0)$ and $(x, y) = (n_c, m_c)$.

2.5 Comparison among Different Correlation Techniques

In this section, the performance of different correlation-based template matching techniques (discussed in this chapter) is compared. A challenging search image as shown in Figure 2.1(a) is selected as test image, because it contains a very distant and dim object (a helicopter) in a hazy scene. The objective is to determine the location of the object in the search image. A 21×23 template of the object is shown in Figure

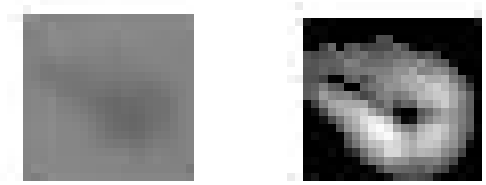

(a) (b)

Figure 2.6 The 21×23 templates (shown enlarged for easy view). (a) Original, (b) Edge-enhanced.

2.6(a). The correct top-left position of the object in the search image is at (m_{tl}, n_{tl}) = (169, 224). The correlation technique, which produces a clean peak exactly at this location in the resulting correlation surface, will be considered the best one.

Figure 2.7(a) illustrates the correlation surface obtained, when the original template was correlated with the original search image using SC given by Eq. (2.1) or Eq. (2.2). This method failed to locate the correct position of the object, because it produced the highest peak of 8,871,601 value at (10, 11) instead of (169, 224). Additionally, it has produced many other (false) peaks at all those spots, which were brighter than the object in the search window. In fact, the correlation value is lower (i.e. 8,226,021) at (169, 224) position, where the object actually lies, since the object is darker than the background. Moreover, the correlation values are not normalized in the range [0.0, 1.0] or [-1.0, 1.0].

Figure 2.7(b) shows the correlation surface obtained, when the original template was correlated with the original search image, using PC described in Eq. (2.3). The method failed to locate the correct location of the object, because it produced the highest peak at (10, 11) instead of (169, 224). It may be noted, that the highest peak value is only 0.14, and there are also some other lower peaks (including the true peak illustrating the location of the target).

Figure 2.7(c) illustrates the correlation surface, which is the result of matching the original template with the original search image using NC given by (2.4). The object is located correctly at (169, 224), and the highest peak has value of 1.0. However, if the surface is observed closely, it can be found that the minimum correlation value in the whole surface is also too high, i.e. 0.9945. This behavior of

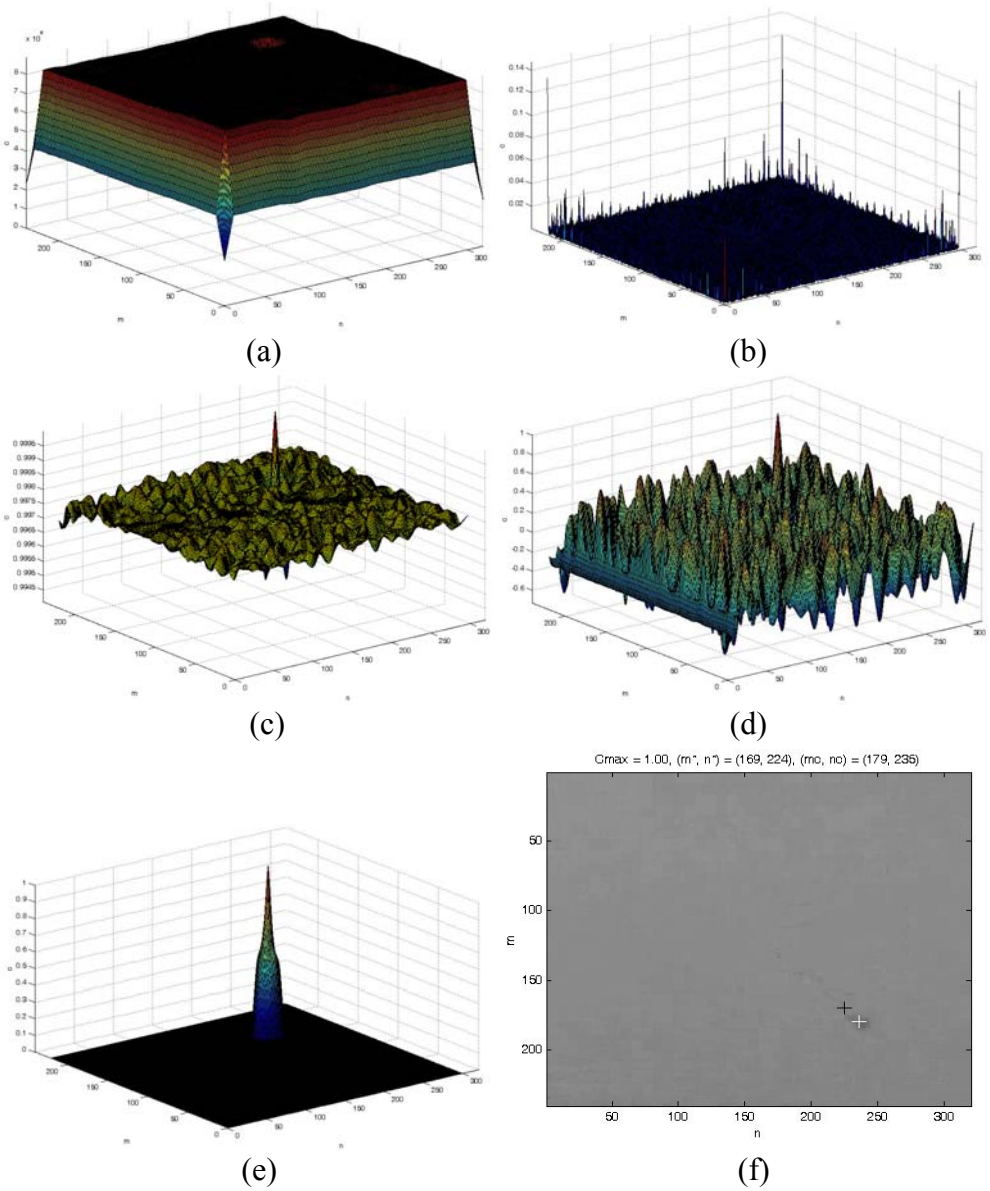

Figure 2.7 Results of various correlation-based object localization methods. (a) SC surface, (b) PC surface, (c) NC surface, (d) NCC surface, (e) Proposed EE-BCFNC surface, and (f) Overlay of the + signs on the target coordinates (correctly found by NC, NCC and EE-BCFNC methods) on the search-window, where the black sign represents the top-left coordinates (m_{tl}, n_{tl}) of the best-match and the white sign represents its center-coordinates (m_c, n_c).

NC with original gray level images may result in the detection of a wrong target instead of the true target in cluttered environment. It will be seen at the end of this section, that this problem with the NC is eliminated, if the images are edge-enhanced before they are correlated with each other.

Figure 2.7(d) depicts the correlation surface obtained, when the original template was correlated with the original search-window, using NCC given by Eq. (2.5). This method also detects the correct position of the target at (169, 224) with the peak correlation value of 1.0. There are various other positive and negative peaks within the range [-1.0, 1.0], but their values are not near the highest peak value, as they were in the NC approach in case of original images.

Finally, Figure 2.7(e) illustrates a nice and clean correlation surface resulting from the proposed EE-BCFNC method, in which the edge-enhanced template shown in Figure 2.6(b) is correlated with the edge-enhanced search image shown in Figure 2.1(c). It is clearly shown in the surface, that there is only one peak with the correlation value of 1.0 exactly at (169, 224) position and all the other values in the surface are zero or well below the highest peak value.

Figure 2.7(f) shows the exact location of the helicopter detected by NC, NCC and EE-BCFNC. The position of the top-left corner of the BMR is shown by the black cross-hair at (m_{tl}, n_{tl}) = (169, 224), while the position of the center of the BMR is indicated by the white cross-hair at (m_c, n_c) = (179, 235).

The comparison analysis has validated the earlier discussion that the best correlation surface is produced by the proposed EE-BCFNC algorithm.

2.6 Chapter Summary

An object can be represented by its shape (e.g. ellipse) or appearance (e.g. template). Correlation based object localization technique looks for a region in the search image, which matches best with the template of the object. The template matching process can be performed using any of various correlation metrics, such as standard correlation (SC), phase correlation (PC), normalized correlation (NC), and normalized correlation coefficient (NCC). Every metric has its own pros and cons. In order to address the limitations of these metrics, an edge-enhanced BPNN-controlled fast normalized correlation (EE-BCFNC) technique is proposed. The algorithm for localizing an object in a *single* frame is quite generic, regardless of the choice of the correlation technique used for the matching process. The results of the comparison among these correlation techniques validate that the proposed EE-BCFNC technique outperforms all the other methods by efficiently producing a clean normalized correlation surface with a dominant peak at the object location. The next chapter discusses the proposed visual tracking framework, which can track an object of interest in the consecutive frames of a *video*, and handles the real-world problems, such as incorrect template initialization, template-drift, occlusion, varying shape of the object, etc.

3

Visual Tracking Framework

3.1 Chapter Overview

This chapter discusses the proposed visual tracking framework and tests it on various videos obtained from the public datasets, such as CAVIAR, PETS, and AV16.3. Additionally, for some other public test videos, the results of the proposed tracker are compared with those of the CONDENSATION [52, 53, 54] and the mean-shift [43, 48] trackers reported in [51]. The proposed correlation tracker is also compared with the traditional correlation tracker at the end of the chapter.

3.2 Challenges for a Visual Tracking Algorithm

Visual tracking can be simply defined as the problem of estimating the trajectory of an object of interest as it moves around the scene in a video [66]. It is a very complex problem for the computer vision community, because of the:

- *Loss of information* due to the projection of the 3D world on a 2D image,
- *Noise in images* due to sensor noise and low illumination conditions,
- *Background clutter* due to other similar or different objects in the scene,
- *Complex object motion (slow, fast, linear, and nonlinear)*,
- *Object fading* due to high-zoom operation of the moving camera in cloudy environment,

- *Obscuration* of the object due to smoke, dust, or fog,
- *Intermittent occlusions* due to other objects hiding the target,
- *Complex object shape variations* during its maneuvering,
- *Change in the object scale* due to its varying distance from the camera or varying zoom level of the camera,
- *Uneven scene illumination*, and
- *Real time processing requirements*.

Additionally, there is a severe problem of *template-drift*, if the tracking is performed using a basic correlation method. Due to this problem, the object tends to drift away from the template with time. Ultimately, it gets out of the template and the tracking becomes a complete failure.

The basic object localization algorithm, given in Section 2.4, is for localizing an object in only a *single* frame when a good template of the object is already present. It can not solve the practical problems listed above. Therefore, an efficient visual tracking algorithm is proposed to explicitly address all of these problems.

3.3 Proposed Visual Tracking Framework

A simplified flowchart of the proposed visual tracking algorithm is shown in Figure 3.1. The individual blocks of the flowchart are discussed in the following sub-sections.

3.3.1 Video Frame Acquisition

If the tracking is performed off-line on an image sequence or the video frames coming from a digital video camera, the individual frames can be acquired easily in the software. However, if the tracking is performed on the video coming from a live analog camera, the digital frames can be acquired using a digitizer module, such as

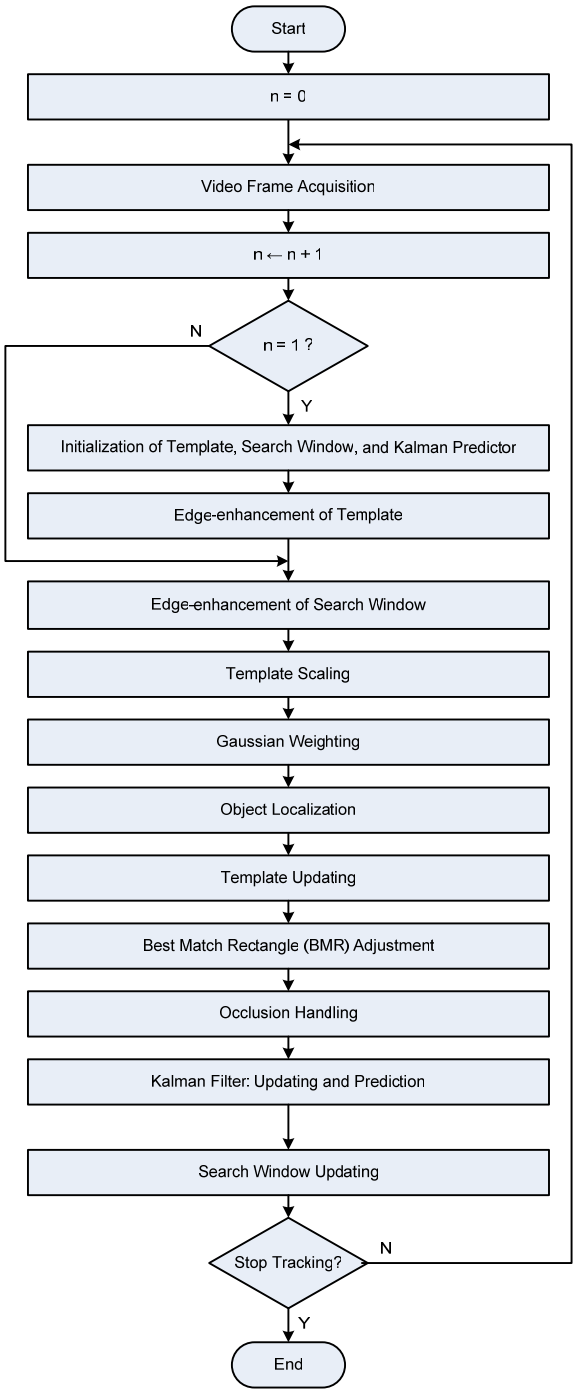

Figure 3.1 Flow chart of the proposed visual tracking algorithm

Dazzle DVC-90. The video camera used in the present research is Sony FCB-EX780BP. The Dazzle DVC-90 module can digitize the video into a frame sequence each of size 640×480, but it is configured to provide each frame of size 320×240 in order to: (1) reduce the computational complexity for real-time processing of the

frame without significantly sacrificing the robustness of the tracker, and (2) efficiently encode the processed frame for video recording purpose. The DVC-90 module can digitize the analog video with a maximum frame rate of 30 fps, which is quite adequate for tracking a physical object moving with significant velocity and maneuvering. Each frame is an RGB color image, but it is converted into gray-level image in order to further reduce the computational burden on the system.

3.3.2 Initialization of Template, Kalman Filter, and Search Window

At the start of the tracking session, the template, the Kalman filter, and the search window are initialized as described in the following sub-subsections.

3.3.2.1 Template Initialization

The template is initialized by the user of the tracking system by selecting any object of interest (or its salient part) appearing in the video. In order to have a long and good tracking session, the *traditional* trackers require that:

- The object should be well centered in the extracted template, if full object is selected, or
- The template should be extracted from the middle region of the object, if a part of the object is to be tracked.

However, it is usually difficult for the user to extract a good template during the motion of the maneuvering object in the *streaming* video coming directly from a camera. In order to eliminate the above-mentioned requirements, a best match rectangle (BMR) adjustment algorithm is proposed in Section 3.3.8.

3.3.2.2 Kalman Filter Initialization

The center of the region, from where the template is extracted, is used to initialize the target coordinates in the frame, (x, y), where x represents the column index and y the row index of the matrix representing the frame. The *measurement vector* (defined in Section 3.3.10) of the Kalman filter is initialized with these target coordinates instead of (0, 0). This strategy is exploited to reduce the initial error of the Kalman filter and expedite the convergence of the filter to the trajectory of the target. Further detail of the filter, including its benefits in the proposed tracker, is given in Section 3.2.10.

3.3.2.3 Search Window Initialization

The center of the initial search window is considered to be at the initial target coordinates, and the size of the window is initialized to be three times that of the initial template to accommodate the unknown velocity of the target at the start of the tracking session. After the convergence of the Kalman filter, the search window will be appropriately updated using Kalman prediction and its error, as discussed in Section 3.3.11.

3.3.3 Edge-enhancement of Template and Search Window

The edge enhancement operation is proposed to be performed on the search window and the template before correlating them. This technique makes the object localization algorithm robust to noise, varying lighting conditions and object fading even in the low-contrast imagery. The detail of this operation is given in Section 2.3.5.1.

3.3.4 Template Scaling

The moving object can get larger (or smaller) with time in the video frames, when the object comes nearer to (or goes farther from) the camera, or when the zoom level of the camera is increased (or decreased). If the template size is kept constant throughout

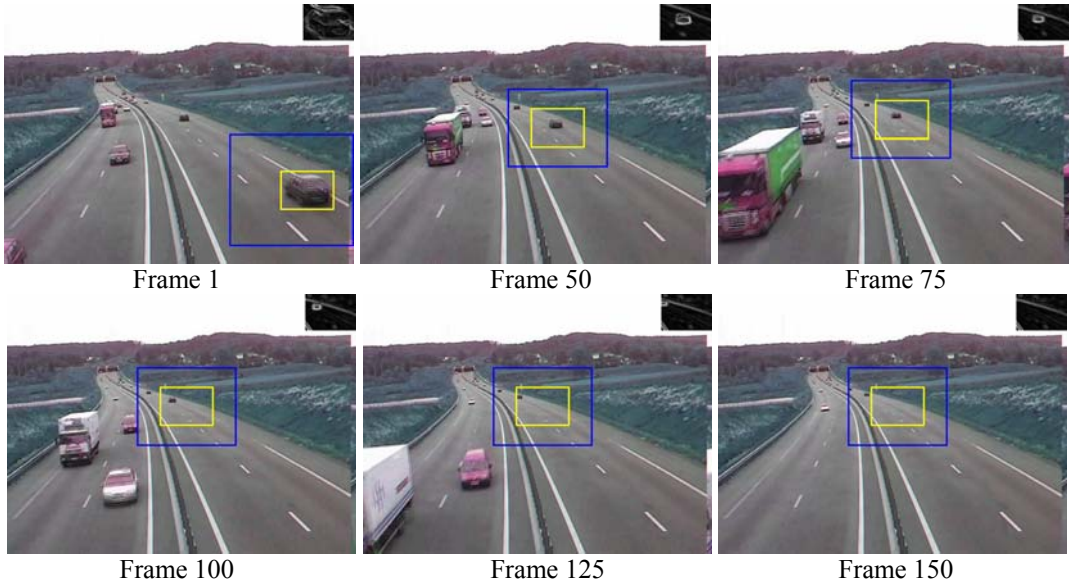

Figure 3.2 Tracking a car going away from the camera without using template scaling stage. The yellow rectangle represents the best-match rectangle, and the blue rectangle represents the dynamic search window (discussed in Section 3.3.11). Since the template size is fixed and the size of the car is reducing with time, the background becomes more dominant than the car being tracked. As a result, the tracker starts tracking the background instead of the car from 75th frame.

the tracking session, it may create two problems: (1) when the object gets smaller, the background pixels will invade into the fixed-size template and the template will represent the background more than the object, and (2) when the object gets larger, the fixed-size template will be representing only a very small part of the object, and it will not contain adequate pixels of the object to make it distinctive from the other objects in the background clutter. Due to these problems, the template can match with clutter more than it does with the actual object. As a result, the false alarm rate will be high, resulting in the failure of the tracking session. This situation is illustrated in Figure 3.2, in which a car is moving away from the camera, so it becomes smaller with time. Since the template size is fixed throughout the tracking session, the contribution of the car in the template becomes less significant than that of the background as the time progresses. As a result, the tracking algorithm starts tracking the background (instead of the car) from 75th frame and lets the car go out of the template in the subsequent frames.

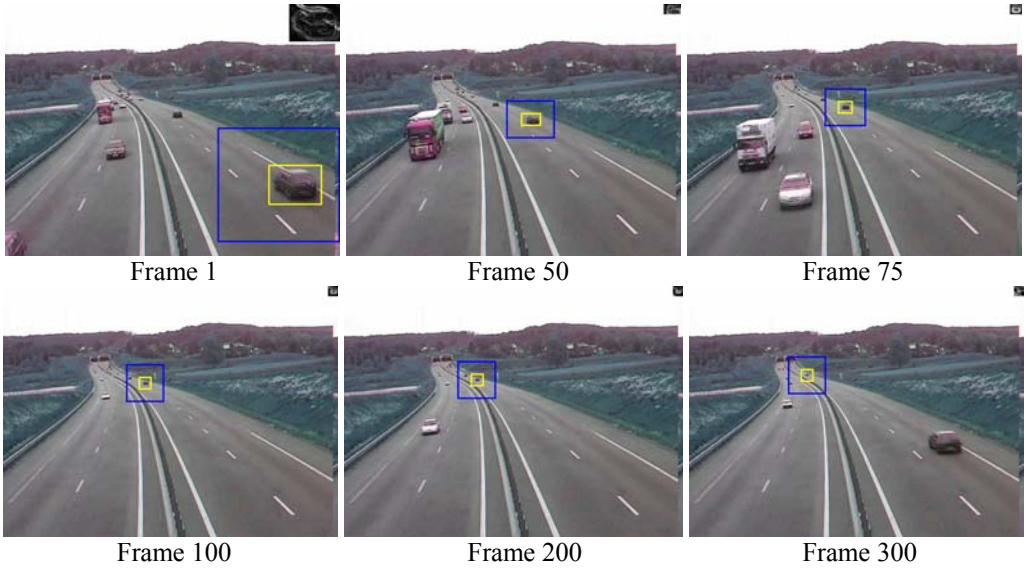

Figure 3.3 Illustration of the scale-handling capability of the proposed visual tracking algorithm. A car is being tracked successfully, even when the scale of the car is being reduced due to its ever-increasing distance from the camera. It can be seen that if the template is reduced in size with time, the dynamic search window is also reduced. Thus, three benefits are obtained: scale handling, more background clutter rejection and less processing burden on the system.

In order to handle the varying scale of the object, a fact about the highest peak in the correlation response is exploited. That is, the correlation peak is high if the scale of the object in the *template* is same as that of the object in the *search window*; otherwise, the peak is low. Thus, the search window is correlated with three scales of the template: 110%, 100%, and 90%. The 100% scale of the template is the original one, which comes from the previous iteration. As a result, three correlation surfaces with the corresponding three peaks are obtained. The best-match rectangle (BMR) corresponding to only that template scale, which produces the highest of the three peaks, is accepted. Thus, the template scale for the next iteration is updated according to the current scale of the object and the tracking becomes persistent. It may be noted that the minimum and the maximum size limits on the template are applied in order to have robust tracking and decrease the computational complexity, respectively, as discussed in Section 3.3.8. Figure 3.3 shows how the varying scale of the car in the same video shown in Figure 3.2 is handled appropriately to have a persistent tracking

session. It may be noted that this scale handling technique can work with any correlation metric or/and actual gray-level images.

3.3.5 Gaussian Weighting of Template Pixels

The *background clutter*, which is far from the object in the scene, is handled by looking for the object only inside a small search window (see Section 3.3.11) instead of the whole frame. However, the search window does not handle the *neighboring clutter*, which may be present immediately around the object *inside* the template.

There are two kinds of neighboring clutter: short-term and long-term. In order to clarify the difference between them, suppose there is a *big* picture hanging on a wall in the video and there is a person (whose head is the target of interest) appearing from the right side of the video and walking towards left. If the person passes the picture *without* standing in front of it, the content of the picture appearing around the head of the person will behave as a short-term neighboring clutter, because the content can be part of the template only for a very short duration. However, if the person stands in front of the picture for a *long* duration, the content of the picture appearing around the head of the person will behave as a long-term neighboring clutter, because the content will be part of the template for a long duration.

The effect of the short-term neighboring clutter is efficiently diminished by temporally smoothing the template (discussed in Section 3.3.7), but the long-term clutter is not handled by the filter. Therefore, the effect of the long-term neighboring clutter is decreased by assuming that the object is at the center of the template (due to the *best-match rectangle adjustment* algorithm discussed in Section 3.3.8) and applying a weight on every pixel in the template. The farther the pixel from the center of the template, the lower the weight it gets. Specifically, a 2D Gaussian weighting function with standard deviation parameter as a function of the size of the template is

used. This way, the object pixels, which are assumed to be at or near the center of the template, will take part in the correlation process more actively as compared to the long-term neighboring clutter pixels, which are assumed to be far from the center of the template. The appropriate values for the two standard deviation parameters of the 2D Gaussian function are calculated using Eq. (2.6).

3.3.6 Object Localization

Once the three scales of the edge-enhanced template are obtained, the corresponding 2D Gauussian weighting window is applied individually on every scaled template, and the search window is edge-enhanced, the object is localized in the frame very efficiently using the BPNN-controlled fast normalized correlation (BCFNC) proposed in Section 2.3.5.2. It may be noted, that the search window is correlated individually with every scale of the template. As a result, three correlation surfaces and the three corresponding highest peaks in those surfaces are obtained. The values of the three correlation peaks are then compared with one another, and the surface which provides the highest peak is selected. The location of the peak in the selected surface determines the location of the top-left vertex of the best-match rectangle (BMR) in the search window. The BMR has the width and height equal to those of the template, which the selected correlation surface belongs to. Finally, the target coordinates, (x, y), with respect to the origin of the frame are determined using Eqs. (2.18) and (2.19). These coordinates will be further adjusted by the best-match rectangle adjustment algorithm proposed in Section 3.3.8, in order to deal with the possible incorrect template initialization and the template drift. Furthermore, the highest peak value in the selected correlation surface, i.e. c_{max}, will work as the normalized confidence level of the object localization process in the later stages of the tracker.

3.3.7 Template Updating

The shape and orientation of the object being tracked may change during its motion in the video. Therefore, a constant template can not work for a long and good tracking session. It must be adapted with time according to the change in the appearance and orientation of the object in the video. This section describes some conventional template updating schemes as well as the proposed one. In all cases, let b_n be the best-match section in the current search window, and let t_n and t_{n+1} be the current and the updated templates, respectively. The c_{max} is the peak value in correlation surface, as previously defined. Finally, let τ_t be some threshold, such that $0 < \tau_t < 1$. Satisfactory results have been obtained by permanently setting $\tau_t = 0.84$ for every scenario.

3.3.7.1 Simple Template Updating Method

In this scheme, the template can be updated by just replacing the current template with the best-match region, if the correlation peak is greater than the threshold; otherwise the template is not updated. This approach is mathematically described as:

$$t_{n+1} = \begin{cases} b_n & \text{if } c_{\max} > \tau_t \\ t_n & \text{otherwise} \end{cases}. \qquad (3.1)$$

This approach assumes that the best-match provided by the correlation is always the true target. On the contrary, sometimes the nearby clutter can produce a higher correlation value than the actual object does. Thus, the template is corrupted by the clutter in the simple template updating method and the object quickly walks off it.

3.3.7.2 α-Tracker Template Updating Method

In order to resolve the limitation of the simple template updating method, some researchers use α-tracker template updating method [11, 31, 32, 85]. It is given as:

$$t_{n+1} = \begin{cases} t_n + \alpha(b_n - t_n) & \text{if } c_{\max} > \tau_t \\ t_n & \text{otherwise} \end{cases}. \quad (3.2)$$

A larger value of α (close to 1.0), will cause a greater change in the template than a smaller value. If $\alpha = 0$, the template will not be updated at all. In [31, 32], a small constant value for α (e.g. 0.02) is used, which reduces the effect of short-lived noise or neighboring object by smoothing the update of the template over time. However, if the tracked object is rapidly changing its shape, α should be large so as to avoid stagnation on the previous appearance of the object.

3.3.7.3 The Proposed Template Updating Method

In order to eliminate the problems of the conventional template updating schemes mentioned in the previous sections, a robust template updating scheme is proposed. It uses a low-pass IIR (Infinite Impulse Response) filter [33, 34] with *adaptive* coefficients, $\lambda c_{\max}$ and (1-$\lambda c_{\max}$):

$$t_{n+1} = \begin{cases} \lambda c_{\max} b_n + (1 - \lambda c_{\max}) t_n & \text{if } c_{\max} > \tau_t \\ t_n & \text{otherwise} \end{cases}, \quad (3.3)$$

The value of λ should be low in the range (0.0, 0.3], so that the b_n can have less weight as compared to that of t_n, and the short-term clutter and the noise can be eliminated from the template. Typically, if the frame rate is adequately high (e.g. 25 fps), a reasonable value of λ is 0.16. In fact, the updated template is a weighted-sum of the current *best-match* and the current *template* (and the weights are adaptively changing). The current template itself is *not* the previous best-match, but weighted-sum of the previous best-match and the previous template. Thus, the proposed approach uses the history of the template, and it does not quickly assign the best-match as the new template. The amount of change to be introduced in the updated

template is determined by the quality of the correlated object. A stronger match is a good candidate for being the next template, so it introduces a larger weight to the best-match, when the peak correlation value is large. When the camera is moving and tracking an object, the neighboring background pixels are continuously changing randomly. Therefore, these pixels will not become the dominant part of the template due to the low value of $\lambda c_{\max}$. On the contrary, the pixels belonging to the object do not change as rapidly, so their effect will become more and more dominant in the template with time. As a result, the template will contain only the object and not the neighboring clutter. Thus, the proposed template updating method also handles the short-lived neighboring clutter. This method also decreases, to some extent, the tendency of the object to drift away from the template. Nevertheless, the template-drift problem is also handled formally by the best-match rectangle adjustment algorithm presented in the next section.

3.3.8 Best-Match Rectangle (BMR) Adjustment

Regardless of the correlation metric used in the template matching process, there are two main concerns that should be addressed properly for precise and persistent correlation tracking. Firstly, the human operator is usually unable to initialize (or extract) a good template of the object of interest, while the object is moving and maneuvering in the video. As a result, the extracted template is usually larger or smaller than the object, or the object is significantly deviated from the center of the template. Secondly, the object tends to drift away from the center of the template slowly with time in a typical correlation tracking session, especially when the object being tracked is rotating in the video. The proposed template updating method discussed in Section 3.3.7 reduces the template-drift to some extent, but the technique does not completely eliminate the problem. The *incorrect template initialization* and

the *template-drift* severely deteriorate the performance of the correlation tracker in two ways. Firstly, they make the background pixels invade into the template, and the visual tracking algorithm starts assuming that it has to track the background clutter instead of the desired object, resulting in a total failure of the tracking session. Secondly, the object remains deviated from the center of the frames in the resulting video, even if the pan-tilt control algorithm itself is very efficient and precise.

These two problems are solved by introducing a *best-match rectangle (BMR) adjustment* algorithm, which is used after the BMR is obtained from the object localization process (Section 3.3.6) and the template is updated by Eq. (3.3). The algorithm analyzes the content of the template and resizes and/or relocates the BMR, so that it can have more of the object and less of the background inside it. As a result, the object remains always at the center of the template as well as the frame (if the camera is moved by the pan-tilt control algorithm to compensate the object motion). The BMR adjustment algorithm consists of two main stages: *template analysis* and *resizing / relocation of the BMR*.

3.3.8.1 Template Analysis

The template analysis stage is started with the splitting of the updated edge-enhanced template (obtained from Section 3.3.7) into nine non-overlapping equal regions, each of size $(K/3)\times(L/3)$, as shown in Figure 3.4. Then, the mean value of the pixels inside every region is computed. The mean value is denoted by μ_i, where i = 1, 2, 3, …, 9. Then, a vote from every non-central region (i.e. the region other than R_5) is obtained for whether the BMR should be same, expanded, or shrunk from the corresponding side. The flow chart of the voting function is illustrated in Figure 3.5. Each of the four side regions, i.e. R_2, R_4, R_6, and R_8, will provide a single vote to move the corresponding side of the BMR. However, each of the four corner regions will

provide three votes to move the corresponding horizontal side, vertical side, or both the sides of the BMR. Thus, if the *region under consideration* (from which the vote is to be obtained) is R_2, R_4, R_6, or R_8, its mean value is compared with the mean values of the *central region* (i.e. R_5) and the *opposite region* (i.e. R_8, R_6, R_4, or R_2, respectively), as shown in Figure 3.4. As a result, there are four votes: v_2, v_4, v_6, and v_8. However, if the *region under consideration* is in the corner (e.g. R_1, R_3, R_7, or R_9), its mean value is compared with the mean values of the regions in the corresponding horizontal, vertical, and diagonal directions to get the vote for moving the corresponding horizontal side, vertical side, or both sides, respectively. For instance, if the corner region under consideration is R_1, its mean value is compared with the mean values of R_2 and R_3 (i.e. the regions in the corresponding horizontal direction), then R_4 and R_7 (i.e. the regions in the corresponding vertical direction), and then R_5 and R_9 (i.e. the regions in the corresponding diagonal direction), as shown in Figure 3.4. As a result, there are twelve more votes: v_{1h}, v_{1v}, v_{1d}, v_{3h}, v_{3v}, v_{3d}, v_{7h}, v_{7v}, v_{7d}, v_{9h}, v_{9v}, and v_{9d}, where the subscripts *h*, *v,* and *d* represent *horizontal*, *vertical*, and

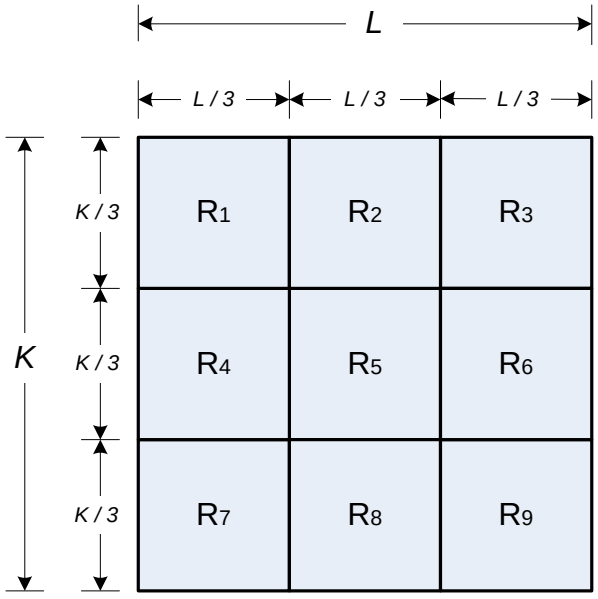

Figure 3.4 The rectangular template split into nine non-overlapping equal regions

diagonal, respectively. Thus, there are sixteen votes in total.

If the vote, v, in the voting function shown in the flow chart in Figure 3.5 is negative, the BMR will be shrunk from the corresponding side. If it is positive, the

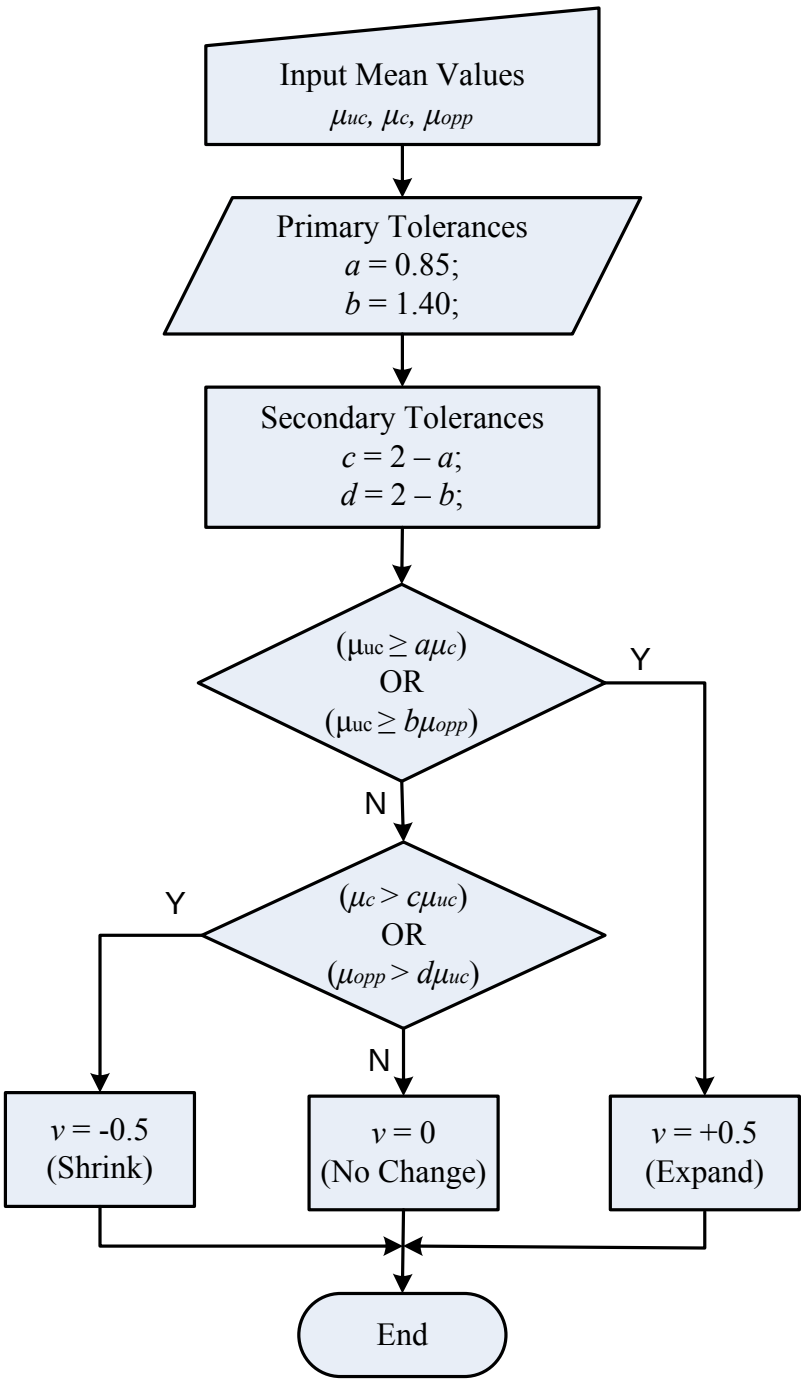

Figure 3.5 Flow chart of the voting function for obtaining the vote from a non-central region for expansion, shrinking, or no change of the best-match rectangle from the corresponding side. The μ_{uc}, μ_c, and μ_{opp} are the input parameters of the function and they are basically the mean values of the region under consideration, the central region, and the opposite region, respectively.

BMR will be expanded from the corresponding side. If it is zero, the BMR will remain same at the corresponding side. The magnitude of the vote defines the step size of the movement of the corresponding side of the BMR. It is set to 0.5 in order to have smooth resizing and relocation of the BMR. If the values of the primary tolerances (i.e. *a* and *b*) are increased, the BMR will be reluctant to resize/relocate. However, if their values are decreased, the BMR will expand and shrink freely. Satisfactory results have been obtained by setting their values as mentioned in the flow chart shown in Figure 3.5.

3.3.8.2 Resizing / Relocation of the BMR

Once all the sixteen votes are obtained in the template analysis stage, the changes to be introduced in the coordinates of the BMR are calculated. Since every vote from a corner region has its own importance in moving the corresponding sides of the BMR, the changes are computed by taking weighted sums of the votes, as:

$$\begin{aligned}
\Delta x_{TL} &= round(w_d v_{1d} + v_4 + w_d v_{7d} + w_s v_{1h} + w_s v_{7h}),\\
\Delta y_{TL} &= round(w_d v_{1d} + v_2 + w_d v_{3d} + w_s v_{1v} + w_s v_{3v}),\\
\Delta x_{BR} &= round(w_d v_{3d} + v_6 + w_d v_{9d} + w_s v_{3h} + w_s v_{9h}),\\
\Delta y_{BR} &= round(w_d v_{7d} + v_8 + w_d v_{9d} + w_s v_{7v} + w_s v_{9v}),
\end{aligned} \tag{3.4}$$

where the function *round*(.) simply rounds a number to its nearest integer, w_d is the weight applied on the votes obtained from the diagonal regions and w_s is the weight applied on the votes obtained from the horizontal or vertical regions. The values for these weights are set experimentally as: $w_d = 0.250$ and $w_s = 0.375$. It may be noted that $w_d < w_s$, because the distance between the centers of two diagonally connected regions is larger than that between the centers of two horizontally or vertically connected regions. Thus, the nearer the regions, the more weighted their votes. The Δx_{TL} and Δy_{TL} are the changes to be introduced in the *x* and *y* coordinates of the *top-*

left vertex of the BMR, respectively. Similarly, the Δx_{BR} and Δy_{BR} are the changes to be introduced in the x and y coordinates of the *bottom-right* vertex of the BMR, respectively. Finally, the coordinates of the adjusted BMR are determined as:

$$\begin{aligned}(x_{TL},\, y_{TL}) &= (x_{TL0} - \Delta x_{TL},\, y_{TL0} - \Delta y_{TL}) \\ (x_{BR},\, y_{BR}) &= (x_{BR0} + \Delta x_{BR},\, y_{BR0} + \Delta y_{BR})\end{aligned} \tag{3.5}$$

where (x_{TL0}, y_{TL0}) and (x_{TL}, y_{TL}) are the coordinates of the top-left vertices of the original and the adjusted BMRs, respectively. Similarly, (x_{BR0}, y_{BR0}) and (x_{BR}, y_{BR}) are the coordinates of the bottom-right vertices of the original and the adjusted BMRs, respectively. If the magnitude of the vote, v, in the voting function is set to 0.5 as suggested previously, the maximum change in the width and/or height of the BMR will be of two pixels per iteration, and it can be confirmed by putting the suggested values of the weights and all positive (or negative) votes in Eqs. (3.4) and (3.5).

It may be noted, that the correlation operation may provide false alarms, if the template is extremely small. On the contrary, the correlation operation can be computation intensive, if the template is extremely large. In order to address these situations, some limit on the new BMR size is applied. If the new coordinates are making the BMR smaller than $K_{min} \times L_{min}$ or larger than $K_{max} \times L_{max}$, the new BMR is not accepted in that particular iteration. However, if the new coordinates are only relocating (and not resizing) the BMR, the new BMR is accepted. In this research, the values of these limits are permanently set as: $K_{min} = L_{min} = 21$, $K_{max} = L_{max} = 41$.

The BMR adjustment algorithm analyzes the *updated edge-enhanced template*, but adjusts the *BMR*. One important question may arise at this point. What difference does it make to the template itself, which will be actually used in the next iteration of the tracking loop? The answer to this question is that we:

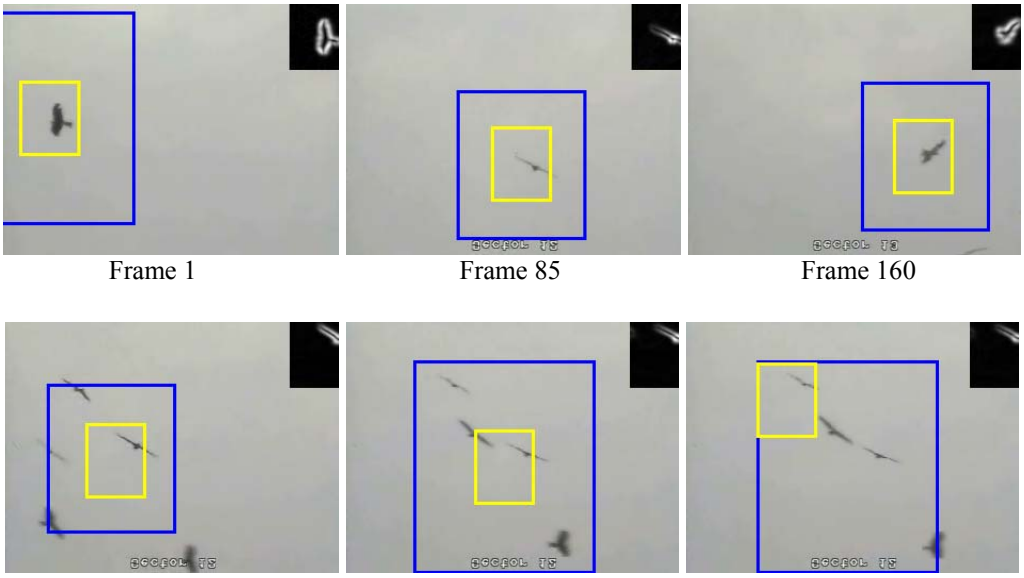

Figure 3.6 Tracking a maneuvering kite (the bird) in a test video, without using BMR adjustment algorithm. Yellow rectangle is the BMR and the blue rectangle is the dynamic search window. The current template is overlaid at the upper-right corner on each frame. The template is incorrectly initialized in such a way, that it is significantly larger than the object and the object is deviated from its center. It can be seen that the object is slowly going away from the center of the template with time. At 347th frame, the tracker has left the object of interest and started tracking another similar object, which was also inside the current search window.

- Replace the pixels of the search window at the rectangular section represented by the *original* BMR with the *updated template* pixels obtained in Section 3.3.7, and
- Extract a rectangular patch from the resulting search window using the coordinates of the *adjusted* BMR.

The patch will serve as an appropriately *updated* and *adjusted* template ready for use in the next iteration. Moreover, the target coordinates, which were obtained from the object localization process (discussed in Section 3.3.6), will have to be replaced by the center coordinates of the adjusted BMR in the frame.

Figure 3.6 shows, that a maneuvering kite (the bird) of interest is not tracked successfully in the test video, due to the incorrect template initialization, the template drift phenomenon, and the presence of other kites. However, Figure 3.7 illustrates that

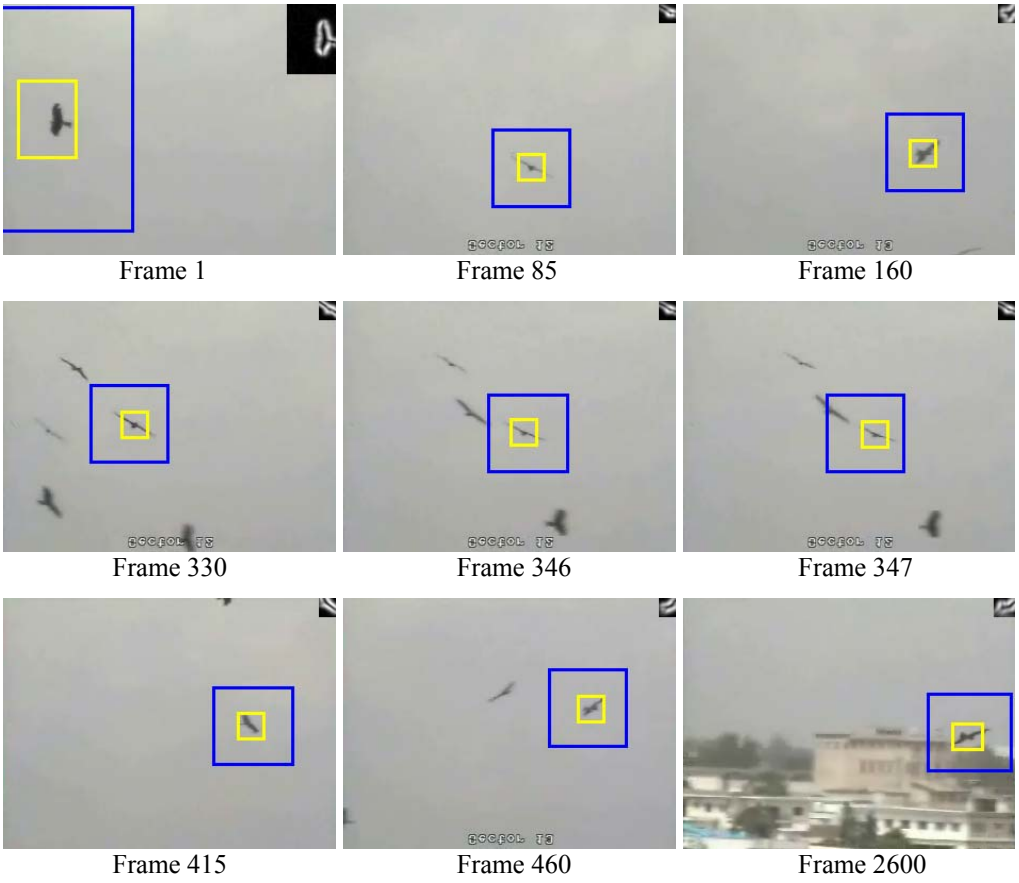

Figure 3.7 Tracking a maneuvering kite (the bird) in a test video, when the BMR adjustment is performed. The current template is overlaid at the upper-right corner on each frame. The template is initialized incorrectly in such a way, that it is significantly larger than the object and the object is deviated from its center. The BMR adjustment algorithm reduces the size of the template appropriately to tightly enclose the object in every frame. As a result, the object does not drift away from the center of the template with time. That is, the template drift problem is eliminated. The size of the dynamic search window is smaller as compared to the one in Figure 3.6, because the template size is now smaller than the initial template. At 347th frame, the tracker is not distracted by the other kites, because the template is now a good representative of the kite of interest and the appropriately sized search window does not contain the other kites inside it. The tracking is continued robustly and persistently till the last (i.e. 2600th) frame of the long test video.

the same object in the same test video is tracked successfully up to the last frame, even if the template is initialized incorrectly. This is because the BMR adjustment algorithm continuously adjusts the BMR, so that it can enclose the object of interest tightly. Due to the adjusted BMR, the template is reduced in size and contains more of the object and less of the background. Therefore, the dynamic search window is also appropriately small, which does not let the other objects invade inside it. As a result, the computational complexity is reduced, the tracking accuracy is increased, and the

tracker is not distracted by the other objects in the scene even if they are very similar to the object being tracked. Due to the visual tracking accuracy, the object will be exactly at the center of the frame and the moving camera will point precisely at the object if the pan-tilt control algorithm is controlling its motion, as discussed in Chapter 4.

The BMR adjustment algorithm can work with any correlation metric or/and gray-level images, as far as the template is first edge-enhanced before it is analyzed. For example, in [100], the technique has been used with NCC and gray-level images to have persistent and precise tracking results.

3.3.9 Occlusion Handling

A target is said to be (partially or completely) occluded when it is (partially or completely) hidden due to the appearance of another object between the camera and the target. Before handling the occlusion, the tracker has to sense when an occlusion has occurred. In order to sense the occurrence of an occlusion, a fact about the correlation process is exploited. That is, when the object being tracked is *suddenly* occluded by another object, the peak correlation value is dropped below the threshold (τ_t). This threshold is the same which is also used for updating the template in Eq. (3.3). When the correlation peak value is dropped, the proposed tracker goes to its occlusion handling mode, as described by the following steps:

1. Assume that the target coordinates provided by the correlation process are not correct and that the target is at the coordinates predicted by the Kalman filter in the previous iteration.
2. Update the Kalman filter in the current iteration with its own prediction made in the previous iteration.

3. Stop updating the template in order to prevent it from being distorted by the appearance of the occluding object.
4. Slightly reduce the threshold to be used in the next frame, iteratively, as:

$$\tau_{t,n+1} = \tau_{t,n} - 0.0005 \tag{3.6}$$

if $\tau_{t,n} \geq \tau_{t\_min}$, where τ_{t_min} is the minimum threshold that can be used safely without increasing the risk of having false alarms (it is set to 0.65 in this research). Furthermore, n is the current frame index. The threshold is iteratively decreased in order to allow the object to slightly change its appearance with time during its occlusion.

5. Gradually expand the dynamic search window for the next frame by iteratively increasing the value of the border parameter κ in Eq. (3.24), as:

$$\kappa_{n+1} = \kappa_n + 2 \tag{3.7}$$

This is done in order to compensate for the uncertainty in the speed and direction of the object during occlusion. This approach, effectively, enlarge the search window by 4 rows and 4 columns per iteration during the occlusion, because of the addition of 2 (i.e. the half of 4). If this value is increased, the search window will be expanded accordingly in larger steps.

6. If the correlation peak in the next iteration reaches above the current threshold value, assume that the object has come out of the occlusion, and that the coordinates provided by the correlation process are now correct. At this point, the values of τ_t and κ should be reset to their initial default values (i.e. 0.84 and 19 respectively) for normal correlation tracking.

3.3.10 Kalman Filter

The Kalman filter [7, 77] in the proposed tracker estimates (or predicts) the position of the target in the next frame. The predicted position is exploited to:

- Search for the object of interest in the next frame only around the predicted position (see Section 3.3.11), so that the probability of picking-up a similar object moving in a different direction can be minimized,
- Create a dynamic search window of optimal size (see Section 3.3.11.2), so that the tracker can track the object even in the presence of complex object motion and there can be less amount of background in the search window without losing the track of the object,
- Make the motors of PTU ready, one step ahead of time, to start moving the camera to follow the target without any delay (see Chapter 4).

3.3.10.1 Dynamic Model for the Motion of the Target

The dynamic model for the target motion normally used for Kalman filter in the literature of trackers is "constant velocity with random walk" [43], but in this research a 2-D "constant-acceleration with random walk [36]" model with six states [see Eqs. (3.8) - (3.15)] is used, because it provides better accuracy in case of slow as well as accelerating target. The target state equation and the observation equation, respectively, are given as [7, 77]:

$$\mathbf{X}_{n+1} = \mathbf{\Phi X}_n + \mathbf{U}_n, \tag{3.8}$$

$$\mathbf{Y}_n = \mathbf{M X}_n + \mathbf{V}_n, \tag{3.9}$$

where $\mathbf{X}_n$ is the proposed state vector containing six states (position, velocity, and acceleration in x and y direction), defined as:

$$\mathbf{X}_n = \begin{bmatrix} x_n & \dot{x}_n & \ddot{x}_n & y_n & \dot{y}_n & \ddot{y}_n \end{bmatrix}^T, \tag{3.10}$$

where the single dot and the double dot over a variable represent single derivative and double derivative with respect to time, respectively. The state transition matrix, $\mathbf{\Phi}$, is defined as in Eq. (3.11), where T is the sampling time (which is simply the inverse of the frame rate). It may be noted, that the x_n and y_n are expressed in terms of 2nd order approximation of their Taylor expansions, respectively [36].

$$\mathbf{\Phi} = \begin{bmatrix} 1 & T & \frac{T^2}{2} & 0 & 0 & 0 \\ 0 & 1 & T & 0 & 0 & 0 \\ 0 & 0 & 1 & 0 & 0 & 0 \\ 0 & 0 & 0 & 1 & T & \frac{T^2}{2} \\ 0 & 0 & 0 & 0 & 1 & T \\ 0 & 0 & 0 & 0 & 0 & 1 \end{bmatrix}. \tag{3.11}$$

$\mathbf{U}_n$ in Eq. (3.8) is the system noise vector, given by:

$$\mathbf{U}_n = \begin{bmatrix} 0 & 0 & u_{xn} & 0 & 0 & u_{yn} \end{bmatrix}^T, \tag{3.12}$$

where u_{xn} and u_{yn} are the assumed uncorrelated zero-mean Gaussian noise elements with variances σ_{ux}^2 and σ_{uy}^2, respectively. They account for the small uncertainty in the acceleration of the object. For simplicity, the values of these variances can be set to unity. $\mathbf{Y}_n$ in Eq. (3.9) is the *measurement vector* given by:

$$\mathbf{Y}_n = \begin{bmatrix} x_n & y_n \end{bmatrix}^T, \tag{3.13}$$

where x_n and y_n are the noisy target-coordinates. They are obtained from the correlation based object localization algorithm at time step n. **M** in Eq. (3.9) is the *observation matrix* given by:

$$\mathbf{M} = \begin{bmatrix} 1 & 0 & 0 & 0 & 0 & 0 \\ 0 & 0 & 0 & 1 & 0 & 0 \end{bmatrix}, \tag{3.14}$$

and $\mathbf{V}_n$ in Eq. (3.9) is the *observation noise vector* given by:

$$\mathbf{V}_n = \begin{bmatrix} v_{xn} & v_{yn} \end{bmatrix}^T, \tag{3.15}$$

where v_{xn} and v_{yn} are the assumed uncorrelated zero-mean Gaussian noise elements with variances σ_{vx}^2 and σ_{vy}^2, respectively. If the variances are set to high values, the Kalman filter will give the predicted coordinates high importance as compared to the measurement coordinates, during its updating (or correcting) phase after the arrival of the new measurement [37]. For simplicity, the values of these variances can be set to unity.

3.3.10.2 Kalman Filter Updating

Once the Kalman filter receives the new measurement (i.e. the pixel coordinates of the target), it is updated to correct its last prediction error if any. The filter is updated as [36, 37, 38]:

$$\mathbf{X}_{n|n}^* = \mathbf{X}_{n|n-1}^* + \mathbf{K}_n \left(\mathbf{Y}_n - \mathbf{M}\mathbf{X}_{n|n-1}^* \right), \tag{3.16}$$

where the subscript "$n|n$-1" means the prediction made in the previous iteration, and "$n|n$" means the updated (or corrected) versions of the previous prediction. $\mathbf{K}_n$ in Eq. (3.16) is the *Kalman gain matrix* defined as [36, 37, 38]:

$$\mathbf{K}_n = \mathbf{S}_{n|n-1}^* \mathbf{M}^T \left[\mathbf{R}_n + \mathbf{M}\mathbf{S}_{n|n-1}^* \mathbf{M}^T \right]^{-1}, \tag{3.17}$$

where $\mathbf{S}_{n|n-1}^*$ is the *predictor error covariance* computed in the previous iteration as:

$$\mathbf{S}^{*}_{n|n-1} = COV(\mathbf{X}^{*}_{n|n-1}) = \mathbf{\Phi}\mathbf{S}^{*}_{n-1|n-1}\mathbf{\Phi}^{T} + \mathbf{Q}_{n}, \tag{3.18}$$

where $\mathbf{S}^{*}_{n-1|n-1}$ is the *covariance of the updated estimate* computed in the previous iteration as:

$$\mathbf{S}^{*}_{n-1|n-1} = COV(\mathbf{X}^{*}_{n-1|n-1}) = \left[\mathbf{I} - \mathbf{K}_{n-1}\mathbf{M}\right]\mathbf{S}^{*}_{n-1|n-2}. \tag{3.19}$$

The $\mathbf{Q}_n$ in Eq. (3.18) is the *noise covariance matrix* of the dynamic model. It is given as:

$$\mathbf{Q}_{n} = COV(\mathbf{U}_{n}) = E[\mathbf{U}_{n}\mathbf{U}_{n}^{T}], \tag{3.20}$$

and $\mathbf{R}_n$ in Eq. (3.17) is the *observation noise covariance* defined as:

$$\mathbf{R}_{n} = COV(\mathbf{V}_{n}) = E[\mathbf{V}_{n}\mathbf{V}_{n}^{T}], \tag{3.21}$$

where $E[.]$ is the "expected value of" operator [36].

3.3.10.3 Prediction by Kalman Filter

The *predicted estimate* of the state vector is given by the *state transition* or *prediction* equation given as under [36, 37, 38]:

$$\mathbf{X}^{*}_{n+1|n} = \mathbf{\Phi}\mathbf{X}^{*}_{n|n}, \tag{3.22}$$

where the superscript (*) indicates, that the state vector has been *estimated* by the Kalman filter, and is not the *actual* measurement obtained from the object localization algorithm. $\mathbf{X}^{*}_{n|n}$ is the updated (or corrected) estimate of the state vector coming from Eq. (3.16). Finally, the position of the target in the next frame is predicted as:

$$\begin{bmatrix} x^*_{n+1|n} \\ y^*_{n+1|n} \end{bmatrix} = \mathbf{M}\mathbf{X}^*_{n+1|n}. \tag{3.23}$$

The predicted target position will be used for generating the dynamic search window for the next iteration (Section 3.3.11), occlusion handling (Section 3.3.9) in the next iteration, and generating the pan-tilt control signals in the current iteration (Chapter 4) for efficient and accurate target tracking with moving camera.

3.3.11 Search Window Updating

The target is usually looked for in a small search window instead of the whole frame. This is done in order to save CPU time and get rid of the false alarms due to the clutter possibly present in the background. However, the search window should not be too small, because there will be a risk of losing the target if it is moving fast [11].

3.3.11.1 Traditional Fixed-Size Search Window

Conventionally, the size of the search window is set to be *constant* throughout the tracking session and its center is updated with the center of the last best-match rectangle (BMR) [39] or the predicted position [11]. These approaches have some drawbacks: (1) If the search window size is fixed and small, and the target is moving and maneuvering very fast, it may go out of the search window. (2) If the search window size is fixed and large, and the target is moving and maneuvering very slow, the redundant background in the search window may contain some clutter. As a result, the clutter may create false alarms and the large size of the search window will make the correlation process slow.

3.3.11.2 Proposed Dynamic Search Window

In order to eliminate the problems of the fixed-size search window highlighted above, the *location* and the *size* of the search window are proposed to be *dynamically*

updated using the prediction and the prediction-error of the Kalman filter explained as follows.

Assuming that K (template-height) and L (template-width) are odd integers, the top-left and the bottom-right co-ordinates, i.e. (x_{tl}, y_{tl}) and (x_{br}, y_{br}) respectively, of the search window in the frame are determined by Eq. (3.24), where $(x^*_{n+1|n}, y^*_{n+1|n})$ are the future target-coordinates estimated by Kalman filter.

$$\begin{aligned} x_{tl} &= x^*_{n+1|n} - \left(\frac{L-1}{2} + \kappa + a_{tx} \left| \varepsilon_x \right| \right), \\ y_{tl} &= y^*_{n+1|n} - \left(\frac{K-1}{2} + \kappa + a_{ty} \left| \varepsilon_y \right| \right), \\ x_{br} &= x^*_{n+1|n} + \left(\frac{L-1}{2} + \kappa + a_{bx} \left| \varepsilon_x \right| \right), \\ y_{br} &= y^*_{n+1|n} + \left(\frac{K-1}{2} + \kappa + a_{by} \left| \varepsilon_y \right| \right), \end{aligned} \tag{3.24}$$

The first three terms in case of every coordinate in Eq. (3.24) make a *minimum-size search window* of size (K+2κ) × (L+2κ), where κ is the minimum width of the border around K×L area centered at the predicted position. The value of κ is experimentally set to 19. Furthermore, ε_x and ε_y in Eq. (3.24) are the *prediction errors*, defined as:

$$\begin{aligned} \varepsilon_x &= x_n - x^*_{n|n-1}, \\ \varepsilon_y &= y_n - y^*_{n|n-1}, \end{aligned} \tag{3.25}$$

where $(x^*_{n|n-1}, y^*_{n|n-1})$ is the target position predicted by Kalman filter in the *previous* iteration. Furthermore, (x_n, y_n) is the target position provided by the correlation process in the *current* iteration. It may be noted, that in the first iteration these coordinates are initialized with the actual target coordinates, from where the template was extracted by the user.

The a_{tx}, a_{ty}, a_{bx}, and a_{by} parameters in Eq. (3.24) are the scaling factors, which compensate for the possible prediction errors in case of a sudden maneuvering of the object. If any of the scaling factors is positive, the *minimum-size search-window* will be expanded further in the direction of the object motion proportional to the corresponding prediction error. If it is negative, the *minimum-size search-window* will be contracted from opposite direction of the object motion proportional to the corresponding prediction error. The scaling factors are given as:

$$\left(a_{tx}, a_{bx}\right) = \begin{cases} (a_1, a_2) & \text{if } \varepsilon_x \geq 0 \\ (a_2, a_1) & \text{otherwise} \end{cases} \tag{3.26}$$

$$\left(a_{ty}, a_{by}\right) = \begin{cases} (a_1, a_2) & \text{if } \varepsilon_y \geq 0 \\ (a_2, a_1) & \text{otherwise} \end{cases} \tag{3.27}$$

where a_1 = -0.25 and a_2 = +1.25 in this research to contract/expand the search window from the the corresponding opposite sides by 25% of the error. If their magnitude is increased, the contraction/expansion will occur in larger steps.

For example, if the prediction error in x-axis is ε_x = +8, the actual target position (determined by the correlation process) is to the right of the predicted position, thus the minimum-size search window will be contracted by 2 pixels from left (using a_{tx} = -0.25), and expanded towards right side by 10 pixels (using a_{bx} = 1.25). Thus, the search window is *dynamically* created in every frame according to the nature of the motion of the maneuvering object. If the object is moving smoothly, there will be no prediction error, so the search window will be of minimum size. If the object is moving with abrupt maneuvering, the search window will be expanded towards the object motion and contracted from the opposite side. The resulting search window is large enough to get the target always inside the window, and small enough to reduce the background clutter and the computational complexity.

Figure 3.8 shows some frames from a short test video *seq_fast.avi* [55], in which a person is moving his head left and right very fast. The frames in the upper row is the result of a fixed-size search window of size $(60 + K) \times (60 + L)$ pixels centered at the predicted position. It can be seen in 21st frame that more than half of the object has got out of the search window (i.e. blue rectangle) and the tracking is lost, when the head is moved suddenly towards right. On the contrary, if the proposed dynamic search window is used, it is dynamically resized to compensate for the prediction error and the object is always inside it, as shown in the frames in the lower row in Figure 3.8. In both cases, if the search window happens to go out of the frame, it is cropped from the corresponding side. It is shown in Figure 6 in [51] that the mean shift [43, 48] and the condensation [51, 52, 53, 54] trackers could not track the fast moving face in this image sequence. However, the proposed tracker is able to track it without any difficulty as demonstrated. The tracking algorithm proposed in [51] exploits a particle filter using an appearance model based on Spatial-color Mixture of Gaussians (SMOG). Its results are comparative to those of the proposed tracker, but it

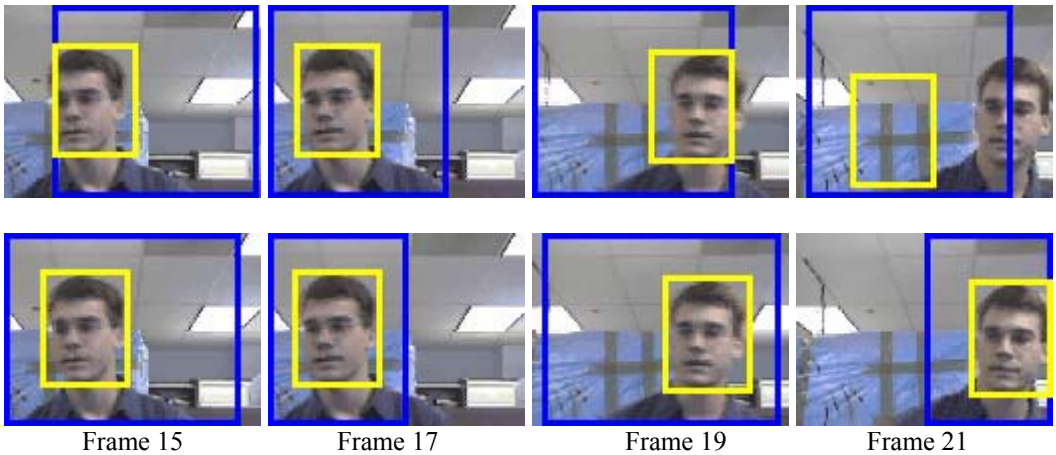

Figure 3.8 Frames from *seq_fast.avi* [55] showing the benefit of the dynamic search window as compared to the fixed-size search window, when the object is moving to and fro very fast. Upper row: When a fixed-size search window is used, the fast to and fro motion causes the object to get out of the search window; Lower row: The object is always inside the search window, when the proposed dynamic search window is used. Note: Search window is represented by a blue rectangle and the template by a yellow rectangle.

is not a real-time tracker.

3.4 Experimental Results

The proposed visual tracking algorithm has been tested on numerous real-world image sequences, but due to space constraint only some of them are presented for evaluation.

Figure 3.9 shows how the proposed tracker persistently tracks a person in the presence of other persons in the test video *ShopAssistant2cor.mpg* from CAVIAR dataset [40], until the person goes out of the scene. In Frame 200, it can be seen that the target person is partially occluded by another person; even then the tracking is continued.

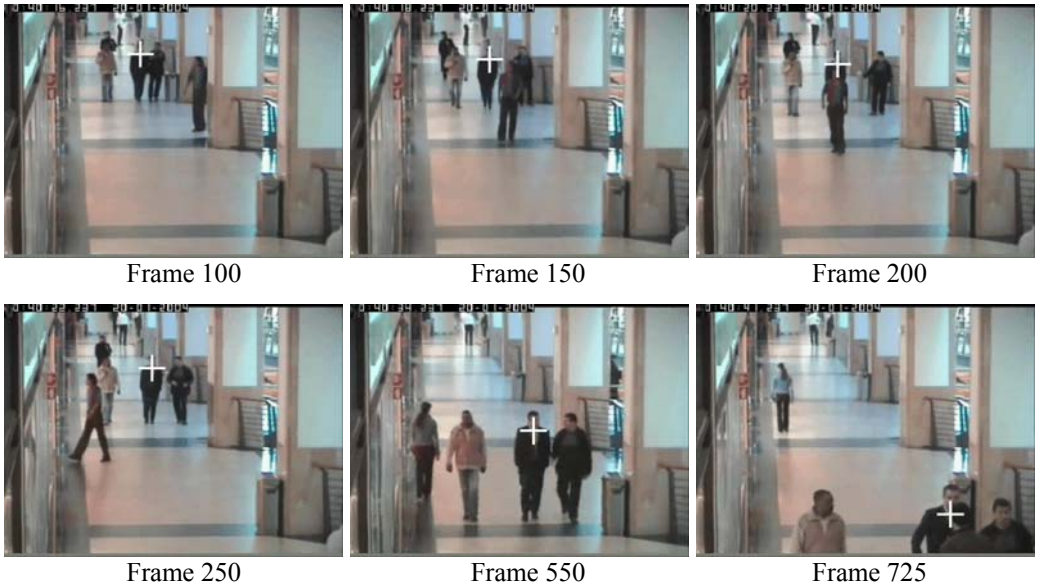

Figure 3.9 Some frames from *ShopAssistant2cor.mpg* video clip from CAVIAR dataset [40], illustrating the robustness of the proposed visual tracking algorithm even in the presence of multiple similar objects, uneven illumination, clutter, object scaling, and occlusion.

Figure 3.10 depicts the robust tracking of a car moving along the road in a low-contrast, noisy and shaky video sequence recorded from an unmanned aerial vehicle (UAV). The whole scene (including the car) is rotating and translating simultaneously due to the motion of the UAV in 6 degree-of-freedom. Furthermore, in Frame 375, there is a glare effect (uneven illumination). Never-the-less, the proposed algorithm tracks the car persistently. Figure 3.11 illustrates some frames from the sequence *seq_fast.avi* obtained from [55]. Here, a person moves his face right and left very fast (with slight rotation). The same frames are shown in Figure 6 in [51] and it is reported that the *mean shift* [43, 48] and the *condensation* [51, 52, 53, 54] trackers could not track the fast moving face in this sequence. However, the proposed tracker is able to track it without any difficulty as shown in Figure 3.11. The tracking algorithm proposed in [51] exploits a particle filter using an appearance-model based on spatial-color Mixture of Gaussians (SMOG). Its results are comparative to those of the proposed tracker, but it is not a real-time tracker.

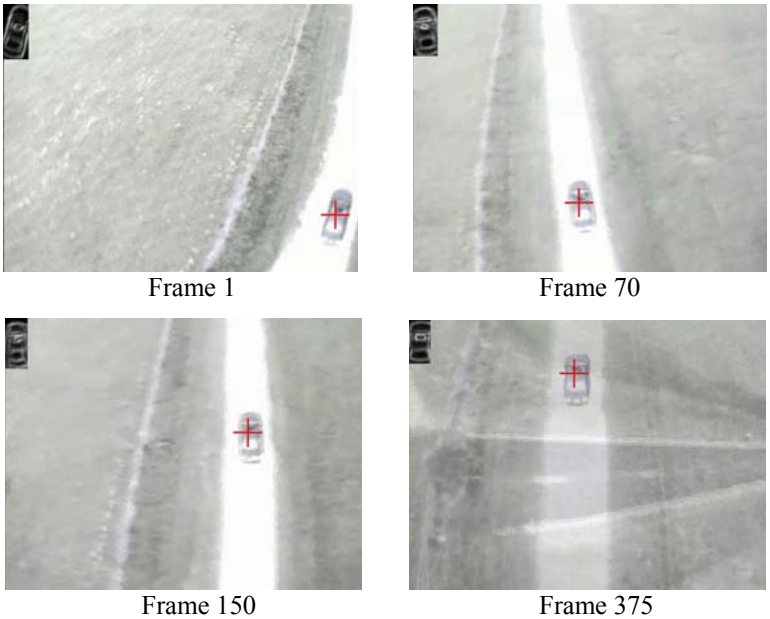

Figure 3.10 Some frames from a shaky video sequence recorded from an unmanned aerial vehicle (UAV) showing a small car being tracked perfectly by the proposed algorithm in the presence of blur, glare, noise and UAV motion in 6 degree-of-freedom. The current template is shown at the top left corner of every frame.

Figure 3.11 Some frames from *seq_fast.avi* sequence [55], in which the proposed algorithm tracks the face even during its fast left and right motion. However, the mean-shift and condensation trackers could not track the fast-moving face (see Figure 6 in [51]).

Figure 3.12 Some frames from *seq_mb.avi* sequence [55]. The proposed algorithm tracks the face of the girl even during occlusion. However, the mean-shift and condensation trackers could not robustly survive the occlusion in this sequence (see Figure 7 in [51]).

Figure 3.12 shows some frames from the sequence *seq_mb.avi* obtained from [55], in which the face of a girl is being occluded slowly with that of another person. In Figure 7 in [51], it is shown that the *mean shift* tracker [43, 48] and the *condensation* [52, 53, 54] trackers could not robustly track the face of the girl during and after this occlusion. However, the tracker presented in [51] could track it robustly. The proposed tracker has also successfully survived the occlusion with the results comparative to those of the tracker presented in [51], with the additional benefit of speed. The edge-enhanced template is shown at the top-right corner of each frame, and it can be observed how smoothly and robustly it is being updated without introducing significant effects due to the occluding face. Interestingly, during this occlusion, the correlation peak value did not drop below the threshold, and the formal occlusion handling method was not invoked, that is why the template is being updated smoothly during the occlusion. This kind of phenomenon occurs, when the object of interest is being occluded *gradually*.


Frame 295

Frame 330


Frame 365


Frame 395

Figure 3.13 Some frames from *PetsD2CeT2.avi* in the PETS dataset [83] showing a car being tracked by the proposed visual tracking algorithm in the presence of background clutter and variation in the scale as well as shape of the car.

Figure 3.13 depicts some frames from *PetsD2CeT2.avi* in the PETS dataset [83] showing a car being successfully tracked by the proposed visual tracking algorithm in the presence of background clutter and variation in the scale as well as the shape of the car.

Figure 3.14 illustrates some frames from a long and challenging video sequence *seq45-3p-1111_cam2.avi* (containing more than 1000 frames) in AV16.3 dataset [84]. In this image sequence, the face of a person with white shirt is being tracked persistently even in the presence of clutter and intermittent occlusions by the faces of the other two persons.

Figure 3.14 The proposed visual tracking algorithm is handling occlusion and clutter while tracking a person's face in a long video sequence *seq45-3p-1111_cam2.avi* in AV 16.3 v6 dataset [84]. The red rectangle indicates there is no occlusion and the algorithm is working in its normal tracking mode. When the algorithm detects and handles the occlusion, the rectangle color is changed to pink for demonstration.

3.5 Comparison with Traditional Correlation Tracker

In this section, the proposed correlation tracker (PCT) is compared with a traditional correlation tracker (TCT). The TCT uses normalized correlation coefficient (NCC) for object localization in original gray-level frames, α-tracker template updating scheme, and a search window of size $3K \times 3L$ centered at the previous target position. In both the trackers, the initial template of size 19×25 is selected from the same position in the initial frame, and the threshold for the correlation peak τ_t is set to 0.84. The trackers are evaluated on two challenging image sequences S_1 and S_2. The sequence S_1, containing 300 frames, shows a flying helicopter. During the recording of this

video, the handy-cam was continuously and randomly moved very fast to create random and fast motion of the helicopter in the video frames. Since the zoom level of the camera was high at the time of recording, the object was suddenly faded for a short time period as usual. The S_2 sequence contains 390 frames, in which an F-16 aircraft is taking-off, during which its size is varying, the background is cluttered with trees and small buildings, and there is an abrupt change in the background when the airplane is flying above the trees and buildings [35]. In order to evaluate the tracking accuracy of the algorithms, the ground truth containing true target-coordinates was generated manually for every frame in both the sequences.

Figure 3.15 is the result of TCT for S_1 sequence. The updated template is overlaid at the upper-left corner in every frame. The frame index, correlation value, and the (x, y) coordinates of the target location are also shown at the top of every frame. It can be observed that the white target sign slowly keeps drifting away from the helicopter and the track is lost when the helicopter is suddenly faded in Frame 273. It may be noted that the helicopter is almost invisible during the fading. The resulting trajectory of the helicopter is illustrated in Figure 3.16, in which the template-drift and the track-loss are observable starting from Frame 273.

Figures 3.17 and 3.18 show the robustness of the PCT that keeps a very good track of the target in the same video. It can be observed, that there is no template-drift or track-loss even during the severe and sudden fading of the object in the presence of fast and random object-motion in the low contrast imagery.

Figure 3.19 shows some frames from the image sequence S_2, when TCT is tested on it. It can be seen that the target sign is exactly at the middle of the airplane in Frame 1, but it slowly drifts backward in the subsequent frames. Furthermore, the track is lost in Frame 93, because the white roof of the building appears suddenly

above the airplane in the image and this white portion is not included in the current template. The complete trajectory of the airplane provided by TCT is compared with

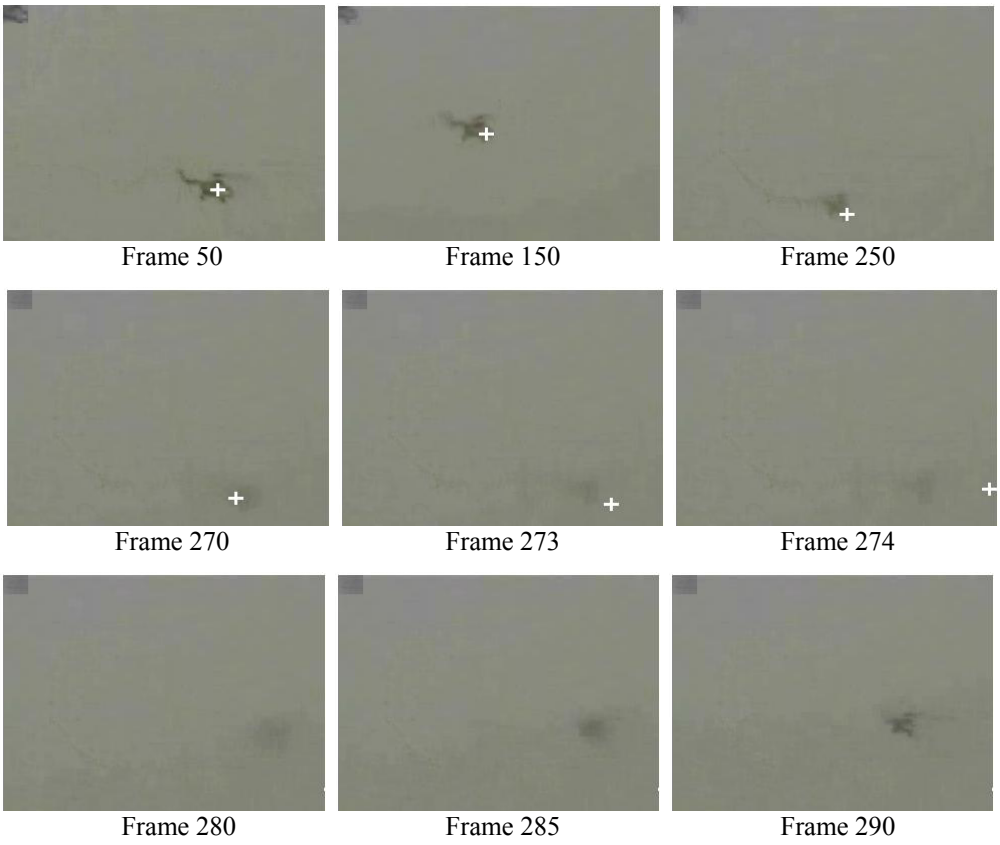

Figure 3.15 Result of TCT (Traditional Correlation Tracker) for S_1 image sequence, showing the template drift problem starting from Frame 150 and its failure starting from Frame 273 during object fading.

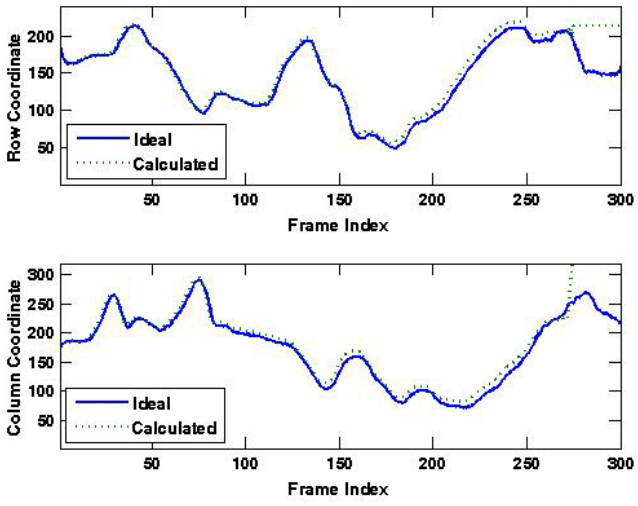

Figure 3.16 Target trajectory (row and column coordinates) produced by TCT for S_1 sequence showing the failure from Frame 273 through the last frame of the image sequence.

the true trajectory in Figure 3.20, which illustrates the failure of the algorithm starting from Frame 93. However, Figures 3.21 and 3.22 show the robustness of the PCT that

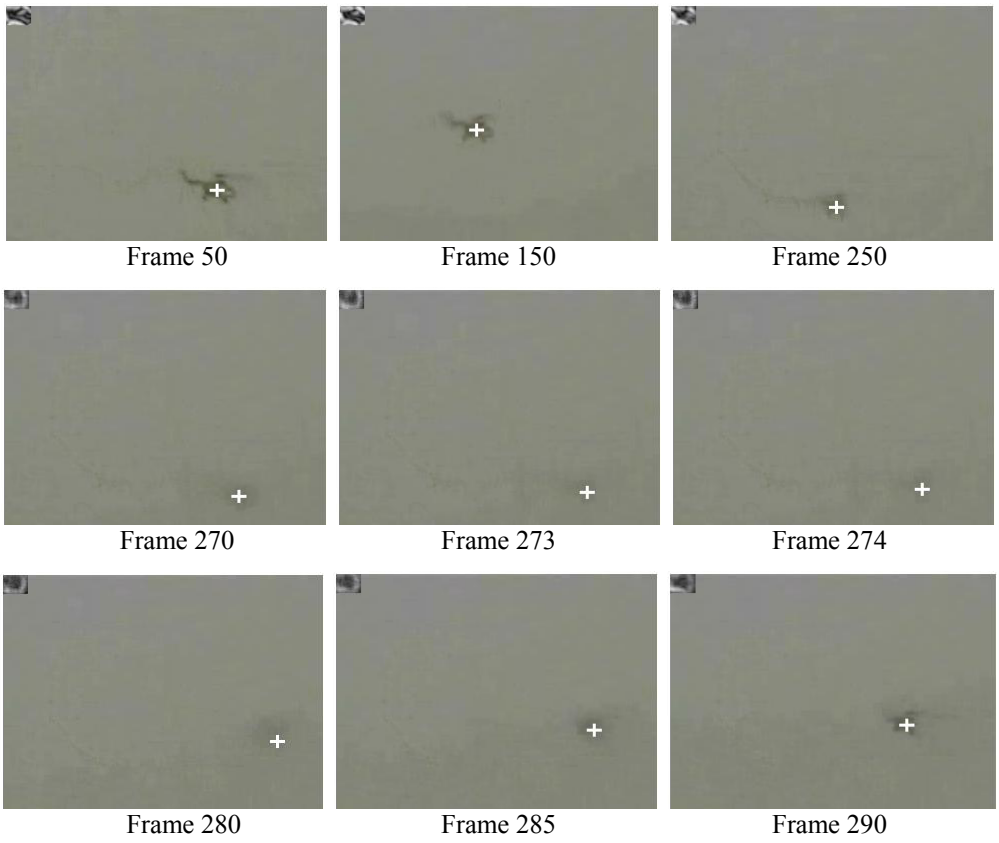

Figure 3.17 Result of PCT (Proposed Correlation Tracker) for S_1 image sequence. The proposed algorithm successfully tracks the helicopter in all the frames even during the severe object fading in very low-contrast video without any template-drift problem.

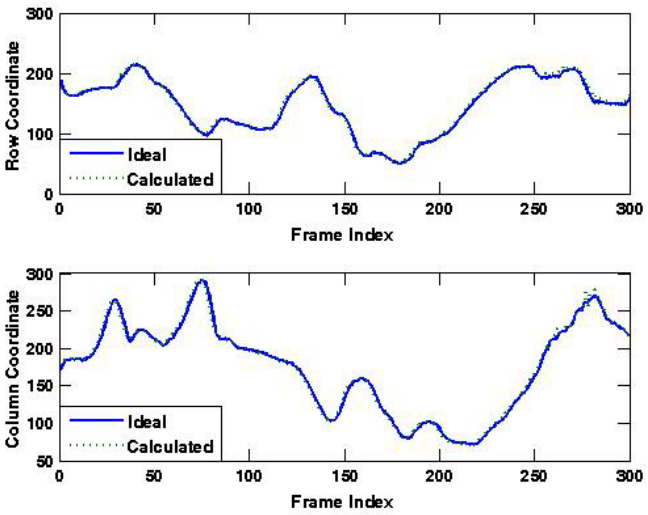

Figure 3.18 Target trajectory (row and column coordinates) for S_1 sequence produced by our A_2 algorithm. Note that the computed trajectory is perfectly matching the ground truth trajectory for almost all the frames.

keeps a good track of the airplane with negligible template drift even during the sudden appearance of the white roof of the building, the surrounding clutter, drastic change in the intensity of the background, and varying scale.

In order to evaluate the accuracy of both the algorithms for both the image sequences, a post regression analysis [24] is carried out that provides *R*-value (the

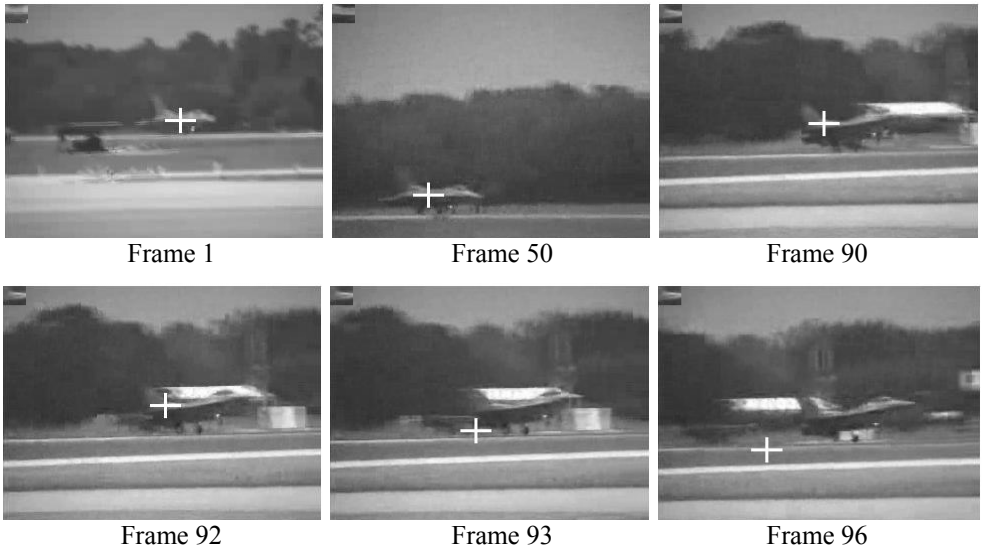

Figure 3.19 Result of TCT for S_2 image sequence. Note that the template-drift problem starts from Frame 90 and the failure starts from Frame 93 due to background clutter.

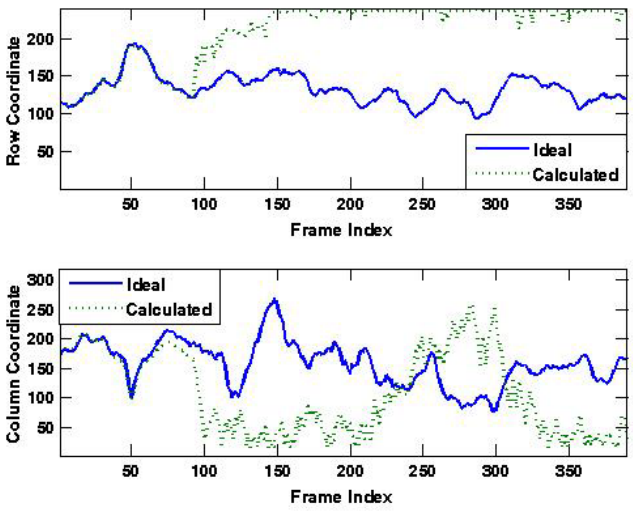

Figure 3.20 Target trajectory (row and column coordinates) produced by TCT for S_2 sequence, showing its failure starting from Frame 93.

correlation coefficient between the true and the calculated coordinates), and the best-

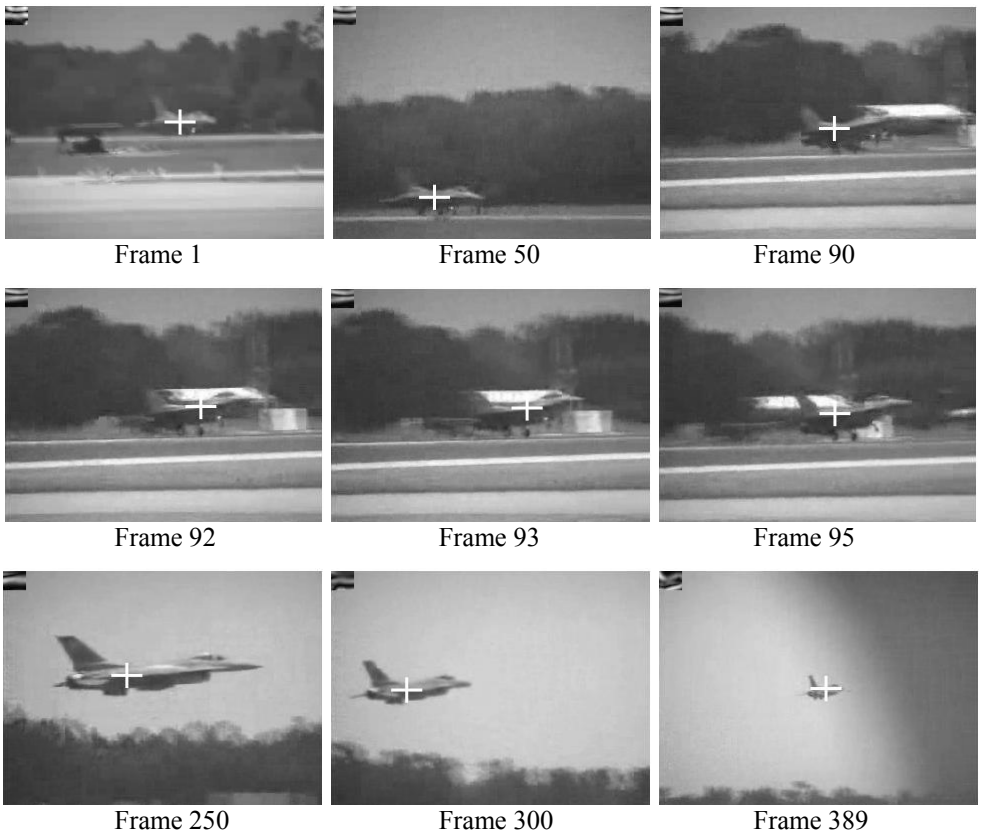

Figure 3.21 Result of PCT for S_2 image sequence, showing how persistently it tracks the airplane up to the last frame, even in the presence of scale change, the high background clutter and the low contrast between the object and the background in the initial part of the video, and the drastic change in the background intensity level in the later part of the video as compared to the first part.

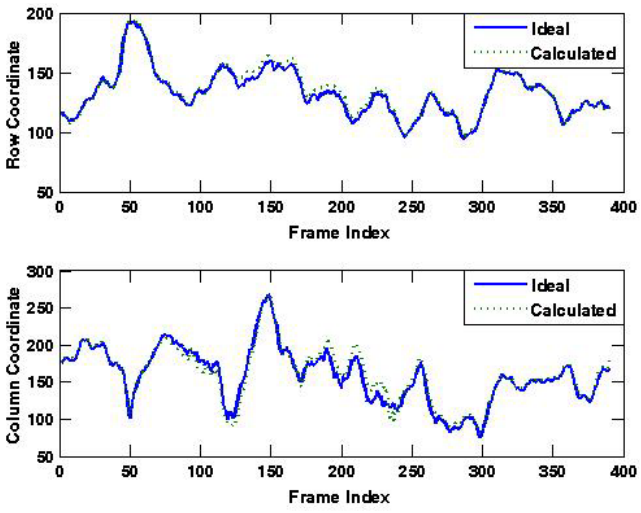

Figure 3.22 Target trajectory provided by PCT for S_2 sequence. It accurately follows the ground truth trajectory in almost all the frames.

Table 3.1 Post-regression analysis for comparing accuracy of TCT and PCT

Tracker	S_1 Sequence						S_2 Sequence					
	x			*y*			*x*			*y*		
	***R* (%)**	***m***	***C***	***R* (%)**	***m***	***C***	***R* (%)**	***m***	***C***	***R* (%)**	***m***	***C***
TCT	94.8	1	-1.3	94.5	1	7.6	34.6	0.6	-0.8	-0.16	-0.4	258
PCT	99.8	1	-0.2	99.7	1	0.4	97.4	0.95	8.9	99.3	1	0.4

fit linear equation between them consisting of a slope (m) and intercept (C). If the trajectory provided by the tracker and the ground truth trajectory are exactly similar, then R = 100%, m = 1.0, and C = 0. The results of the analysis are summarized in Table 3.1, which shows that PCT outperforms TCT in tracking accuracy for both the test sequences.

One might think at this point that the TCT might have performed better than PCT, if the images were edge-enhanced for both the trackers. In order to address the query, another set of experiments were performed where TCT was also using the edge-enhanced versions of the template as well as the search window for the S_1 and S_2 image sequences. It was found out that the edge-enhanced TCT did not show any significant improvement over the original TCT. That is, it failed at the same instant in the videos at which the original TCT did.

3.6 Chapter Summary

A visual tracking algorithm needs to address various practical problems, while it is tracking an object of interest in complex situations. The problems that cause those situations are loss of information, noise in images, background clutter, complex object motion, object fading, obscuration, partial and full occlusions, real-time processing requirements, variation in the shape and the scale of the object, and uneven brightness in the scene. Additionally, there is a severe problem of *template-drift* if the tracking is

performed using a simple correlation tracker. A correlation tracking framework has been proposed that addresses almost all of these problems very efficiently. Various experimental results have been presented to demonstrate the robustness and performance of the proposed tracker. The proposed tracker has also been compared with the mean-shift and the condensation trackers for some real-world publicly available test sequences and it has been shown that the proposed tracker outperforms them in robustness to the occlusion and the fast to-and-fro motion of the object. A comparison of the proposed correlation tracker (PCT) has also been performed with a traditional correlation tracker (TCT). The results of the post-regression analysis show that the proposed tracker is more robust and accurate than TCT. The next two chapters discuss the design, implementation, and analysis of the machine vision systems in which the proposed tracker is deployed.

4

Active Camera Tracking System

4.1 Chapter Overview

This chapter discusses the design, implementation, and analysis of an active camera tracking system that exploits the proposed visual tracking framework as an integrated module. Various experimental results, that validate the robust and accurate performance of the system, are also shown at the end of the chapter.

4.2 Problem Description

An active camera tracking system tracks an object of interest automatically with a pan-tilt-zoom (PTZ) video camera. The system, in its simplest form, is illustrated using a block diagram shown in Figure 4.1. It consists of a video camera, a visual tracking algorithm, a pan-tilt control algorithm, and a pan-tilt unit (PTU). Every frame acquired from the video camera is analyzed by the *visual tracking algorithm*, which localizes the object of interest inside the image in pixel-coordinates. The coordinates are then sent to a *pan-tilt control algorithm*, which generates the pan-tilt motion control signals to rotate the PTU according to the motion of the object in the scene. Since the camera is securely attached to the PTU, it also rotates in synchronization

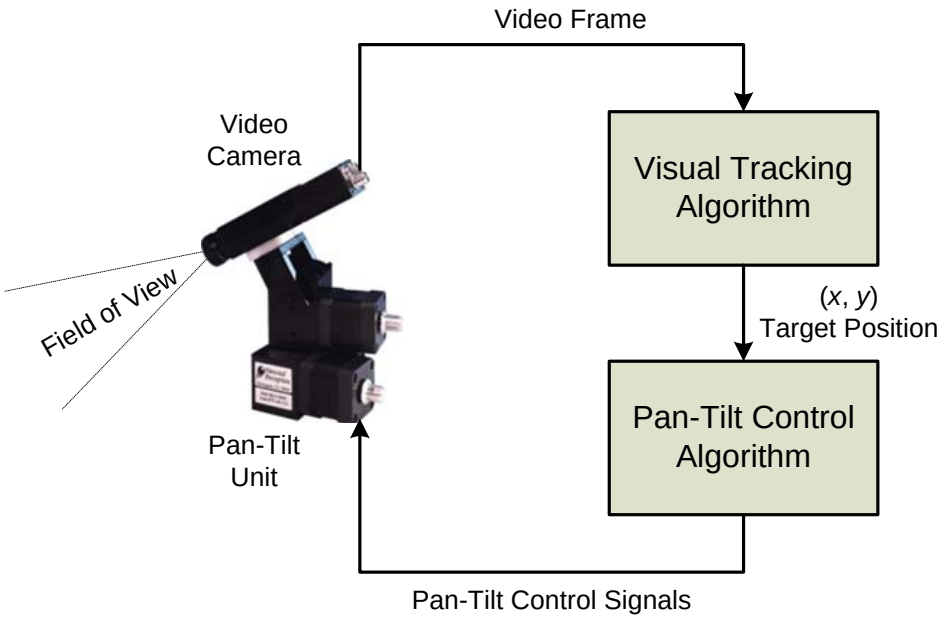

Figure 4.1 Simplified block diagram of an active camera tracking system

with the PTU. Thus, the tracked object is always projected at the center of the video frames regardless of the nature of the motion of the object.

Since the visual tracking algorithm has been already discussed in Chapter 3, only the pan-tilt control algorithm is designed and analyzed in the following section.

4.3 Pan-Tilt Control Algorithm

Most of the time, the algorithm used to control a plant or system is the classic proportional-integral-derivative (PID) controller [56]. However, its design requires a mathematical model of the plant or system. Besides, it necessitates a sensitive and rigorous tuning of its proportional, differential and integral gain parameters. The tuning of the three parameters is very time consuming, if they are to be optimized for use with all the zoom levels of the camera in a tracking application. An alternative approach is to use a fuzzy controller [10, 59, 60, 61] that does not require the system model, but choosing a set of right membership functions and fuzzy rules calibrated for every zoom-level of the camera is practically very cumbersome. Another alternative is

Figure 4.2 Demonstration of the Car-Following Control (CFC) law

to implement a neural network controller [25, 62], but it is heavily dependent on the *quality* and the *variety* of the *examples* in the training dataset, which can accurately represent the complete behavior of the controller in *all* possible scenarios, including the varying zoom-levels of the camera. Furthermore, the traditional control algorithms, e.g. the one used in [14], are generally implemented based on the difference between the center (i.e. reference) position and the current target *position* in the image. They do not account for the target *velocity*. As a result, there will be oscillations (if the object is moving slow), a lag (if it is moving with a mediocre speed), and loss of the object from the frame (if it is moving faster than the maximum pan-tilt velocity *generated* by the *control algorithm*). In order to address the limitations of the traditional control algorithms, a "Predictive Open-Loop Car Following Control (POL-CFC)" is proposed. Its basic idea has been obtained from "Car-Following Control (CFC)" law [15].

4.3.1 Car-Following Control (CFC) Law

Suppose a car, F, is moving with a velocity V_F and is following another car, L, moving with a velocity V_L, as shown in Figure 4.2. The letters 'F' and 'L' in the subscript stands for "follow" and "lead", respectively. Let the positional error between the cars be denoted by e. Then, the basic Car-Following Control (CFC) law is simply defined as [15]:

$$V_F[new] = V_L + f(e), \tag{4.1}$$

where $f(e)$ is a function of the positional error. The control law states that "the new velocity of the *follow* car should be set to the velocity of the *lead* car plus a velocity adjustment based upon the positional error between them". This simple control strategy has some desirable characteristics [15]:

- When the *lead* car stops, the $f(e)$ term still drives F to a proper steady state.
- Direction reversal of L can result in proper control of F.
- By attempting to match the *lead* velocity, the *follow* car can maintain *smooth* tracking, while the *lead* car is in transit. This is not the case for "bang-bang" control laws (e.g. [14]), that generate the control signals based upon only the positional error (e) and causes the undesirable oscillations.
- The function $f(e)$ can use closed forms to determine what correction term is required to minimize e, within a given time bound and given current velocities.

4.3.1.1 Proposed Implementation of CFC

Given a servo-motor PTU and a moving object in the video frames, the velocity of the object relative to that of the PTU in terms of PTU degree/second has two components: relative pan velocity ($v_{rp,n}$) and relative tilt velocity ($v_{rt,n}$), where n represents the time step. These velocity components can be approximated as:

$$\begin{aligned} v_{rp,n} &= C_{dpp}\frac{\Delta x}{\Delta t} = C_{dpp}\left(\frac{x_n - x_{n-1}}{T}\right), \\ v_{rt,n} &= C_{dpp}\frac{\Delta y}{\Delta t} = C_{dpp}\left(\frac{y_n - y_{n-1}}{T}\right), \end{aligned} \tag{4.2}$$

where T is the sampling time, which is the inverse of the frame rate, and C_{dpp} is the conversion factor, which converts the units of the velocities from pixels/second into

degrees/second. The value of C_{dpp} for every zoom level of the camera is obtained by a simple and effective camera calibration procedure discussed in Section 4.3.3. It may be noted, that x_n and y_n are the target coordinates coming from the visual tracking algorithm at time step n. The new pan and tilt velocities of the PTU (i.e. the *follow* velocities) can then be estimated as:

$$\begin{aligned} v_{p,n+1} &= \left[v_{fp,n} + \left(-v_{rp,n} \right) \right] + Ke_{x,n}, \\ v_{t,n+1} &= \left(v_{ft,n} + v_{rt,n} \right) + \left(-Ke_{y,n} \right), \end{aligned} \tag{4.3}$$

where $v_{fp,n}$ and $v_{ft,n}$ are the current pan and tilt velocities of the PTU motors fed back by speed sensors, and K is the proportional gain parameter, which can be experimentally set for every zoom level. Furthermore, e_x and e_y in Eq. (4.3) are the positional errors in x and y axes, respectively. These errors are computed as:

$$\begin{aligned} e_{x,n} &= r_x - x_n, \\ e_{y,n} &= r_y - y_n, \end{aligned} \tag{4.4}$$

where r_x and r_y are the coordinates of the reference point (or *track-point*), which is normally the center of the video frame. The CFC law described by Eq. (4.3) commands the PTU to move the camera towards the object, so that the object remains always at the track-point. The first two terms in each equation in Eq. (4.3) represent the *absolute* lead velocity, while the last term represents the $f(e)$ function (or *approaching* velocity), as mentioned in Eq. (4.1). The plus and the minus signs in Eqs. (4.3)-(4.4) compensate the difference between the directions in the pixel coordinate system and the PTU coordinate system. It is assumed that the pan velocity is positive, if the PTU is moving towards left, and the tilt velocity is positive, if the PTU is moving downwards. However, the x coordinate of an object in an image

increases when the object moves towards right, and its y coordinate increases when the object moves downwards.

4.3.2 Predictive Open-Loop CFC (POL-CFC)

The basic CFC law implemented by Eq. (4.3) assumes that the current pan-tilt velocities (i.e. $v_{fp,n}$ and $v_{ft,n}$) of the PTU are fed back to the control algorithm through some velocity sensors. But, unfortunately, the PTU used in the current research is a stepper-motor mechanism instead of a servo-mechanism. Therefore, its does not feed back its current pan-tilt velocities. In control theory, such a system is referred to as "open-loop" system. The proposed POL-CFC algorithm eliminates the requirement of the current velocities. It simply replaces these velocities with the previously generated pan-tilt velocities, and uses an η factor to smooth the amount added to the previously generated velocities to compute the new velocities. Furthermore, it uses the predicted position of the target in the image rather than its current position. The predicted position is estimated by the Kalman filter, discussed in Section 3.3.10. The predicted position is exploited so that the PTU can be ready one step ahead of time to accurately reach the angular position corresponding to the 3-D position of the target at the same time when the target is supposed to reach there. The proposed POL-CFC algorithm generates the new pan-tilt velocities as:

$$\begin{aligned} v_{p,n+1} &= v_{p,n} + \eta\left[\left(-v^{*}_{rp,n+1|n}\right) + Ke^{*}_{x,n+1|n}\right], \\ v_{t,n+1} &= v_{t,n} + \eta\left[v^{*}_{rt,n+1|n} + \left(-Ke^{*}_{y,n+1|n}\right)\right], \end{aligned} \tag{4.5}$$

where the positive and the negative signs compensate for the difference between the image pixel coordinate system and the PTU coordinate system, as mentioned previously. Furthermore, η is a positive constant such that $0.0 < \eta < 1.0$, which controls the amount of velocity added to the *previously* generated velocity command.

The value of η is set to 0.145 to have smooth change in the PTU velocity. K is the proportional gain parameter, which is tuned for every zoom level as given in Table 4.1 to have 0% overshoot [defined in Eq. (4.9)] to track the target without any oscillation effect. Moreover, $e^*_{x,n+1|n}$ and $e^*_{y,n+1|n}$ are the predicted errors in both the axes, which are defined as:

$$\begin{aligned} e^*_{x,n+1|n} &= r_x - x^*_{n+1|n}, \\ e^*_{y,n+1|n} &= r_y - y^*_{n+1|n}, \end{aligned} \tag{4.6}$$

where $x^*_{n+1|n}$ and $y^*_{n+1|n}$ are the predicted coordinates of the target in the image estimated by Kalman filter in Eq. (3.23). The $v^*_{rp,n+1|n}$ and $v^*_{rt,n+1|n}$ in Eq. (4.5) are the predicted velocities of the target *relative* to those of the PTU in degree/second. They are approximated as:

$$\begin{aligned} v^*_{rp,n+1|n} &= C_{dpp}\left(\frac{x^*_{n+1|n} - x^*_{n|n-1}}{T}\right), \\ v^*_{rt,n+1|n} &= C_{dpp}\left(\frac{y^*_{n+1|n} - y^*_{n|n-1}}{T}\right). \end{aligned} \tag{4.7}$$

It may be noted that $v_{p,n}$ and $v_{t,n}$ in Eq. (4.5) are the pan and tilt velocities generated by the POL-CFC controller in its previous iteration, and they are only the *approximations* of the actual current velocities of the PTU. The reason for saying that they are approximation is that it is not necessary that the PTU has attained the previously generated velocity within a small sampling time, T, due to the practical limitations (e.g. the motor response, the inertia of the PTU and the camera, etc). For example, if an object is captured from a region, which is far from the center of the frame, the control algorithm will go on increasing the velocity very quickly, since the

motors take some time to start from stand-still. Before the motors start moving, the algorithm-generated velocity will be increased up to the saturation point, and there can be an unacceptable overshoot. In order to control this phenomenon, the following limit conditions are applied on $v_{p,n+1}$ and $v_{t,n+1}$ after they are computed by Eq. (4.5):

$$v_{n+1} = \begin{cases} \dfrac{K}{K_1}\left(\dfrac{v_{\max}}{12}\right) & \text{if } n \le 12 \\ v_{\max} & \text{if } n > 12 \text{ and } v_{n+1} > v_{\max} \end{cases} \tag{4.8}$$

where the time step n is initialized to 1 at the start of the tracking session, K_1 and K are the proportional gain parameters for the 1× zoom level and the current zoom level of the camera, respectively, $v_{\max}$ is the maximum velocity of the pan-tilt unit (which is

Table 4.1 The values of K for different zoom levels of the camera to have 0% overshoot

Zoom Level	*K*
1	12
2	6
3	5
4	4.4
5	3.4
6	2.8
7	1.8
8	1.4
9	1.2
10	1
11	0.9
12	0.9
13	0.9
14	0.9
15	0.9
16	0.8
17	0.7
18	0.7
19	0.6
20	0.6
21	0.6
22	0.5
23	0.4
24	0.3
25	0.3

77.1 degrees/second for the PTU used in this research as specified in its specification sheet), and the constant number is set to the smallest value (i.e. 12 in this research) which can result in zero overshoot and efficient target following behavior of the tracking system.

4.3.3 Determining C_{dpp} Factor

This section briefly describes the calibration method for obtaining the conversion factor C_{dpp} used in the proposed pan-tilt control algorithm. The subscript "*dpp*" stands for "degrees per pixel", which indicates that the conversion factor is basically a ratio of the degrees, that the PTU must traverse to cause an object to move by one pixel in the video frame. The C_{dpp} is determined as described in the following steps.

Step 1: Find a stationary object having a sharp vertical edge in the video.

Step 2: Move the PTU towards right, so that the sharp edge of the object reaches the left edge of the video frame.

Step 3: Note the step index of the current pan position of the PTU, i.e. s_l.

Step 4: Note the index of the left-most column of the video frame, i.e. x_l.

Step 5: Move the PTU towards left, so that the same sharp edge of the object reaches the right edge of the frame.

Step 6: Note the step index of the current pan position of the PTU, i.e. s_r.

Step 4: Note the index of the right-most column of the frame, i.e. x_r.

Step 5: Let r_{ptu}, having unit of degree/step, be the resolution of the PTU. Then, calculate the value of the C_{dpp} as:

$$C_{dpp} = r_{ptu} \left| \frac{s_l - s_r}{x_l - x_r} \right| \tag{4.9}$$

The resolution of the stepper-motor PTU and the frame size used in the present research are 0.01285 degree/step and 320×240 pixels, respectively. Therefore, r_{ptu} = 0.01285, x_l = 0 and x_r = 319. Thus, Eq. (4.9) can be simplified as:

$$C_{dpp} = 0.01285 \left| \frac{s_r - s_l}{319} \right| \tag{4.10}$$

For example, when the camera was operating in its first zoom level, the pan step-indices were: s_l = 3353 and s_r = 128. Thus, for this zoom level, C_{dpp} = 0.1299 degree/pixel. Similarly, the conversion factors for the higher zoom levels of the camera were determined very easily using Eq. (4.10).

4.3.4 Performance Analysis of POL-CFC

In order to evaluate the performance of the POL-CFC algorithm, a stationary object was selected from the top-left section of the live video from the camera and the algorithm was let to generate the appropriate pan-tilt velocities to move the camera to centralize the object in the video frames. Figure 4.3 shows the instantaneous position of the object in the video frame, the instantaneous control action (velocity) generated by the proposed controller and the instantaneous positional error in both the axes, while the object was being centralized. It is again reminded, that the PTU moves to the left, if $v_p > 0$, and upwards, if $v_t < 0$. The curves illustrate that initially the controller generates a constant velocity using Eq. (4.8) to start the motors from rest. When the controller senses that the positional error is not reduced adequately, it starts increasing the speed after about 0.4 second. As a result, the object starts coming closer and closer to the center of the frame, i.e. (160, 120), efficiently, within the time

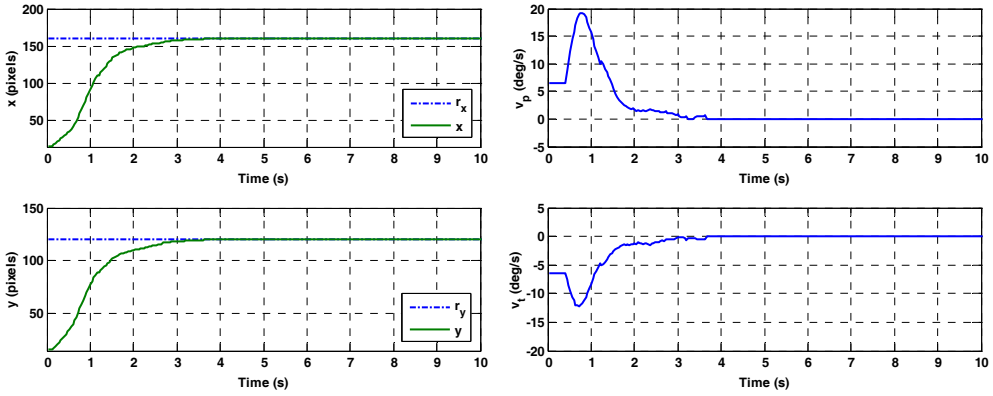

(a) Target trajectory in the video frames (b) Velocity generated by the POL-CFC

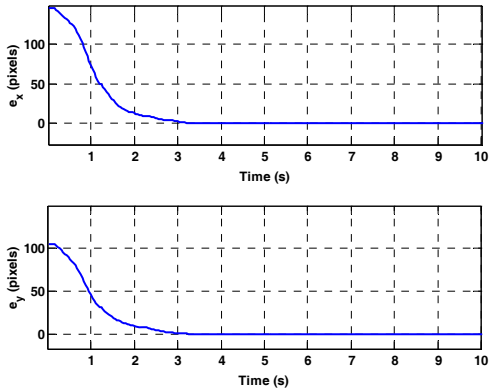

(c) Tracking error with respect to center of the frame

Figure 4.3 Target trajectory, generated velocity, and tracking error curves in both axes, when a stationary object was being centralized in the video frames by the proposed tracking system.

span between 0.5 to 1.5 seconds, as shown in Figure 4.2(a). When the error is reduced significantly and the current PTU velocity is greater than it should be for the current position of the object, the control algorithm reduces the velocity smoothly until the object approaches the center of the video frame. It can be observed that there is 0% overshoot, 1.7 second rise time, and zero steady state error. The *percent overshoot* and *rise-time* are the parameters which describe a system in its transient period. The percent overshoot is defined as [56]:

$$\%OS = 100 \times \frac{(p - r)}{r} \tag{4.11}$$

where p is the peak value and r is the reference (or track-point). The rise time is referred to as the time taken by the system to rise from 10% to 90% of the reference

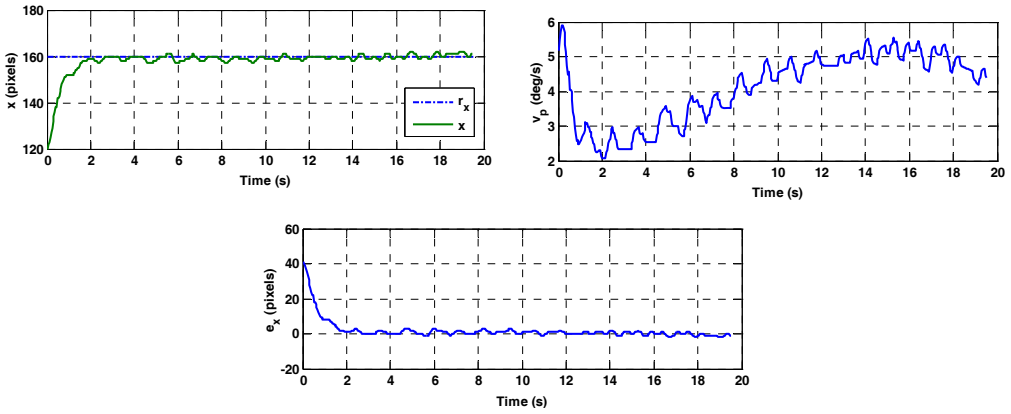

Figure 4.4 Target trajectory, velocity and tracking error curves for pan motion, when a walking person was being tracked.

(or track-point) [56]. The steady state error is the deviation of the target coordinates from the track-point, after the transient period of the system has passed. Thus, the stationary target selected from a position farthest from the center of the frame is *perfectly* centralized within 3 seconds.

The performance of the system was also tested for various moving objects such as helicopters, airplanes, vehicles, walking and running persons, etc. in real-world scenarios. In Figure 4.4, the results for a person with varying walking speed are presented. Since there was no significant motion in the tilt axis in this example, the results are shown only for the pan axis. It can be observed that the object is perfectly centralized within 2 seconds and then it remains centralized accurately regardless of the increasing velocity of the object. The small vibration in the curves is due to the jerky motion of the walking person. This kind of vibration does not occur, when the object being tracked is moving smoothly, e.g. airplane, helicopter, etc. In order to validate the statement, the target trajectory in x-axis, the pan velocity, and the tracking error in x-axis for the case of a flying helicopter are shown in Figure 4.5. In this scenario, the helicopter was captured from the position $(x, y) = (192, 118)$ in the frame as shown by the initial point in the trajectory curve. Since the helicopter was moving fast towards right and the camera was initially stationary, the helicopter in the video

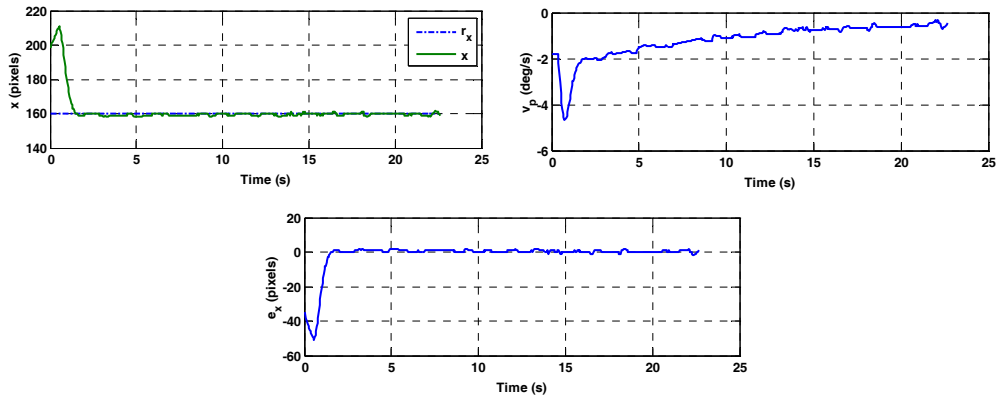

Figure 4.5 Target trajectory, velocity and tracking error curves for pan motion, when a flying helicopter was being tracked.

moved further towards right. This is shown by the initial upward bulge above x = 192 in the trajectory curve. The PTU motion catches up with the helicopter motion after about 0.4 second. Then, the control algorithm starts centralizing the helicopter very efficiently. It can be seen in the curves that the helicopter is finally centralized by about 1.4 seconds and it remains at the center of the frames afterwards with the maximum steady state error of only ±1 pixel. This experiment was performed, when the camera was operating at 5x zoom level, and some frames from the resulting video are shown in Figure 4.7.

The pan-tilt control algorithm has been calibrated for 1x to 25x zoom levels of the video camera. The *maximum steady-state errors* of the proposed tracking system at different zoom levels for the target moving without abrupt change in its direction are listed in Table 4.2. These errors are negligible because of the very small size of one pixel in a 320×240 pixel frame.

4.4 Experimental Results

The active camera tracking system has been tested rigorously for at least a whole year in numerous real-world and complex scenarios. Some of the results are shown and discussed as follows.

4.4.1 Tracking a Distant and Faded Airplane

Figure 4.6 shows some frames from the tracking session, in which a very distant and dim airplane is being tracked very smoothly with the proposed tracking system. The white target sign (i.e. the circle with a constant radius and the four line segments) shows the object localization result produced by the visual tracking module. In fact, the center of the best-match rectangle (BMR) is the same as that of the circle. The white dot at the center of every frame represents the line-of-sight of the camera. It is overlaid in order to validate the accuracy of the pan-tilt control algorithm. The small image at the bottom-right of every frame is the current edge-enhanced, updated and adjusted template. The text overlaid at the top of every frame shows the current correlation peak value ($c_{\max}$), BMR center coordinates (x, y), zoom level of the camera, W (showing that the search of the target is being carried out in a small dynamic search **w**indow instead of the whole frame), and the generated pan-tilt velocities of the PTU, i.e. (v_p, v_t). The text overlaid at the bottom of every frame shows the date and time when the tracking was performed. It can be observed that the user has initialized the template incorrectly (as shown in Frame 1) due to the motion of the airplane in the video, such that the template is much larger than the object and the object is not at the center of the template. The BMR adjustment algorithm in the proposed visual tracking module resizes/relocates the BMR very efficiently. As a

Table 4.2 *Maximum* steady state error of the proposed tracker at different camera zoom levels

Camera Zoom Level	***Maximum* Steady State Error (in pixels)**
1x to 6x	±1
7x to 15x	±2
16x to 19x	±3
20x to 25x	±4

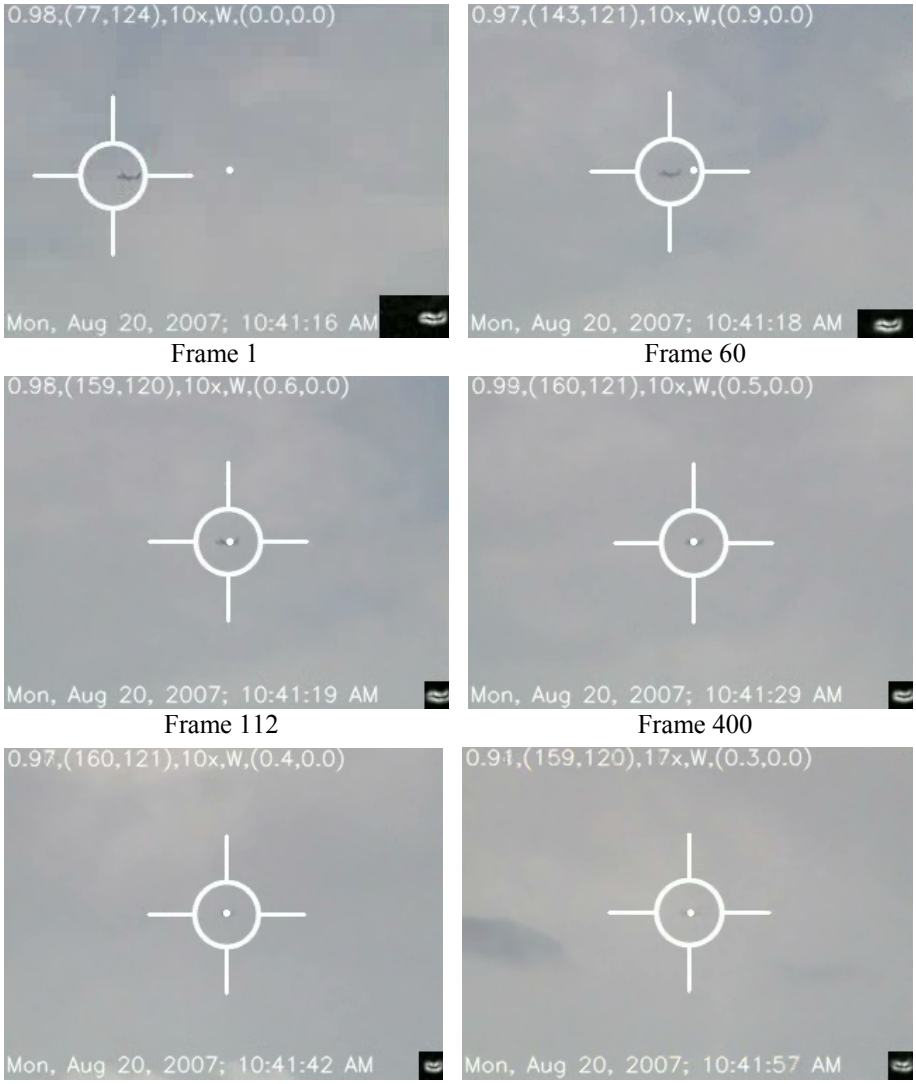

Figure 4.6 Tracking a very distant airplane robustly with the proposed tracking system even in the presence of incorrect template initialization, clouds, and object fading (obscuration) in very low contrast imagery.

result, the target is tightly enclosed by the BMR and the template in a few initial iterations. The pan-tilt control algorithm initially centralizes the airplane in the video and then the airplane remains always at the center of the video with only ±1 pixel maximum steady state error, even when the zoom level of the camera is varying from 10x to 17x. This steady state error at high zoom levels is well below the maximum steady state error reported in Table 4.2. The tracking is continued robustly, even when the object is very small in the cloudy scene and there is object fading and obscuration

resulting in very low contrast between the object and the background. The robustness of the proposed tracker to the object fading is due to the proposed EE-BCFNC algorithm, discussed in Section 2.3.5. The tracking is stopped, only when the airplane is completely vanished from the scene after Frame 1227.

4.4.2 Tracking a Helicopter

Figure 4.7 illustrates some frames from the video, which was recorded while tracking a helicopter. Due to the motion of the helicopter, the user has again selected the initial

Figure 4.7 A helicopter is being tracked persistently and smoothly with the proposed tracking system even when the template was incorrectly initialized by the user and the size of the object is being reduced to about 3×3 pixels.

template incorrectly as shown in Frame 1. The overlaid white rectangle is the best-match rectangle (BMR). The BMR adjustment algorithm in the proposed visual tracking module resizes/relocates the BMR very efficiently. As a result, the helicopter is tightly enclosed by the BMR within 35 frames. The pan-tilt control accurately centralizes the target within 40 frames (≈ 1.6 s), and this is even below the 1.7 second rise time of the pan-tilt control system as mentioned in Section 4.3.4. After the initial target centralization, the camera is always pointing precisely to the helicopter regardless of its ever decreasing size and varying shape. The tracking is stopped only when the helicopter disappears beyond a hill.

4.4.3 Tracking a Crow Flying with Variable Velocity

A crow flies with abrupt variation in its speed. Its appearance is always varying due to the up and down motion of its feathers. Figure 4.8 shows how efficiently the proposed system is persistently tracking it, until it disappears beyond a building. Initially, due to the fast motion of the crow, the template is initialized incorrectly by the user, as shown in the template at the bottom-right of Frame 1. The BMR adjustment algorithm automatically resizes/relocates the template to tightly enclose the crow. Furthermore, the tracker is not disturbed, even when the zoom level of the camera is varied from 3x through 7x in this example. The pan-tilt control algorithm centralizes the target in the frame efficiently within only the first 1.47 seconds. Later on, the crow remains mostly at the center of the frame. However, sometimes the crow moves *slightly* away from the center of the frame due to the *abrupt* change in its direction of motion.

4.4.4 Tracking a Maneuvering Kite and Handling Occlusion

Figure 4.9 depicts some frames from a tracking session, in which a kite (a highly maneuvering bird) is being tracked by the proposed system. It may be noted that the

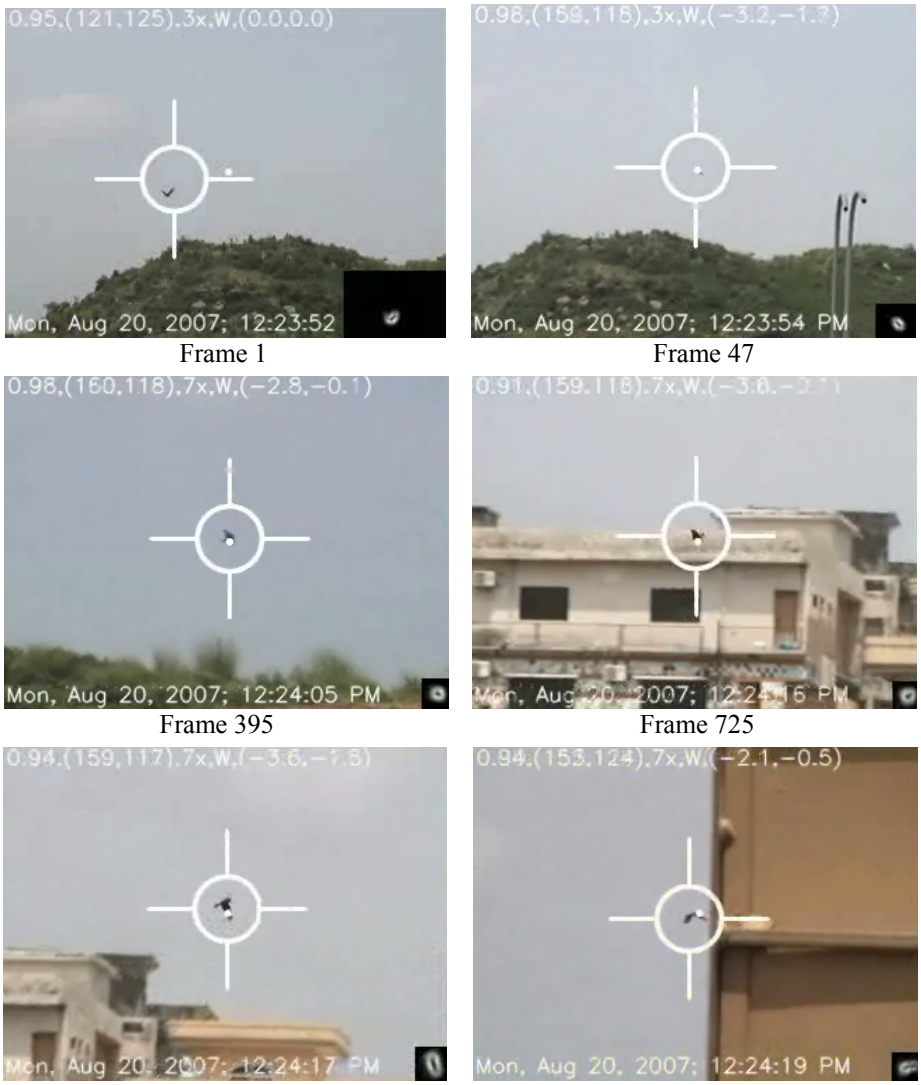

Figure 4.8 Tracking a crow persistently even in the presence of sudden variation in appearance, speed, background, and camera zoom (from 3x to 7x).

appearance, the speed and the motion direction of the kite changes continuously. The current template is shown at the bottom-left of every frame in the figure. It can be observed in the frame sequence that: (1) it is very far from the camera and it looks very small even at the zoom level from 8x through 25x, and (2) there are multiple similar kites in the scene and one of them is occluding the kite of interest in Frames 1565 through 1585 (only Frame 1574 is shown due to space constraint). Even then, the proposed tracking system is tracking the kite of interest robustly without any problem or distraction. The yellow color of the overlaid content in Frame 1574

indicates that the correlation peak value has dropped below the threshold, τ_t, and the tracker is working in its occlusion handling mode (discussed in Section 3.3.9), during which the template is not updated. Normal tracking is resumed from Frame 1586, when the correlation peak value rises above the current dynamic threshold calculated in Eq. (3.6) during the occlusion handling mode of the tracker.

4.4.5 Tracking a Person in the Shrubbery

Figure 4.10 shows how the proposed system tracks a man walking in the cluttered

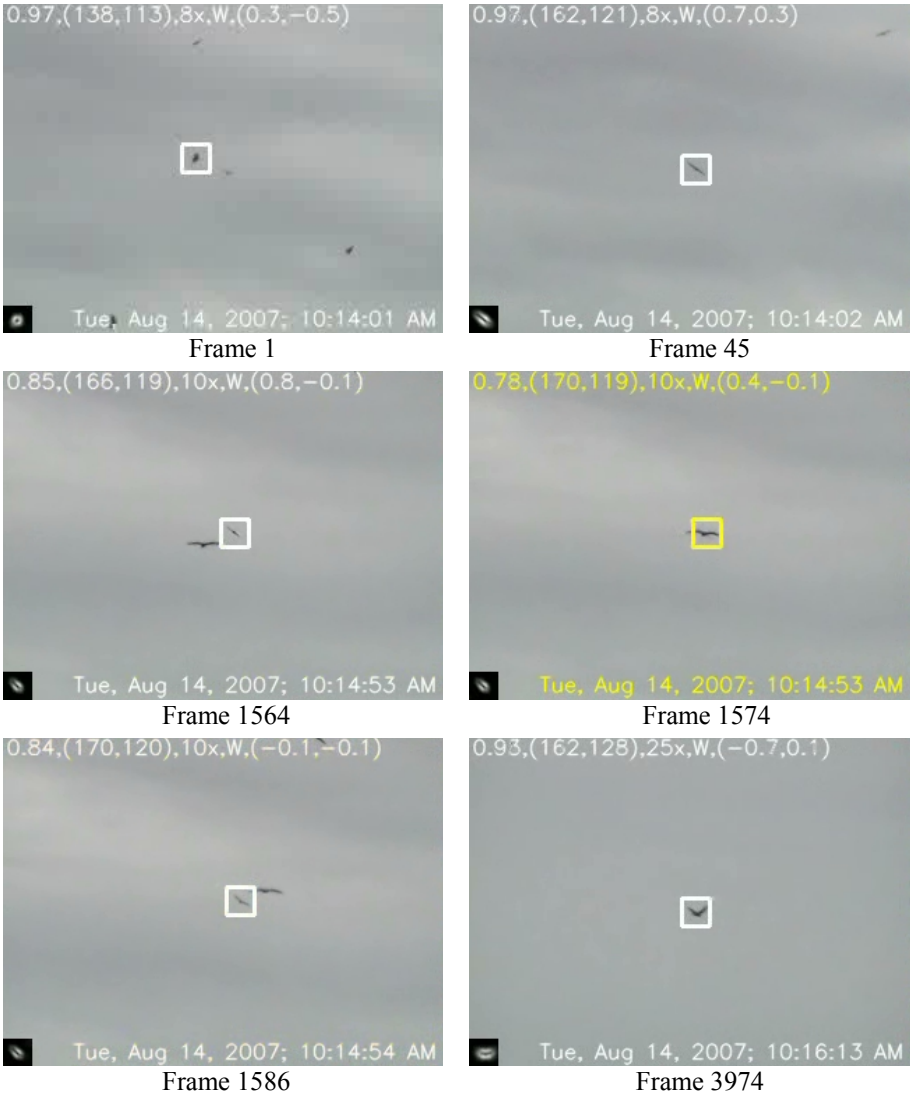

Figure 4.9 Tracking a distant kite with the proposed tracking system for long duration, even in the presence of its ever-changing direction and appearance, varying zoom level, multiple similar objects, and occlusion (Frames 1565 to 1585). Yellow overlaid content in Frame 1574 indicates that the tracker is working in its occlusion handling mode.

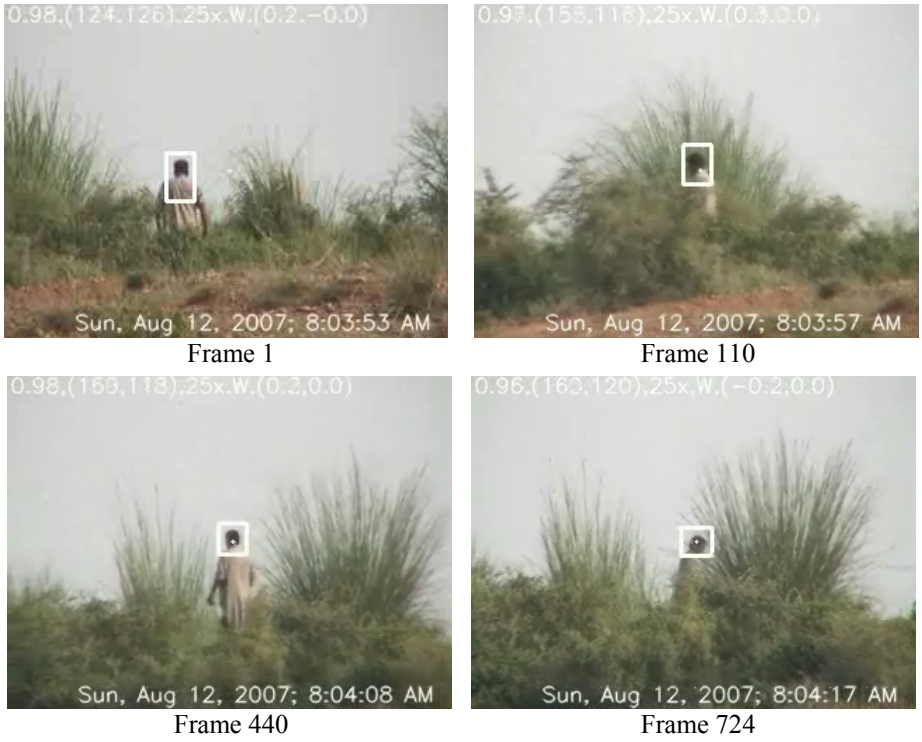

Frame 1 Frame 110

Frame 440 Frame 724

Figure 4.10 Tracking a man walking in the cluttered shrubbery at the highest zoom level (25x) of the camera used in this research, until he disappears beyond a bush.

scene and it is not distracted by the shrubs. The zoom level of the camera in this example is continuously at 25x, which is the maximum zoom level of the camera. This much zoom level is challenging for any pan-tilt control, because the field of view (FOV) is significantly reduced, and a very small angular motion of the camera reflects a very large motion of the object in the video. However, the proposed control algorithm moves the camera smoothly to follow the target accurately even in this situation. The tracking is stopped, only when the man disappears beyond a dense bush.

4.4.6 Tracking a Car in Clutter and Occlusion

Figure 4.11 shows some frames from a successful tracking video, in which a car is being tracked in the presence of a highly cluttered scene (i.e. houses, trees, shrubs, etc) and two occlusions (once by a motorcycle as shown in Frame 250 and another time by a big bulb on the gate of a home as shown in Frame 348). The yellow color of

the overlaid content represents normal tracking mode and the dark yellow color represents the occlusion handling mode of the tracking system. It may be observed that the scale (i.e. size) of the car is increasing in the video frames, but the template is not expanded by the BMR adjustment algorithm or the scale handling method. This is because the initial template is already larger than the maximum size limit of the template (see Section 3.3.8).

4.4.7 Face Tracking in Uneven Illumination and Occlusion

Figure 4.12 illustrates how efficiently the proposed system tracks the face of a person, who is walking in a room with all the lights turned off. The only light, that was available in the room, was coming from the blinds shown in the frames. This natural

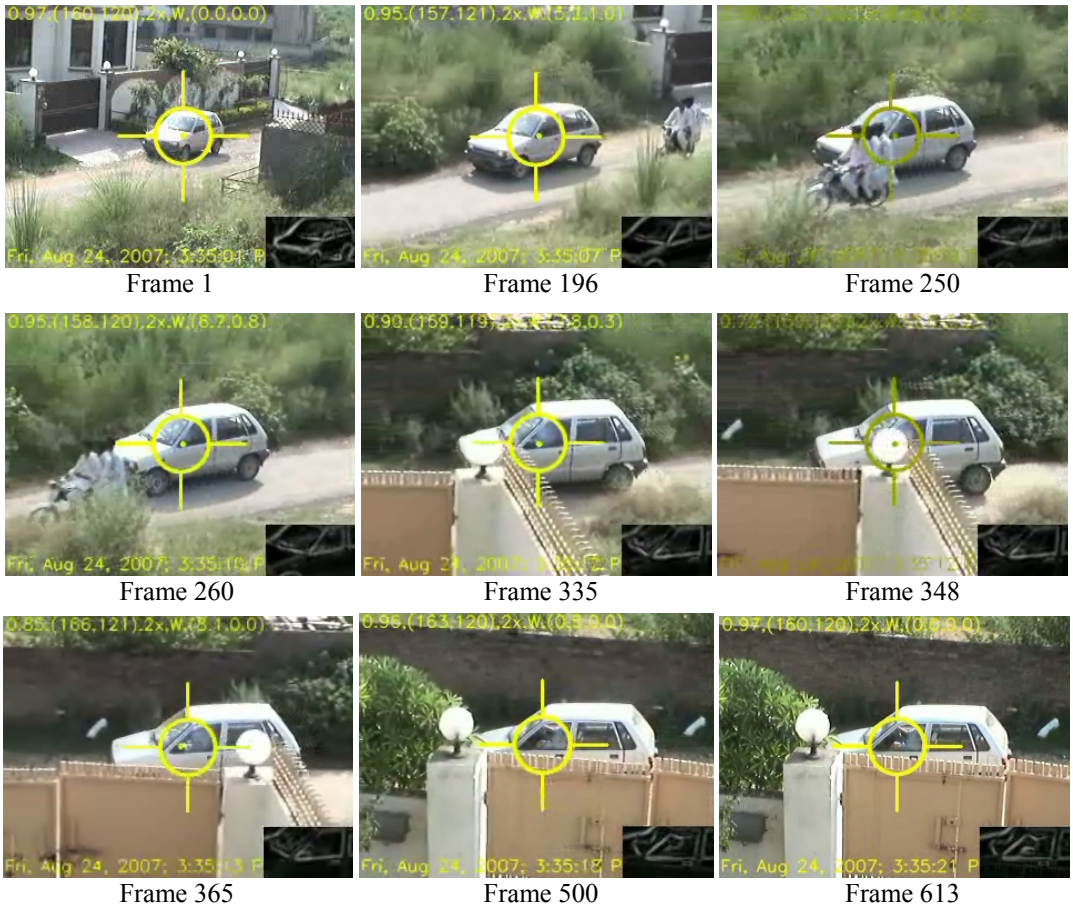

Figure 4.11 Tracking a car in a highly cluttered scene and multiple occlusions. The yellow color of the overlaid content indicates the normal tracking mode and the dark yellow color (in Frame 250 and 348) indicates the occlusion handling mode of the tracking system.

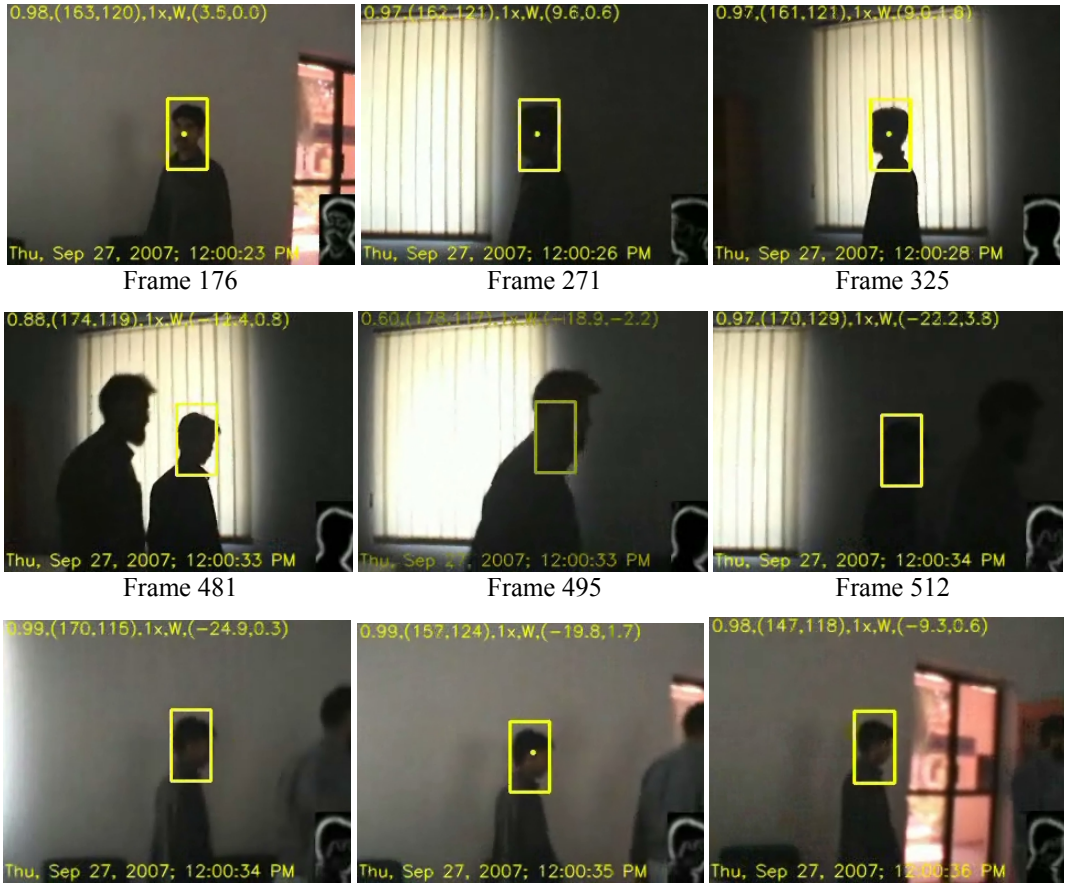

Figure 4.12 Tracking the face of a person during severe illumination variation, noise, low detail, and occlusion. All the lights in the room were turned off in this experiment to create a challenging scenario. The dark yellow rectangle in Frame 495 indicates that the tracker is currently working in its occlusion handling mode.

light created a severe illumination variation in the video, since the camera was operating on its auto-focus mode in front of the light source. Specifically, when the camera was looking in the direction of the bright window, the other things (persons, wall, etc.) became very dark (see Frames 271 to 512), and when there was no bright window in the video frames, the whole scene became a little clearer. It may be noted, that there is noise and no detail in the whole video due to low light conditions. The target person and the occluding person are both walking in the *same* direction making the scenario even more complex. It can be further observed in Frame 495, that the occlusion of the tracked person by the other person happens partly in the bright region and partly in the dark region of the video frame. Moreover, the track of the target

person after the occlusion is resumed in *very much dark*, as shown in Frame 512. Since the persons were very near to the camera, even a small movement of the persons was reflecting a large movement in the video frames. Thus, it was a challenging experiment for the pan-tilt control algorithm as well. All the problems (i.e. severe illumination variation, noise, low detail, full occlusion, and fast motion) are handled very efficiently and robustly by the proposed tracking system in real-time, and the face of the person of interest is always at (or near) the center of the video frames.

4.4.8 Tracking a Goat amidst Multiple Goats in Clutter and Noise

Figure 4.13 depicts some frames from a tracking session performed at about 7:26 p.m. in the evening. The scene is very cluttered and noisy. A goat has been selected by the user from the top of the video in Frame 1. The tracker centralizes the goat in the video

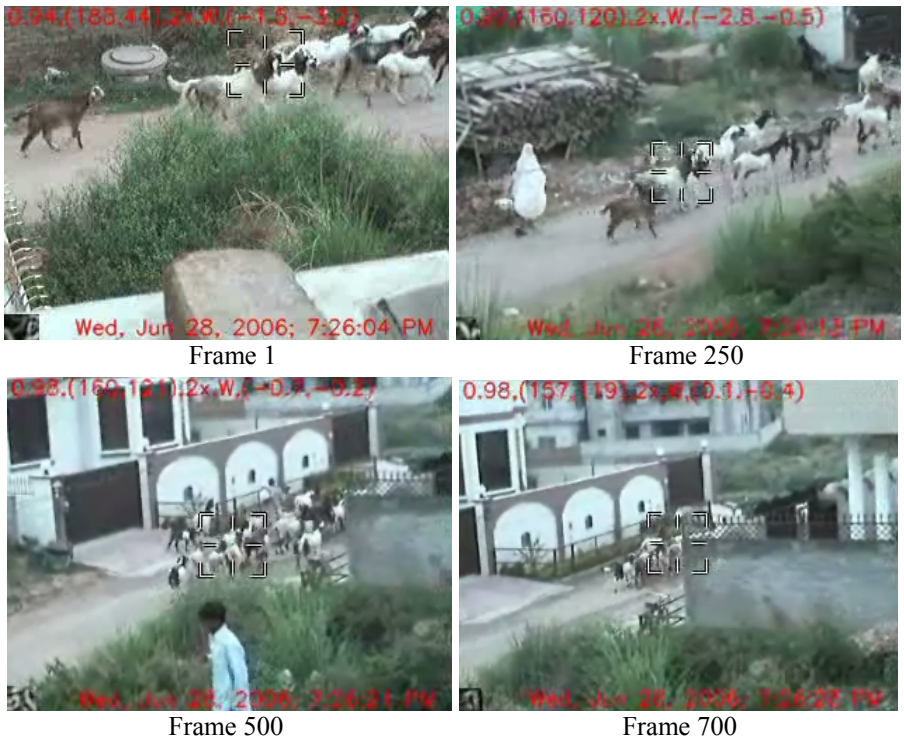

Frame 1 Frame 250

Frame 500 Frame 700

Figure 4.13 Tracking a goat amidst many other goats in a highly cluttered and noisy scene at about 7:26 p.m. in the evening. Initially, the front part of the goat is selected by the user from top of the video. The goat is then centralized and tracked until it disappears beyond a home.

and tracks it robustly and persistently in the middle of many other goats, until it disappears beyond the wall of a home. This tracking session shows the robustness of the visual tracking algorithm to the noise, other similar objects, and background clutter (i.e. grass, homes, people, logs, stones, debris, etc).

4.5 Chapter Summary

This chapter presented the design, implementation, analysis, and experimental results of the proposed active camera tracking system (ACTS), that exploited the visual tracking framework discussed in Chapter 3. The system offers 0% *overshoot*, 1.7 second *rise time*, and ±1 pixel *maximum steady state error*, if the object being tracked does not change its direction of motion *abruptly*. The experimental results validate that, due to the proposed visual tracking framework, the ACTS is quite able to track *any* object of interest with a *pan-tilt-zoom* camera in real-world complex scenarios, such as object fading, clutter, occlusion, uneven illumination, distraction by multiple similar objects, noise, and change in scale, orientation, appearance, and velocity of the object.

5

A Vision Based System for a UGV to Handle a Road Intersection

5.1 Chapter Overview

This chapter presents the design and implementation of a machine vision system that exploits the proposed visual tracking framework discussed in Chapter 3. The system enables an unmanned ground vehicle (UGV) to automatically handle a road intersection [57]. The experimental results of the actual system deployed on a UGV are also shown to validate its performance.

5.2 Problem Description

Consider the scenario of a UGV approaching a four way intersection regulated by a stop sign. Traffic laws require that each vehicle must come to a stop before entering the intersection and allow any other vehicles that arrive earlier to pass first. The UGV must effectively wait for its turn and look for the leading vehicles at the other roads that want to pass the intersection. It is not sufficient to simply detect the presence of other vehicles at the intersection, since the UGV should have the right-of-way if other vehicles approach the intersection after it has already stopped. Thus, it will be necessary to determine the behavior of each other vehicle, i.e. whether it is just arriving at the intersection, waiting for its turn to go, or already passing through. It is

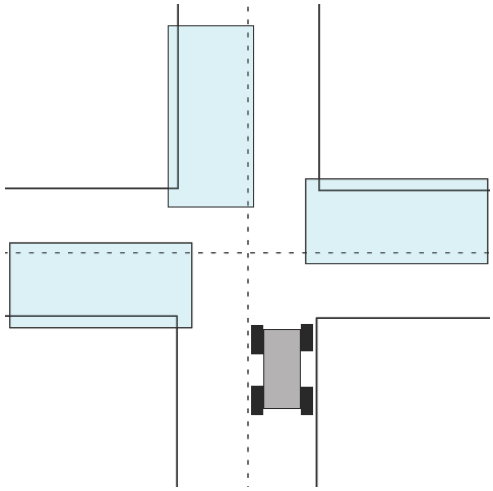

Figure 5.1 The four way intersection scenario. All vehicles must come to a stop before entering the intersection. The UGV must be aware of incoming vehicles in the right-hand lane of each of the three roads (left, front, and right), in the regions indicated by the shaded boxes.

assumed that all intersections will have at most four incoming roads oriented at perpendicular angles and that all vehicles will travel in the right-hand lanes according to USA traffic rules. Thus, the on-board computer vision system must be aware of the vehicles in the three regions shown in Figure 5.1, once the UGV has come to a stop.

Some further relaxations regarding traffic flow to simplify the problem are made. If another vehicle approaches from the road straight ahead, beats the UGV to the intersection, and begins to make a right hand turn (a turn to the UGV's left), the UGV could safely make a right hand turn without having to wait. For simplicity, the UGV is programmed to decide not to cross the intersection until the intersection is completely clear of other vehicles. It is also assumed that the UGV will encounter only small vehicles with four or more wheels, but of any color or shape (e.g., a compact convertible or a pickup truck, but not a motorcycle or a semi-truck).

The DARPA Urban Challenge 2007 provided a map of GPS paths along the lanes of the road, so it is unnecessary to perform path planning. The map also includes the locations of each regulated intersection and the possible directions of cross-traffic,

Figure 5.2 The experimental UGV is a Subaru Outback with an autopilot system and three cameras mounted to the roof.

so it is not required to detect the number of roads or the presence of a stop sign. The experimental UGV is a Subaru Outback station wagon that has been used in previous autonomous vehicle projects by the Team UCF (University of Central Florida). It is equipped with a GPS receiver, several racks of off-the-shelf computers, mechanical controls for the steering wheel, brakes, and accelerator, and an autopilot system that autonomously follows GPS waypoints. Thus, it is also unnecessary to consider low-level controls; it is instead sufficient to inform the autopilot when it is the UGVs turn to proceed through intersection.

5.3 Overview of the Proposed Solution

The proposed vision system uses three video cameras mounted to the roof of the UGV, as shown in Figure 5.2. The cameras are pointed towards the three other roads leading to the intersection, i.e. to the right, to the left, and straight ahead. Each camera provides RGB color frames with a resolution of 320×240 at a frame rate of 30 fps. Each camera is connected to a separate off-the-shelf computer installed in the UGV. Each computer will run the proposed software, which is written in C++. The three computers communicate with the autopilot through a UDP Ethernet connection.

When the autopilot determines that the UGV has reached the intersection and has come to a stop, it will send a message to the three computers signaling them to begin looking for vehicles in their fields of view. The proposed software consists of three main components: a vehicle detector, a tracker, and a finite-state-machine (FSM) model of the traffic, as shown in Figure 5.3. First, the vehicle detector tries to detect a vehicle in each video frame by using an OT-MACH (Optimal Trade-off Maximum Average Correlation Height) filter [97, 98, 99] pre-constructed from training images of vehicles captured from each camera. Once a vehicle is detected in a single frame, the detector gives the position and size of the detected vehicle to the tracker. The tracker follows the vehicle in the subsequent frames, adapts to the changing appearance of the vehicle, handles occlusions, and estimates the current and

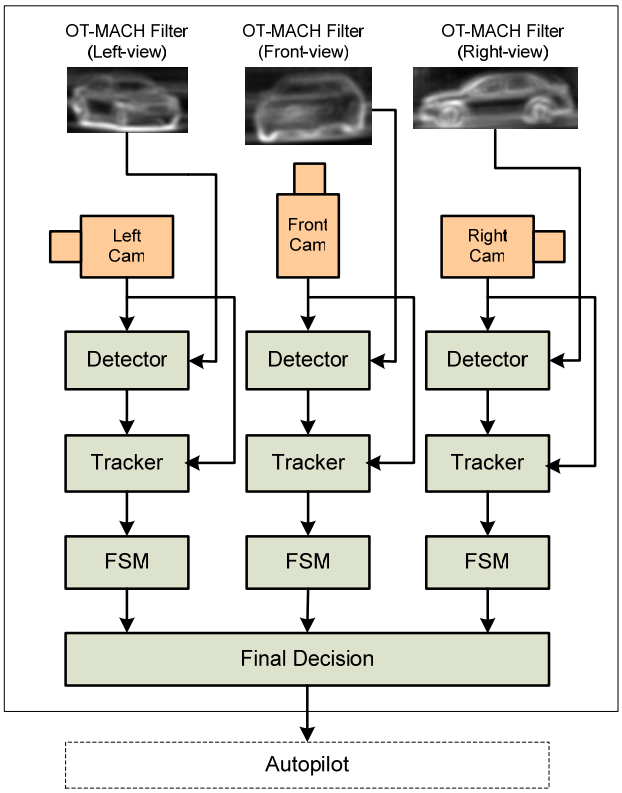

Figure 5.3 Block diagram of our proposed system. The *Vehicle Detector*, *Tracker*, and *Finite State Machine* (FSM) are run on the three on-board computers simultaneously for each camera view. The actual OT-MACH filters used for each view are also shown at the top.

next position of the vehicle in the imagery. A finite state machine (FSM) model is used to determine the state of the leading vehicle in each view. The states of the leading vehicle in each view are then used to make a final decision about when it is safe for the autopilot to drive the UGV through the intersection. All the components of the proposed solution are discussed separately in the next sections.

5.4 Vehicle Detector

The first step of the proposed solution is to detect a vehicle in a video frame by matching an appearance template that has been prepared for each of the three views. The template is basically an OT-MACH (Optimal Trade-off Maximum Average Correlation Height) filter, which combines the training images into a single composite template by optimizing four performance metrics: the *Average Correlation Height* (ACH), the *Average Correlation Energy* (ACE), the *Average Similarity Measure* (ASM), and the *Output Noise Variance* (ONV), as explained in [97, 98, 99]. Since each incoming vehicle from a given road is oriented in approximately the same pose, and since the UGV always sees each road in the intersection from roughly the same point of view, this method produces a template that expresses the general shape of a vehicle in each view. The color invariance is achieved by using edge-enhanced images instead of the original color frames as described in [58]. The edge-enhanced OT-MACH filter generated for each of the three views is shown in Figure 5.3.

Once the edge-enhanced OT-MACH filter is prepared, it is applied to edge-enhanced search window inside the incoming video frames by performing normalized cross-correlation very efficiently as discussed in Chapter 2. The highest peak in the correlation response is compared with a threshold. The threshold was determined just after the synthesis of the filter as $\tau = 0.95 \min(p_1, p_2, p_3, ..., p_N)$, where p_i is the correlation peak value obtained when the filter was applied on *i*th training image, and

N is the total number of the training images. The 95% of the minimum peak value is used in order to tolerate small amount of perturbation of the actual vehicles from the vehicles used in the training phase. If the peak is greater than the threshold, it indicates the position of a vehicle; otherwise it is assumed that there is no vehicle in the scene.

The most significant change in the appearance of vehicles between different intersections comes from varying number and width of lanes. A specific solution is proposed to this uncertainty in distance between the camera and the vehicle. The filter is obtained from the training images each resized to an average size, but the detection is performed with several rescaled versions of the average size filter. The scales are 80%, 100%, and 120% of the size of the original OT-MACH filter. After computing the correlation at each scale, the scale that produces the maximum correlation peak decides the size of the vehicle in the image.

5.5 Tracker

While the vehicle detector locates a vehicle in a single frame, the tracker is intended to follow the vehicle in the subsequent frames to determine its current and next position, velocity, and acceleration. The tracker is initialized using the image rectangle identified by the vehicle detector. While the detector uses only the prior knowledge of the appearance of a vehicle, the tracking stage ignores the prior knowledge and instead exploits the temporal and spatial consistency of appearance from frame to frame. This tracker is basically the same as the one discussed in Chapter 3. The current and predicted position of the vehicle coming from every road under observation is used by the finite-state-machine (discussed in the next section) to determine the state of the traffic on the intersection.

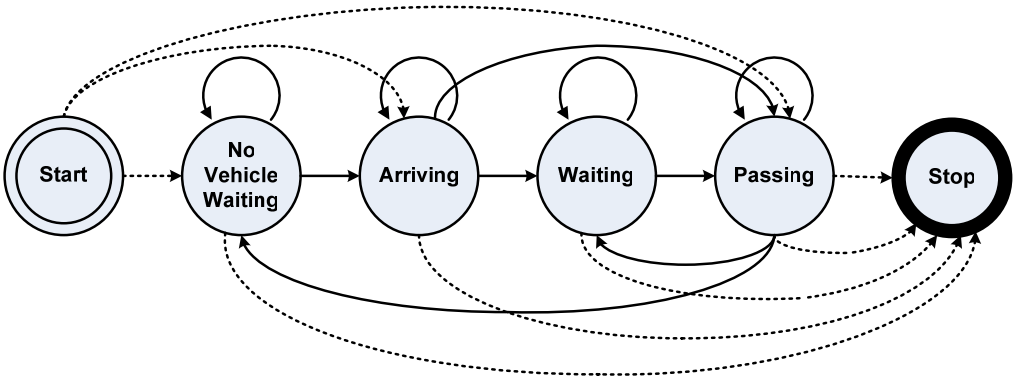

Figure 5.4 Finite state machine (FSM) model for the state of traffic on a road.

5.6 Finite State Machine (FSM) Model

The tracker provided the current and predicted position of the detected vehicle in each view. The goal of the intersection model is to use this information, along with prior knowledge about the geometry of the scenario, to determine which cars have the right of way and help make the final decision to be sent to the autopilot when it is the UGV's turn to cross the intersection.

The state of the traffic in each view is modeled with a finite-state-machine consisting of four states: *No Vehicle Waiting*, *Arriving at the intersection*, *Waiting*, and *Passing the intersection*. The relationships between these states are shown graphically in Figure 5.4. The state transitions are controlled by rules that operate on the dynamics information from the tracker.

The velocity and acceleration of the vehicle coming from the left or right road can be estimated easily by obtaining the left or right motion of the vehicle between the consecutive frames, but this kind of motion is not significant in case of the vehicle coming from the front road. This case is addressed by the scale that is obtained by the scale handling capability of the proposed visual tracking framework. If the ratio of the

size of the updated template to the size of the previous template is greater than 1, it means the vehicle is approaching towards the intersection from the front road.

The FSM transitions from *No Vehicle Waiting* to *Arriving* when a new vehicle is detected. After arriving at the intersection, the vehicle can be in two possible states: *Waiting* or *Passing*. The FSM transitions from *Arriving* or *Passing* to *Waiting* when the vehicle stops moving, i.e. when the velocity and acceleration of the vehicle in the x and y directions as well as the change in scale ratio (in front view case) drop below some threshold. As a guard against spurious state transitions, the vehicle must be still for about 15 frames (half a second) before it is considered *Waiting*. While in the *Arriving* state, the vehicle transitions directly into the *Passing* state if it crosses a spatial threshold, i.e. if the x coordinate crosses a threshold in the left and right views, or if either x or y coordinates cross a threshold in the front view. A transition from *Passing* to *Waiting* is permitted because the vehicle may unexpectedly have to wait due to some disturbance, such as a pedestrian, while it is passing the intersection. If the vehicle starts moving again, then it transitions back into the *Passing* state. Once in the *Passing* state, the FSM transitions again to *No Vehicle* once the vehicle reaches the edge of the frame.

Since the vision system is turned on by the autopilot once the UGV has stopped at the intersection, other vehicles may already be in the scene. If a vehicle is detected in the first frame, the FSM is allowed to begin with the *Arriving* or *Passing* state depending on the position of the vehicle in the frame. Similarly, the autopilot may turn off the vision system while the state machine is in any state.

5.7 Final Decision

In order to decide when to cross the intersection, the system combines the traffic information from all the three FSMs. If the vehicle on the other road is already *Waiting* when the UGV arrives at the intersection, then it has the right-of-way, and the UGV is commanded to wait for it to leave the scene before proceeding. If at any time a vehicle is *Passing* the intersection, the UGV is commanded not to cross. Since a vehicle will reach the edge of the frame before it has crossed the intersection, the UGV waits for two seconds after the corresponding FSM stops indicating that the vehicle is passing. Any vehicle that is *Arriving* or *Waiting* after the UGV arrives does not have the right-of-way, so it is assumed they will let the UGV pass the intersection.

5.8 Experimental Results

The low-level components of the system were tested by parking the UGV at several real four-way intersections at which one of the roads was a dead end, so the traffic was not interfered. It is easy to objectively evaluate the vehicle detector since the total number of visible vehicles is a discrete and unambiguous value. Table 5.1 shows the number of successfully detected vehicles, as well as the false alarms and misdetections for each camera view. The tradeoff between false alarms and misdetections is controlled by the parameters and thresholds. The misdetections were favored over false alarms, since if the tracker *got stuck* on a patch of stationary background clutter, the UGV would wait indefinitely. Since these results were gathered from several intersections with uncontrolled traffic, they demonstrate the robustness and generalization of the detection system.

For testing the entire system as a whole, each experiment was staged as a coordinated event where the UGV and another vehicle (operated by a human driver) would approach the intersection in an agreed-upon order. The results for these

experiments are shown in Table 5.2. If the safety driver (in the UGV) had to override the autopilot to avoid a collision, or if the UGV did not begin to move, then the experiment was marked as a failure. In most cases (90%), the UGV effectively waited for the other vehicle to pass when the other vehicle arrived first, and then automatically proceeded through the intersection.

An annotated sequence of frames from one experiment is provided in Figures 5.5-5.9, which illustrate how the proposed system successfully handles a real road intersection. In each figure, the upper left image shows the view from the left camera, the upper middle image shows the view from the front camera, the upper right image shows the view from the right camera, and the bottom image shows the view from a camcorder placed inside the UGV to record the automatic motion of its steering wheel. The zoom level of the camcorder inside the UGV was set lower than that of the front camera atop the UGV to have a wide field of view and show as much of the steering wheel as possible. The upper images are basically the processed frames recorded by the three on-board computers. Figure 5.5 shows the instance when the UGV is arriving at the intersection, but another car is already waiting on the left road.

Table 5.1 Detection results in uncontrolled traffic

	Road			Total	%
	Left	Front	Right		
Visible	62	55	53	170	
Detected	61	50	50	161	94.7
Misdetected	1	5	3	9	5.3
False Alarm	0	0	0	0	0

Table 5.2 Results of the actual UGV experiments under autonomous control.

	Road			Total	%
	Left	Front	Right		
Success	4	2	3	9	90
Failure	1	0	0	1	10

The computer vision system is not turned on, because the UGV has not reached the stop sign yet. Figure 5.6 shows the instance when the UGV stops and turns on the proposed computer vision system. The system detects that a car is already waiting at the left road and commands the UGV to wait. The detected vehicle is surrounded by the best-match rectangle (BMR) overlaid in the left view. The large rectangles on the front and right views indicate the corresponding areas where the vehicles are being searched for by the vehicle detector using the corresponding OT-MACH filters. The vehicles were being searched for in these small areas of interest instead of the whole frames, in order to reduce the computation time in the correlation process and eliminate the possible false detections due to the background clutter. The small images overlaid at the bottom-left of every frame shows either the OT-MACH filters (if there is no vehicle on the road) or the current adaptive template (if there is a vehicle being tracked by the proposed tracker). The first line of the text indicates the maximum correlation value and the coordinates of the center of the best match rectangle (BMR). The BMR is shown only when the correlation value is above some threshold (as can be seen in the left view). The second line of the text indicates the scale of the OT-MACH filter that provides the maximum correlation value in the detection mode. The third line of the text indicates the road state provided by the corresponding FSM. Figure 5.7 shows the instance when the car at the other road begins to pass the intersection. The FSM for the left road correctly senses that the car is passing the intersection, as can be seen in the overlaid text. Figure 5.8 shows the instance when the car has exited the view of the left camera, although it is still visible in the video frames from the front camera and the camcorder. Since there were no vehicles on the right and the front roads, and the car has exited the view of the left road. The decision is made that it is now the UGV's turn to pass the intersection, so

the computer vision system is automatically turned off. This action is indicated by the absence of any overlaid content on the frames from the left, front, and right cameras atop the UGV. The UGV waits another two seconds so that the other car can pass the intersection safely. Finally, it starts passing the intersection automatically, as shown by the motion of the steering wheel and the scenes from the three cameras (atop the UGV) in Figure 5.9.

5.9 Chapter Summary

In this chapter, a vision based system is proposed that can enable a UGV to handle a road intersection. The system consists of mainly a vehicle detector, a tracker (which is discussed in Chapter 3), and a finite state machine (FSM) model of the road for each of the three cameras looking towards left, right, and front roads. For each camera view, the vehicle detector detects the vehicle on the other road, the tracker determines the current and predicted position of the detected vehicle in the consecutive video frames, and the FSM determines the state of the corresponding road. Finally, the traffic scenario obtained from the FSMs is utilized to make the final decision whether the UGV should go ahead and cross the intersection or wait for its turn. The experimental results show that the proposed system works with the success rate of 90%, which is significantly encouraging.

Figure 5.5 The UGV is arriving at the intersection, but another car is already waiting on the left road.

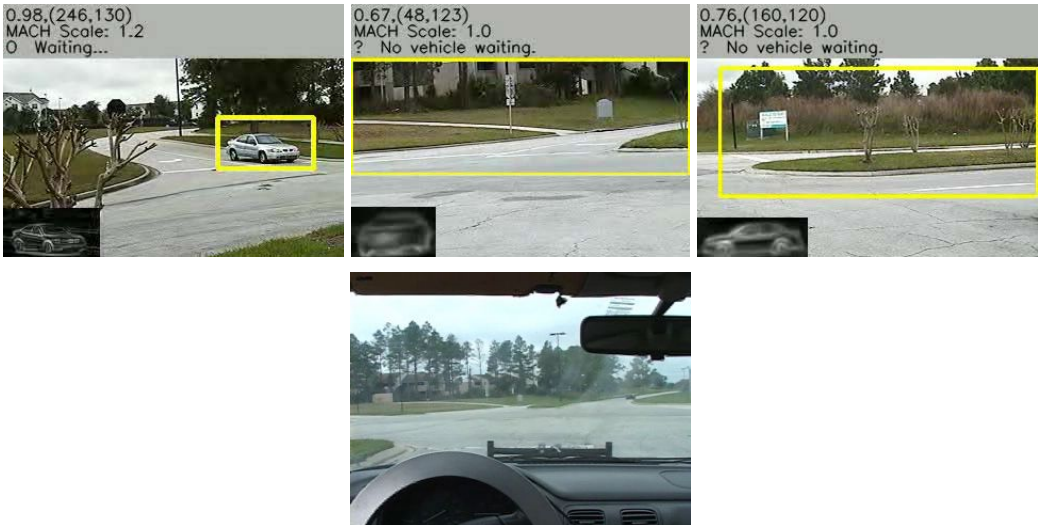

Figure 5.6 The UGV stops and turns on the computer vision system. The system detects that the car is at the intersection and commands the UGV to wait.

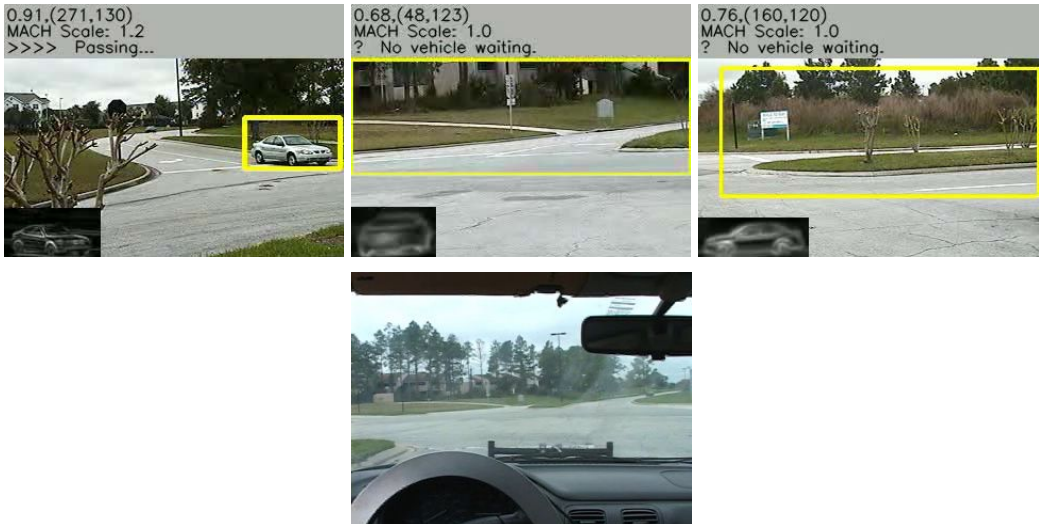

Figure 5.7 The car at the other road begins to pass the intersection.

Figure 5.8 The car has exited the view of the left camera, although it is still visible in the video from the camcorder. The computer vision system is turned off because it will now be the UGV's turn to cross the intersection.

Figure 5.9 Two seconds later, the UGV begins to pass the intersection automatically.

6

Conclusion and Future Directions

The thesis presented an adaptive edge-enhanced correlation based robust and real-time visual tracking framework, and its deployment in two machine vision systems: (1) an active camera tracking system, and (2) a system for a UGV to handle road intersections. In this chapter, the conclusion and the future work for the visual tracking framework and the machine vision systems based on it are drawn and presented, respectively.

6.1 Visual Tracking Framework

The proposed visual tracking algorithm is based on edge-enhanced BPNN-controlled fast normalized correlation (EE-BCFNC). The edge-enhancement (EE) operation in the EE-BCFNC is performed using Gaussian smoothing filter with an automatic standard deviation parameter, gradient magnitude, normalization, and thresholding. This kind of enhancement helps the correlation process handle object fading, low-contrast imagery and variation in the scene illumination in a better way and provides cleaner peak at the object location in the correlation surface than the most commonly used normalized correlation coefficient (NCC). The next operation in the EE-BCFNC is the BCFNC (BPNN-controlled fast normalized correlation), which exploits a back-propagation neural network (BPNN) to work as a switch between two

implementations of the normalized correlation (NC): direct method and FFT-SAT (fast Fourier transform – summed area table) method. The BPNN predicts which implementation will be faster for computing NC, given the search-window-size and the ratio of the template-size to the search-window-size. The varying scale of the object is handled by preparing scaled versions of the template, correlating them individually with the search window, and accepting the best scale, which produces the highest correlation peak in all the three correlation surfaces. The long-term neighboring clutter is dealt with by applying a 2D Gaussian weighting on the template pixels, using automatically computed optimal standard deviation parameters depending on the size of the current template. An effective and smooth method for updating the template is also introduced to handle the varying object appearance, the short-term neighboring clutter, and to some extent the template-drift. In order to formally handle the template drift and the inaccurate object initialization problems, a best match rectangle adjustment algorithm has been proposed. The visual tracking algorithm has been further improved using a Kalman predictor, in which a "constant acceleration with random walk" model of the target motion is used for good prediction accuracy. A novel method is presented to dynamically determine the location and size of the search-window depending on the prediction and the prediction-error of the Kalman filter. The occlusion of the target by other object(s) has been handled using a simple data association technique. The proposed algorithm has been compared with the most commonly used correlation tracker, and (for some sequences) the mean-shift and the condensation trackers. The results prove that the proposed tracker outperforms them in the presence of temporary object fading, significant background clutter, variations in the size of the object, variations in the illumination conditions, significant object maneuvering, multiple objects, obscuration,

and intermittent occlusion of the object, and variation in velocity, shape and orientation of the object.

The computational efficiency of the spatial domain implementation of NC for template matching can be further improved using the early termination algorithms, for example [101]. Then, its efficiency can be compared with the FFT-SAT method for different sizes of the templates and search images. If there is a significant difference between their computational efficiencies for different sizes of the images, the BPNN can be trained accordingly to switch between the two implementations.

Furthermore, a significant improvement in the proposed visual tracking framework would be to address the following complex real-world situations in which it may fail:

- A *moving* object is *completely* occluded by other object(s) for a *very long* duration, when the object changes its shape, speed, or direction significantly during the occlusion.
- The object is being occluded very slowly, in which case the correlation peak never falls below the threshold (τ_t) to sense the occurrence of the occlusion, because in this scenario the template is continuously being updated and the occluding object slowly invades into the template.
- There is a lot of clutter including exactly similar objects having similar orientation and scale in the search window as that of the object of interest.
- The object is changing its appearance fast, while its scale is increasing, e.g. a turning vehicle coming nearer the camera.

6.2 Active Camera Tracking System

As far as the active camera tracking system is concerned, a predictive open-loop car-following control (POL-CFC) has been presented to maneuver the pan-tilt unit (PTU), which moves the camera towards the object. The control algorithm calculates the predictive velocity of the object to be tracked using Kalman predicted position estimated by the visual tracking algorithm, and then smoothly adjusts the velocity of the PTU accordingly (without using any velocity feedback from the motors). As a result, the object remains always locked to the line-of-sight of the camera with good accuracy, regardless of the change in the velocity of the object. The POL-CFC algorithm offers 0% *overshoot*, 1.7 second *rise-time*, and ±1 pixel *maximum steady state error* for an object, which does not change its direction of motion *abruptly*. The steady state error is slightly increased, if the zoom level is more than 6x. The maximum error, while the camera is working at its highest zoom level of 25x, is only ±4 pixels from the center of the frame. However, if the object is changing its direction fast, the error may be increased further depending on the rate of change of the direction of the object motion. Nevertheless, the object remains always near the center of the frame. The precision of the motion controller depends mainly on the resolution of the PTU. Presently, a stepper-motor based PTU having resolution of 0.01285 degree/step is used. If a servo-motor based PTU having better resolution is used, the tracking can be smoother and more precise, especially when the camera is operating at very high zoom level.

The visual tracking algorithm and the pan-tilt control algorithm are implemented in separate threads exploiting the parallel processing capability of the presently available microprocessor in a standard PC. The throughput of the integrated

system is 25 to 75 fps (on a Centrino P4 1.7 GHz machine with 512 MB RAM) depending on the sizes of the adaptive template and the dynamic search window.

The system has been tested for more than a year in real-world indoor as well as outdoor scenarios. Some of the frames from the resulting videos recorded during various tracking sessions have been presented in this thesis. They prove that the system works very efficiently and robustly in the real-world complex scenarios.

6.3 A Vision Based System for a UGV to Handle a Road Intersection

UGVs will have to develop the capability to safely cross intersections with stop signs if they are going to be deployed in urban environments. In this research, some analysis of this specific problem is provided and a complete computer vision solution that combines a vehicle detection-and-tracking algorithm with a finite-state-machine model of the traffic near the intersection to automatically navigate the UGV through the intersection is proposed. The initial experiments of the system suggest that a computer vision approach can be the basis of an effective solution, but a truly robust system will need to better deal with subtle uncertainties in such a scenario. For example, it is currently assumed that the vehicle will take no more than two seconds to pass the intersection, but it is possible that the vehicle will unexpectedly stop while it is outside the view of the camera. The next work can be to address this problem by combining the output from the computer vision system with other systems, like a laser range finder, which can detect obstacles in the immediate path of the UGV.

References

[1] Y. Cui, S. Samarasekera, Q. Huang, M Greienhagen, "Indoor Monitoring Via the Collaboration Between a Peripheral Sensor and a Foveal Sensor," *IEEE Workshop on Visual Surveillance*, Bombay, India, 2-9, 1998.

[2] G. R. Bradski, "Computer Vision Face Tracking as a Component of a Perceptual User Interface," *IEEE Workshop on Applications of Computer Vision*, Princeton, 214-219, 1998.

[3] S. S. Intille, J.W. Davis, A.F. Bobick, "Real-Time Closed-World Tracking," *IEEE Conference on Computer Vision and Pattern Recognition*, Puerto Rico, 697-703, 1997.

[4] C. Wren, A. Azarbayejani, T. Darrell, A. Pentland, "PFinder: Real-Time Tracking of the Human Body," *IEEE Transactions on Pattern Analysis Machine Intelligence*, 19:780-785, 1997.

[5] A. Eleftheriadis, A. Jacquin, "Automatic Face Location Detection and Tracking for Model-Assisted Coding of Video Teleconference Sequences at Low Bit Rates," *Signal Processing–Image Communication*, 7(3): 231-248, 1995.

[6] R. Rosales, S. Sclaro, "3D Trajectory Recovery for Tracking Multiple Objects and Trajectory Guided Recognition of Actions," *IEEE Conference on Computer Vision and Pattern Recognition*, Fort Collins, vol. 2, 117-123, 1999.

[7] J. Ahmed, M. N. Jafri, J. Ahmad, and M. I. Khan, "Design and Implementation of a Neural Network for Real-Time Object Tracking," *International Conference on Machine Vision and Pattern Recognition in Conjunction with 4th World Enformatika Conference*, Istanbul, 2005.

[8] J. Ahmed, M. N. Jafri, J. Ahmad, "Target Tracking in an Image Sequence Using Wavelet Features and a Neural Network," *IEEE Region 10: Tencon'05 Conference*, Melbourne, Australia, 2005

[9] A. Doulamis, N. Doulamis, K. Ntalianis, and S. Kollias, "An Efficient Fully Unsupervised Video Object Segmentation Scheme Using an Adaptive Neural-Network Classifier Architecture," *IEEE Transaction on Neural Networks*, May 2003.

[10] E. V. Cuevas, D. Zaldivar, and R. Rojas, "Intelligent Tracking," *Technical Report B-03-15*, Freie Universitat Berlin, Germany, November 10, 2003.

[11] S. Blackman and R. Popoli, *Design and Analysis of Modern Tracking Systems*, pp. 309-313, Artech House, Boston, 1999.

[12] S. Wong, "Advanced Correlation Tracking of Objects in Cluttered Imagery," *Proceedings of SPIE*, Vol. 5810, 2005.

[13] R. C. Gonzalez, R. E. Woods, *Digital Image Processing*, 2nd Ed., Prentice-Hall, Inc., 2002

[14] N. Mir-Nasiri, "Camera-based 3D Tracking," *IEEE Region 10: Tencon'05 Conference*, Melbourne, Australia, 2005.

[15] "Basic Control Law for PTU to Follow a Moving Target," *Application Note 01*, Directed Perception Inc., 1996.

[16] J. P. Lewis, "Fast Normalized Cross-Correlation", *Industrial Light & Magic*, 1995.

[17] R. C. Gonzalez, R. E. Woods, and S. L. Eddins, *Digtal Image Processing Using MATLAB*, Pearson Education Pte. Ltd., 2004.

[18] F. Crow, "Summed-Area Tables for Texture Mapping", *Computer Graphics*, vol 18, No. 3, pp. 207-212, 1984.

[19] G. X. Ritter and J. N. Wilson, *Handbook of Computer Vision Algorithms in Image Algebra*. CRC Press, Boca Raton, Fl., 1996.

[20] C. Kuglin and D. Hines, "The Phase Correlation Image Alignment Method," *International Conference on Cybernetics and Society*, 1975, pp. 163-165.

[21] Q. Chen, M. Defrise, and F. Deconinck, "Symmetric Phase-Only Matched Filtering of Fourier-Mellin Transforms for Image Registration and Recognition," *IEEE Transactions on Pattern Analysis and Machine Intelligence*, Vol.16, December, 1994.

[22] H. S. Stone and B. Tao and M. McGuire, "Analysis of Image Registration Noise Due to Rotationally Dependent Aliasing," *Journal of Visual Communication and Image Representation,* Vol. 14, pp. 114-135, 2003.

[23] H. S. Stone, "Fourier-Based Image Registration Techniques", *NEC Research*, 2002.

[24] H. Demuth, and M. Beale, *Neural Network Toolbox for Use with MATLAB: User's Guide (v. 4)*, The Mathworks, Inc., 2001.

[25] S. Haykin, *Neural Networks: A Comprehensive Foundation*, 2nd Ed., Pearson Education, Delhi, 1999.

[26] L. Fausett, *Fundamentals of Neural Networks: Architectures, Algorithms, and Applications*, Prentice Hall, Englewood Cliffs, 1994.

[27] M. F. Moller, "A Scaled Conjugate Gradient Algorithm for Fast Supervised Learning," *Neural Networks*, vol. 6, pp. 525-533, 1993.

[28] *MATLAB 7.0 On-line Help Documentation*

[29] G. Bradski, A. Kaehler, and V. Pisarevsky, "Learning-Based Computer Vision with Open Source Computer Vision Library," *Intel Technology Journal*, Vol. 9, Issue 2, May 2005.

[30] S. E. Umbaugh, *Computer Imaging: Digital Image Analysis and Processing*, *CRC Press*, 2005.

[31] J. M. Fitts, "Precision Correlation Tracking via Optimal Weighting Functions," *18th IEEE Conference on Decision and Control Including the Symposium on Adaptive Processes*, 1979.

[32] R. L. Brunson, D. L. Boesen, G. A. Crockett, and J. F. Riker, "Precision Trackpoint Control via Correlation Track Referenced to Simulated Imagery," Bellingham, WA: Society of Photo-Optical Instrumentation Engineers, 1992.

[33] A. V. Oppenheim, R. W. Schafer, J. R. Buck, *Discrete-Time Signal Processing*, 2nd Ed., Prentice Hall, 1999.

[34] M. H. Hayes, *Digital Signal Processing*, McGraw-Hill, New York, 1999.

[35] Available at http://www.fastpasses.com

[36] E. Brookner, *Tracking and Kalman Filtering Made Easy*, John Wiley & Sons, 1998.

[37] G. Welch, and G. Bishop , "An Introduction to the Kalman Filter," *TR 95-041*, Department of Computer Science, University of North Carolina at Chapel Hill, Chapel Hill, NC 27599-3175, 2004

[38] M. S. Grewal, and A. P. Andrews, *Kalman Filtering: Theory and Practice Using MATLAB*, 2nd Ed., John Wiley & Sons Inc., New York, 2001.

[39] C. Fagiani and J. Gips, *An Evaluation of Tracking Methods for Human-Computer Interaction*, *Senior Thesis*, Computer Science Department, Boston College, Fulton Hall, Chestnut Hill, MA 02467, 2002

[40] CAVIAR (**C**ontext **A**ware **V**ision using **I**mage-based **A**ctive **R**ecognition) test video clips 2003-2004, available at http://homepages.inf.ed.ac.uk/rbf/CAVIAR/

[41] C. R. Wren, A. Azarbayejani, T. Darrell, and A.P. Pentland, "Pfinder: Real-Time Tracking of the Human Body," *IEEE Transactions on Pattern Analysis and Machine Intelligence*, vol. 19, no. 7, July 1997.

[42] C. Stauffer and W. Grimson, "Learning Patterns of Activity Using Real Time Tracking," *IEEE Transactions on Pattern Analysis and Machine Intelligence*, vol. 22, no. 8, pp. 747-767, Aug. 2000.

[43] D. Comaniciu, R. Visvanathan, and P. Meer, "Kernel based object tracking," *IEEE Transactions on Pattern Analysis and Machine Intelligence*, 25(5):564–575, 2003.

[44] A. Adam, E. Rivlin, and I. Shimshoni, "Robust Fragments-based Tracking using the Integral Histogram," *IEEE Conference on Computer Vision and Pattern Recognition*, 2006.

[45] M. Kass, A. Witkin, and D. Terzopoulos, "Snakes: Active Contour Models," *International Journal of. Computer Vision*, vol. 1, 1988.

[46] A. Yilmaz, X. Li, and M. Shah, "Contour-Based Object Tracking with Occlusion Handling in Video Acquired Using Mobile Cameras," *IEEE Transactions on Pattern Analysis and Machine Intelligence*, Vol. 26, No. 11, November 2004.

[47] F. Porikli, "Integral Histogram: A Fast Way to Extract Histograms in Cartesian Spaces," *IEEE Conference on Computer Vision and Pattern Recognition*, 2005

[48] D. Comaniciu, V. Ramesh, and P. Meer, "Real-time Tracking of Non-rigid Objects Using Mean Shift," *IEEE Conference on Computer Vision and Pattern Recognition*, Hilton Head, SC, volume 1, pages 142–149, 2000.

[49] F. Porikli and O. Tuzel, "Multi-kernel Object Tracking," *IEEE International Conference on Multimedia and Expo*, Amsterdam, Netherlands, 2005.

[50] F. Porikli, O. Tuzel, and P. Meer, "Covariance Tracking Using Model Update Based on Lie Algebra," *IEEE Conference on Computer Vision and Pattern Recognition*, 2006

[51] H. Wang, D. Suter and K. Schindler, "Effective Appearance Model and Similarity Measure for Particle Filtering and Visual Tracking," *European Conference on Computer Vision*, 2006.

[52] K. Nummiaroa, E. Koller-Meierb, and L. V. Gool, "An Adaptive Color-Based Particle Filter," *Image and Vision Computing*, 21: p. 99-110, 2003.

[53] M. Isard, and A. Blake, "CONDENSATION-Conditional Density Propagation for Visual Tracking," *International Journal of Computer Vision*, 29(1): p. 5-28, 1998.

[54] P. Perez, et al., "Color-Based Probabilistic Tracking," *European Conference on Computer Vision*, p. 661-675, 2002.

[55] Available at http://vision.stanford.edu/~birch/headtracker/seq/

[56] B. C. Kuo, *Automatic Control Systems*, 7th Ed., John Wiley & Sons, 1995.

[57] J. Ahmed, M. Shah, A. Miller, D. Harper, and M. N. Jafri, "A Vision Based System for a UGV to Handle a Road Intersection," *AAAI-07: 22nd Conference on Artificial Intelligence*, Vancouver, Canada, July 22-26, 2007.

[58] J. Ahmed, M. N. Jafri, M. Shah, and M. Akbar, "Real-Time Edge-Enhanced Dynamic Correlation and Predictive Open-Loop Car Following Control for Robust Tracking," *Machine Vision and Applications Journal*, Vol. 19, No. 1, pp. 1–25, January 2008.

[59] G. Chen and T. Tat Pham, *Introduction to Fuzzy Sets, Fuzzy Logic, and Fuzzy Control Systems*, CRC Press, Boca Raton, 2001.

[60] T. J. Ross, *Fuzzy Logic with Engineering Applications*, 2nd Edition, John Wiley & Sons Ltd., England, 2004.

[61] H. T. Nguyen and E. A. Walker, *A First Course in Fuzzy Logic*, 2nd Edition, Chapman & Hall/CRC, Boca Raton, 2000.

[62] H. T. Nguyen, N. R. Prasad, C. L. Walker, and E. A. Walker, *A First Course in Fuzzy and Neural Control*, Chapman & Hall/CRC, Boca Raton, 2003.

[63] J. Ahmed, and M. N. Jafri, "Improved Phase Correlation Matching," *Accepted in ICISP-08: International Conference on Image and Signal Processing*, France, July 1-3, 2008.

[64] O. Veksler, "Fast Variable Window for Stereo Correspondence using Integral Images," *IEEE Conference on Computer Vision and Pattern Recognition*, 2003.

[65] B. Han, C. Yang, R. Duraiswami, and Larry Davis, "Bayesian Filtering and Integral Image for Visual Tracking," *Workshop on Image Analysis for Multimedia Interactive Services (WIAMIS'05)*, 2005.

[66] A. Yilmaz, O. Javed, and M. Shah, "Object Tracking: A Survey," *ACM Computing Surveys*, 2006.

[67] C. Veenman, M. Reinders, and E. Backer, "Resolving Motion Correspondence for Densely Moving Points," *IEEE Transactions on Pattern Analysis and Machine Intelligence*, 23, 1, 54–72, 2001.

[68] D. Ballard and C. Brown, *Computer Vision*, Prentice-Hall, 1982.

[69] A. Ali and J. Aggarwal, "Segmentation and Recognition of Continuous Human Activity," *IEEE Workshop on Detection and Recognition of Events in Video*, 2001.

[70] S. Zhu, and A. Yuille, "Region Competition: Unifying Snakes, Region Growing, and Bayes/MDL for Multiband Image Segmentation," *IEEE Transactions* on *Pattern Analysis and Machine Intelligence*, 18, 9, 884–900, 1996.

[71] N. Paragios, and R. Deriche, "Geodesic Active Regions and Level Set Methods for Supervised Texture Segmentation," *International Journal of Computer Vision,* 46, 3, 223–247, 2002.

[72] P. Fieguth, and D. Terzopoulos, "Color-based Tracking of Heads and Other Mobile Objects at Video Frame Rates," *IEEE Conference on Computer Vision and Pattern Recognition*, 21–27, 1997.

[73] M. Black, and A. Jepson, "Eigentracking: Robust Matching and Tracking of Articulated Objects Using a View-based Representation," *International Journal of Computer Vision,* 26, 1, 63–84, 1998.

[74] S. Avidan, "Support Vector Tracking," *IEEE Conference on Computer Vision and Pattern Recognition*, 2001.

[75] S. Park, and J. K. Aggarwal, "A Hierarchical Bayesian Network for Event Recognition of Human Actions and Interactions," *Multimedia Systems*, 10, 2, 164–179, 2004.

[76] R. E. Kalman, "A New Approach to Linear Filtering and Prediction Problems," *Transactions of the ASME - Journal of Basic Engineering* Vol. 82: pp. 35-45, 1960.

[77] R. E. Kalman, and R. S. Bucy, "New Results in Linear Filtering and Prediction Theory," *Transactions of the ASME - Journal of Basic Engineering* Vol. 83: pp. 95-107, 1961.

[78] M. Blank, L. Gorelick, E. Shechtman, M. Irani, and R. Basri, "Actions as Space-time Shapes," *10th IEEE International Conference on Computer Vision*, pages 1395–1402, 2005. Available at: http://www.wisdom.weizmann.ac.il/~vision/SpaceTimeActions.html

[79] M. Nixon and A. Aguado, *Feature Extraction and Image Processing*, Newnes, Oxford, 2002.

[80] J. Jingying, H. Xiaodong, X. Kexin, and Y. Qilian, "Phase Correlation-based Matching Method with Sub-pixel Accuracy for Translated and Rotated Images," *IEEE International Conference on Signal Processing (ICSP'02)*, 2002.

[81] H. Foroosh (Shekarforoush) and J. B. Zerubia, "Extension of Phase Correlation to Subpixel Registration," *IEEE Transactions on Image Processing*, Vol. 11, NO. 3, March 2002.

[82] Y. Keller, A. Averbuch, and O. Miller, "Robust Phase Correlation," *17th International Conference on Pattern Recognition (ICPR'04)*, 2004.

[83] PETS-2001 Dataset: http://www.research.ibm.com/peoplevision/performanceevaluation.html

[84] G. Lathoud, J. Odobez, and D. Gatica-Perez, "AV16.3: An Audio-Visual Corpus for Speaker Localization and Tracking," *IDIAP*, Martigny, Switzerland, *IDIAP-RR* 28, 2004; *MLMI* 2004; *LNCS* 3361, pp. 182–195, Springer-Verlag Berlin Heidelberg, 2005.

[85] P. S. Maybeck, T. D. Herrera, and R. J. Evans, "Target Tracking Using Infrared Measurements and Laser Illumination," *IEEE Transactions on Aerospace and Electronic Systems*, vol. 30, pp. 758-68, 1994.

[86] http://www.ni.com/labview

[87] R. Manduchi and G. A. Mian, "Accuracy Analysis for Correlation-Based Image Registration Algorithms," *IEEE*, 2001.

[88] C. Rasmussen, "Combining Laser Range, Color, and Texture Cues for Autonomous Road Following," *ICRA*, 2002.

[89] W. Chun, J. Faukoner, and S. Munkeby, "UGV Demo II: Reuse Technology for AHS," *IEEE Intelligent Vehicles Symposium*, 1995.

[90] L. Matthies, A. Kelly, T. Litwin, and G. Tharp, "Obstacle Detection for Unmanned Ground Vehicles: A Progress Report," *Robotics Research 7 Springer-Verlag*, 1995.

[91] Z. Zhang, R. Weiss, and A.R. Hanson, "Qualitative Obstacle Detection," *In Proc. IEEE CVPR*, 1994.

[92] L. Matthies, "Stereo Vision for Planetary Rovers: Stochastic Modeling to Near Real-Time Implementation," *International Journal of Computer Vision*, Vol. 8, No. 1, 1992.

[93] L. Matthies, L., and E. Brown, "Machine Vision for Obstacle Detection and Ordnance Recognition," *AUVSI*, 1996.

[94] A. Talukder, R. Manduchi, L. Matthies, and A. Rankin, "Fast and Reliable Obstacle Detection and Segmentation for Cross Country Navigation," *IEEE Intelligent Vehicle Symposium*, 2002.

[95] A. Shashua, Y. Gdalyahu, and G. Hayun, "Pedestrian Detection for Driving Assistance Systems: Single frame Classification and System Level Performance," *IEEE Intelligent Vehicle Symposium*, 2004.

[96] R. Vidal, O. Shakernia, J. Kim, H. Shim, and S. Sastry, "Multiple Agent Probabilistic Pursuit-Evasion Games with Unmanned Ground and Aerial Vehicles," *IEEE Trans. on Robotics and Automation*, 2001.

[97] P. Refregier, "Optimal Trade-off Filters for Noise Robustness, Sharpness of the Correlation Peak, and Horner Efficiency," *Optics Letters*, Vol. 16, No. 11, 1991.

[98] A. Mahalanobis, B.V.K.V. Kumar, S. Song, S. Sims, and J. Epperson, "Unconstrained Correlation Filters," *Applied Optics*, Vol. 33, No. 17, 1994.

[99] H. Zhou, and T.-H Chao, "MACH Filter Synthesizing for Detecting Targets in Cluttered Environments for Gray-scale Optical Correlator," *Proc. SPIE*, vol. 3715, 1999.

[100] J. Ahmed and M. N. Jafri, "Best-Match Rectangle Adjustment Algorithm for Persistent and Precise Correlation Tracking," *Proc. IEEE International Conference on Machine Vision*, Islamabad, Pakistan, on 28-29 December, 2007.

[101] A. Mahmood, and S. Khan, "Early Termination Algorithms for Correlation Coefficient Based Block Matching," *Proc. ICIP-07: IEEE International Conference on Image Processing*, 2007.

Author Biography

Javed Ahmed received BE (Electronics Engineering) from Dawood College of Engineering & Technology (NED University of Engineering & Technology), Karachi (Pakistan), at the end of 1994. He obtained his MSc (Systems Engineering) with distinction (2nd position), under the fellowship program from Pakistan Institute of Engineering & Applied Sciences, Islamabad (Pakistan), in 1997. Then, he joined National Engineering & Scientific Commission (NESCOM) in 1997 and worked in the fields of real-time embedded systems, signal processing, and control systems. He got enrolled in Military College of Signals as a PhD candidate under the NUST Endowment Fund Scholarship program on 28 May 2003. During his PhD studies, he focused his research work on the real-time object detection and tracking in the real-world imagery. He proceeded to Computer Vision Lab, University of Central Florida (UCF), Orlando (USA) on 3 July 2006 to conduct a funded collaborative research until 28 February 2007. His publications include one journal paper and six conference papers given below:

1. Javed Ahmed, and M. Noman Jafri, "Improved Phase Correlation Matching," *Accepted in ICISP-08: 3rd International Conference on Image and Signal Processing*, to be held in Normandy, France, July 1-3, 2008.

2. Mikel Rodriguiz, Javed Ahmed, and Mubarak Shah "Action MACH: A Spatiotemporal Maximum Average Correlation Height Filter for Action Recognition," *Accepted in CVPR-08: IEEE International Conference on Computer Vision and Pattern Recognition*, to be held in Alaska, USA, in June 23-28, 2008.

3. Javed Ahmed, M. N. Jafri, Mubarak Shah, and Muhammad Akbar, "Real-Time Edge-Enhanced Dynamic Correlation and Predictive Open-Loop Car Following

Control for Robust Tracking," *Machine Vision and Applications Journal*, Vol. 19, No. 1, pp. 1–25, January 2008.

4. Javed Ahmed and M. N. Jafri, "Best-Match Rectangle Adjustment Algorithm for Persistent and Precise Correlation Tracking," *Proc. IEEE International Conference on Machine Vision*, Islamabad, Pakistan, on 28-29 December, 2007.

5. Javed Ahmed, Mubarak Shah, Andrew Miller, Don Harper, and M. N. Jafri, "A Vision Based System for a UGV to Handle a Road Intersection," *Proc. AAAI-07: 22nd Conference on Artificial Intelligence*, Vancouver, Canada, July 22-26, 2007.

6. Javed Ahmed, M. N. Jafri, and Jamil Ahmad, "Target Tracking in an Image Sequence Using Wavelet Features and a Neural Network," *Proc. IEEE Region 10: Tencon'05 conference*, Melbourne, Australia, 21-24 November 2005.

7. Javed Ahmed, M. N. Jafri, Jamil Ahmad, and Muhammed I. Khan, "Design and Implementation of a Neural Network for Real-Time Object Tracking," *Proc. International Conference on Machine Vision and Pattern Recognition, Fourth World Enformatika Conference (WEC'05)*, Istanbul, Turkey, 24-26 June 2005.

Besides, his following paper is under review process:

J. Ahmed, and M. N. Jafri, "Decaying Extension Based Phase Correlation for Robust Object Localization in Full Search Space," *Submitted in EUSIPCO-08: 16th European Signal Processing Conference*, to be held in Switzerland on August 25-29, 2008.

He served as a Technical Program Co-chair, papers reviewer and a member Organizing Committee of the ICMV-07: IEEE International Conference on Machine Vision organized by MCS (NUST) and University of Central Florida in Islamabad (Pakistan) on 28-29 December 2007. Besides, he has reviewed research papers of various international conferences and journals (including *Machine Vision and Applications* journal).

He is a graduate member of IEEE and a student member of SPIE. His current areas of research are computer vision, signal processing, control systems, and soft computing (i.e. artificial neural networks, fuzzy logic, and genetic algorithms).